

ABSTRACT

LEE, WILLIAM MORGAN. Modeling and Experimental Characterization of the Interfacial Behavior of High Strength Aluminum Alloys. (Under the direction of Professor Mohammed A. Zikry).

The interfacial microstructural behavior of high strength aluminum alloys was investigated by experimental characterization and dislocation density based crystalline plasticity finite element modeling. The microstructure of samples subjected to high strain-rate projectile impact and split Hopkinson testing was characterized at different length-scales associated with grains, inclusions, dispersed particles, and precipitates using OM, OIM, EDS, TEM/HRTEM, SAD, and SEM. Large grain sizes reduce GB area, allowing for more precipitation in the matrix and reduced susceptibility to GB cracking. Precipitates were shown to play a critical role in the toughening and strengthening of the alloy, with different deformation modes observed for Ω and θ' . Dispersed particles were associated with ductile failure, and inclusions were associated with ductile and shear failure.

Computational modeling using a dislocation density based crystalline plasticity finite element framework was focused on the dispersed particles because of the direct relationship to failure as observed by experimental characterization. An aluminum aggregate was modeled in quasi-static plane strain tension and compression to investigate the effects of dispersed particles and plastic deformation on numerical instabilities. Both local plastic deformation and the presence of these dispersed particles can trigger hourglass instabilities, caused by the difference in the deformability of neighboring elements and the energy modes associated with hourglassing. Therefore, hourglass controls are necessary to accurately delineate material and numerical instabilities.

A new formulation based on an eigenstrain representation of Orowan looping was also developed, and it was coupled with the dislocation density based crystalline plasticity finite element framework to model the unrelaxed plastic strain and interfacial behavior associated with the dispersed particles in high strength aluminum alloys. This representation accounts for the increased stresses associated with Orowan looping at interfacial regions associated with extra half-planes of atoms, and for plastic relaxation using the incompatibilities in lattice rotations between the particles and the alloy matrix. Predictions indicate that the orientations and morphologies of the particles with respect to the most active slip plane are critical factors in the relaxation of the eigenstrains associated with the loops.

These interfacial effects of the dispersed particles on the dynamic deformation of high strength aluminum alloys were also investigated as a function of particle size, spacing, and volume fraction, and grain boundary (GB) misorientations. Particle spacing had a significant effect on the shear slip distribution, with localization occurring between the particles for smaller particle spacing. The eigenstress fields associated with the larger particles led to longer-range interaction of pressure fields, which can promote void coalescence for nucleated voids at the particle-matrix interfaces. GB misorientation had a significant effect on the behavior associated with the particles, with plastic shear slip localizing at the particle-matrix interfaces for low angle GB misorientations, and at GBs and GB junctions for high angle misorientations.

The interrelated effects of dispersed particle interfaces and GB misorientations on the dynamic deformation of high strength aluminum alloys were investigated by modeling an aluminum tri-crystal with different distributions of dispersed particles and GB misorientations. Slip was relatively homogeneous and associated with initially preferential

slip planes for low angle GB misorientations. Particle dispersion had a greater effect on the deformation behavior for the high angle misorientation tri-crystal, with dislocation density generation at the particle-matrix interface resulting in particle-controlled shear banding, which can inhibit shear banding caused by triple junctions. Larger dispersed particles led to higher stress concentrations at the triple junction and higher tensile pressures at the particle-matrix interfaces. This study underscores the effects of dispersed particles on the behavior of high strength aluminum alloys, and how material competition between dispersed particles and GB junctions can be potentially controlled to mitigate shear localization within and between grains.

© Copyright 2011 by William Morgan Lee

All Rights Reserved

Modeling and Experimental Characterization of the Interfacial Behavior of High Strength
Aluminum Alloys

by
William Morgan Lee

A dissertation submitted to the Graduate Faculty of
North Carolina State University
in partial fulfillment of the
requirements for the degree of
Doctor of Philosophy

Mechanical Engineering

Raleigh, North Carolina

2011

APPROVED BY:

Professor Mohammed A. Zikry
Committee Chair

Professor Kara Peters

Professor Jeffrey Eischen

Professor Donald Brenner

DEDICATION

This work is dedicated to those who have shaped me into who I am today. I feel very blessed to have the support of my parents, family, church family, teachers, professors, friends, teammates, co-workers, and coaches. You all have taught me many valuable lessons that I have been able to apply to this project.

BIOGRAPHY

William Morgan Lee was born in Raleigh, NC on January 6, 1984. He was raised in Fuquay-Varina, NC and graduated from Fuquay-Varina High School in 2002. He attended North Carolina State University for undergraduate studies in mechanical engineering. As a starting long snapper for the NC State football team from 2004 to 2006, he earned Academic All-American honors from ESPN the Magazine and COSIDA in 2006, and had the honor of receiving the 2006 Bo Rein award for a vital contribution in an unsung role, an award first won by head coach Chuck Amato. He received a Bachelor of Science Degree in Mechanical Engineering from NC State in the spring of 2006.

William stayed at NC State for graduate studies, earning a Master of Science degree in Mechanical engineering under advisor Professor Mohammed A. Zikry in the spring of 2008. He was awarded a Department of Defense National Defense Science and Engineering Fellowship in 2008. He also earned a Master of Materials Science and Engineering degree in the spring of 2010. The research relating to this dissertation has generated the following research papers and proceedings:

Elkhodary, K.I., **Lee, W.M.**, Cheeseman, B., Brenner, D.W., and Zikry, M.A., "High Strain-Rate Behavior of High Strength Aluminum Alloys," *Mater. Res. Soc. Symp. Proc.* Vol. 1137. 1137-EE05-31

Elkhodary, K.I., **Lee, W.M.**, Cheeseman, B., Sun, L., Brenner, D.W., and Zikry, M.A., "The Effects of Precipitates and Mn-bearing Particles on the High Strain-Rate Compression of High Strength Aluminum," *Mater. Res. Soc. Symp. Proc.* Vol. 1225. 1225-HH04-08

Elkhodary, K.I., **Lee, W.M.**, Sun, L., Brenner, D.W., and Zikry, M.A., "Deformation mechanisms of an Ω precipitate in a high strength aluminum alloy subjected to high strain rates," *Journal of Materials Research*, Vol. 26, No. 4, Feb 2011

Lee, W.M., and M.A. Zikry, “Microstructural Characterization of a High Strength Aluminum Alloy Subjected to High-Strain-Rate Impact,” *Metallurgical and Materials Transactions A*. Vol. 42, No. 5, May 2011

Salem, H.A.G., **Lee, W.M.**, Bodelot, L., Ravichandran, G., and Zikry, M.A., “Quasi-Static and High Strain-Rate Experimental Microstructural Investigation of a High Strength Aluminum Alloy,” Submitted.

Lee, W.M., and M.A. Zikry, “Microstructurally Induced Hourglass Modes,” Submitted.

Lee, W.M., and M.A. Zikry, “Modeling the Interfacial Plastic Strain Incompatibilities Associated with Dispersed Particles in High Strength Aluminum Alloys,” Submitted.

Lee, W.M., and M.A. Zikry, “High Strain-Rate Modeling of the Interfacial Effects of Dispersed Particles in High Strength Aluminum Alloys,” Submitted.

Lee, W.M., and M.A. Zikry, “Dispersed Particle and Triple Junction Interactions in Aluminum Alloys,” Submitted.

Upon completion of the Doctor of Philosophy degree in Mechanical Engineering, he will work as a Design Engineer for Stewart-Haas Racing in Kannapolis, NC.

ACKNOWLEDGMENTS

I would like to first and foremost thank God for the blessing me with the opportunities to allow me to pursue and complete this portion of my educational journey. I would like to acknowledge and thank those who assisted me in my efforts in this research. A special thanks to Professor Mohammed A. Zikry for his support and guidance through the research. I would also like to thank my Master's committee members for their guidance, Professor Kara Peters and Professor Alina Chertock, and my PhD committee members, Professor Kara Peters, Professor Jeffrey Eischen, and Professor Donald Brenner, along with my co-workers under Professor Zikry, James Pearson, Jibin Shi, Tarek Hatem, Omid Rezvanian, Khalil Elkhodary, Pratheek Shanthraj, Siqi Xu, Prasenjit Khanikar, Drew LaBarbera, Letisha McLaughlin, Zach Hester, Shoayb Ziaei, and Qifeng Wu. Also, none of this would have been possible without the support and guidance of Dr. Bryan Cheeseman at the Army Research Laboratory, Dr. Alex Cho at ALCAN/ATI, Dr. Bruce Lamattina at the Army Research Office, and Dr. James Wargo at JIEDDO.

I would especially like to thank the following people for their assistance with the research: Skip Richardson at NCSU MAE Fabrication Shop for machining samples; Dr. Dale Batchelor, Chuck Mooney, Roberto Garcia, and Ka "Wingo" Wong at NCSU AIF for their assistance and patience with me in sample preparation and observation; Pete Thompson at Industrial Machine Solutions for the waterjet cutting of the shot plate samples; Andy Newell from the NCSU MSE Department for the electrochemical TEM sample preparation and guidance and expertise with the TEM; Tyra Nylese and John Carpenter from EDAX for OIM inspection of the alloy; John Mastovich from Bruker EDS for voluntary investigation of

constituent elements; and Dr. Tom Rawdanowicz for his teaching, support, and guidance with the TEM.

I am extremely thankful to everyone that made this educational experience possible. This includes all of my teachers in Fuquay-Varina from elementary to high school who prepared me so well for a college education, and all of my professors at NC State. I would like to thank all of my coaches for believing in me, which opened MANY doors for me and allowed me the opportunities that have led me to where I am today. I would like to thank the organizations and people that funded my graduate education, including JIEDDO and the U.S. Army Research Office Grant No. ARO W911 NF-06-1-0472, the DoD NDSEG Fellowship, the Warren-Wolfpack Club Postgraduate Fellowship, the ACC Postgraduate Fellowship, and those that funded my undergraduate education, the NCSU football scholarship, the TYCO scholarship, the National Football Foundation and College Hall of Fame Triangle Chapter High School Scholar Athlete award, and, last but not least, my parents.

And to my parents, THANK YOU for leading me in the right direction and giving me all the support I needed to accomplish what I have so far.

TABLE OF CONTENTS

LIST OF TABLES	x
LIST OF FIGURES	xi
Chapter 1: Introduction	1
1.1 Overview	1
1.2 General Research Objectives and Approach	3
1.3 Dissertation Organization	5
References—Chapter 1	6
Chapter 2: Microstructural Characterization of a High Strength Aluminum Alloy Subjected to High Strain-Rate Impact	9
2.1 Introduction	9
2.2 Experimental Methods	11
2.2.1 Projectile Impact of a 1.5” (38 mm) plate	11
2.2.2 Split Hopkinson Impact of Shear Compression Specimens	13
2.3 Results and Discussion-Projectile Impact	13
2.3.1 Damage Modes	13
2.3.2 Microstructural Characteristics	14
2.3.2.1 Grain Morphology	14
2.3.2.2 Dispersed Particles and Inclusions	15
2.3.2.3 Precipitates	17
2.4 Results and Discussion-Split Hopkinson	19
2.5 Conclusions	20
References—Chapter 2	22
Tables and Figures—Chapter 2	24
Chapter 3: Dislocation Density Based Crystalline Plasticity Constitutive Formulation	41
3.1 Multiple Slip Crystal Plasticity Kinematics	41
3.2 Dislocation Density Evolution	44
References—Chapter 3	48
Tables and Figures—Chapter 3	49
Chapter 4: Numerical Methods	50
4.1 Determination of the Total Velocity Gradient	50
4.2 Determination of the Plastic Velocity Gradient	52
4.3 Solution of Systems of ODE’s	53
References—Chapter 4	55
Chapter 5: Microstructurally Induced Hourglass Modes	56
5.1 Introduction	56
5.2 Approach—Measure of Hourglass Modes	58
5.3 Results	58
5.3.1 Microstructural Representation	58
5.3.2 Effect of Matrix Deformation	59
5.3.3 Effects of Dispersed Particles	60
5.3.4 Influence of Microstructure and Deformation on Hourglass Modes	60

5.4 Conclusions.....	64
References—Chapter 5	65
Tables and Figures—Chapter 5	66
Chapter 6: Orowan Looping and Plastic Relaxation in Crystalline Plasticity Finite Element Analysis.....	75
6.1 Introduction.....	75
6.2 Approach.....	78
6.2.1 Orowan Looping	78
6.2.2 Verification of Eigenstrain Representation.....	78
6.2.3 Representation of Plastic Relaxation	80
References—Chapter 6	84
Tables and Figures—Chapter 6	87
Chapter 7: Quasi-static Modeling of the Interfacial Plastic Strain Incompatibilities Associated with Dispersed Particles in High Strength Aluminum Alloys.....	92
7.1 Introduction.....	92
7.2 Results.....	92
7.2.1 Microstructural Representation.....	92
7.2.2 Single Particle: Model 1.....	94
7.2.3 Orientation Effects: Model 2	95
7.2.4 20 Grain Aggregate: Model 3	97
7.3 Conclusions.....	98
References—Chapter 7	100
Tables and Figures—Chapter 7	101
Chapter 8: High Strain-Rate Modeling of the Interfacial Effects of Dispersed Particles in High Strength Aluminum Alloys.....	114
8.1 Introduction.....	114
8.2 Results.....	114
8.2.1 Microstructural Representation.....	114
8.2.2 Single Grain	116
8.2.2.1 Particle Spacing Effects	116
8.2.2.2 Particle Size Effects	117
8.2.2.3 Volume Fraction Effects	118
8.2.3 Polycrystalline Aggregate and Dispersed Particle Distributions	119
8.3 Conclusions.....	122
References—Chapter 8	124
Tables and Figures—Chapter 8	125
Chapter 9: Dispersed Particle and Triple Junction Interactions in Aluminum Alloys	137
9.1. Introduction.....	137
9.2. Results.....	139
9.2.1 Microstructural Representation.....	139
9.2.2 Grain Boundary (GB) Misorientation.....	140
9.2.3 Dispersed Particle-GB Interaction	141
9.2.3.1 Particle Spacing	141

9.2.3.2 Particle Size	143
9.3. Conclusions.....	145
References—Chapter 9.....	147
Tables and Figures—Chapter 9	148
Chapter 10: Future Research Recommendations.....	161
References—Chapter 10.....	163

LIST OF TABLES

Table 2.1: Composition of Al 2139 (Cho and Bes 2006)	24
Table 2.2: Effect of strain-rate on properties of Al 2139 (Elkhodary, Sun et al. 2009)	24
Table 3.1: Summary of interactions and coefficient values in an FCC crystal.....	49
Table 3.2: Summary of g-coefficients for dislocation density evolution equations	49
Table 5.1: Material properties of aluminum matrix and manganese-bearing dispersed particles	66
Table 6.1: Parameters used for homogeneous inclusion investigation	87
Table 6.2: Parameters used for inhomogeneous inclusion investigation	87
Table 7.1: Material properties of aluminum matrix and manganese-bearing dispersed particles	101
Table 8.1: Grain misorientation averages for polycrystalline aggregates (degrees).....	125
Table 8.2: Material properties of aluminum matrix and manganese-bearing dispersed particles	125
Table 9.1: Euler angles used in the tri-crystal simulations (deg).....	148
Table 9.2: GB misorientation angles (deg).....	148
Table 9.3: Material properties of aluminum matrix and manganese-bearing dispersed particles	148

LIST OF FIGURES

Figure 2.1: Backside of 1.5” (38 mm) plate of Al 2139 after V_{50} test showing bulging and disc punchout	25
Figure 2.2: Polished cross-section indicating damage modes of penetrated region	26
Figure 2.3: OM image of shear crack running into shear bands in a penetrated region	27
Figure 2.4: OM image of a shear crack due to particle debonding initiated at the matrix/inclusion interface	28
Figure 2.5: SEM image of a cracked Al-Cu-Fe-Mn inclusion promoting shear failure in an area of otherwise ductile failure.....	29
Figure 2.6: SEM image and schematic of dispersed particles in the center of dimples on a ductile fracture surface with the long axis of the particles in the plane of deformation, indicating void nucleation due to particles of this orientation.....	30
Figure 2.7: SEM image and schematic of dispersed particles on the ridges of a ductile fracture surface with the long axis of the particles inclined to the plane of deformation, indicating resistance to void coalescence and final failure.....	31
Figure 2.8: Comparison of the effects of inclusions and dispersed particles on a ductile fracture, showing larger void sizes associated with the inclusions (marked with arrows)	32
Figure 2.9: SAD pattern ($B=[011]$), of an undeformed specimen, showing some breakup in the $[200]$ direction associated with the precipitation of θ' and spots at $1/3$ and $2/3$ $[220]$ associated with Ω	33
Figure 2.10: DF TEM image of Ω and θ' precipitates; $B=[011]$, $g=[200]$, showing a “wavy” deformation mode for θ' and a “multiple cutting” mechanism for Ω associated with the high strain-rate deformation.....	34
Figure 2.11: HRTEM image of a deformed θ' precipitate, $B=[011]$; FFT inset indicating precipitate can rotate away from matrix habit plane.....	35
Figure 2.12: HRTEM image of a deformed Ω precipitate, $B=[011]$; FFT inset indicating uncut regions maintain planar relationship with matrix	36
Figure 2.13: HRTEM image of a deformed Ω precipitate, $B=[011]$, showing extensive multiple cutting.....	37
Figure 2.14: a) Typical shear dominated fracture surface; b) Region of mostly void sheet dimpled rupture in the vicinity of shear dominated fracture for split Hopkinson testing	38
Figure 2.15: a) Al-Cu-Fe-Mn inclusion cracking and associated local shear fracture surface; b) Al-Cu-Fe-Mn inclusions associated with large dimples in area of dimpled void sheet failure for split Hopkinson testing	39

Figure 2.16: a) $\text{Al}_{20}\text{Cu}_2\text{Mn}_3$ dispersed particles with the long axis in the plane of deformation located in the center of the dimples; b) $\text{Al}_{20}\text{Cu}_2\text{Mn}_3$ dispersed particles with the long axis normal to the plane of deformation, observed on the ridges for split Hopkinson testing.....	40
Figure 5.1: Hourglassing deformation associated with a 10% hourglass strain in the x-direction	67
Figure 5.2: Contour plots of a) hourglass strain norm and b) effective plastic slip at 10% nominal plane strain compression, matrix only	68
Figure 5.3: Contour plots of a) hourglass strain norm and b) effective plastic slip at 10% nominal plane strain tension, matrix only.....	69
Figure 5.4: Contour plots of a) hourglass strain norm and b) effective plastic slip at 10% nominal plane strain compression, dispersed particles included	70
Figure 5.5: Contour plots of a) hourglass strain norm and b) effective plastic slip at 10% nominal plane strain tension, dispersed particles included.....	71
Figure 5.6: Contour plots of hourglass strain norm and effective plastic slip, factor (i). a) Localized shear slip in matrix element triggering hourglass modes in surrounding regions; b) localized shear in matrix elements at triple junction triggering hourglass modes in neighboring elements; c) deformable matrix elements triggering hourglass modes in a dispersed particle	72
Figure 5.7: Contour plots of hourglass strain norm and effective plastic slip, factor (ii): hourglassing in matrix caused by constraint associated with single element thick dispersed particles at a) 10% nominal tension and at b) 10% nominal compression; arrows indicate dispersed particles	73
Figure 5.8: Effect of particle meshing on propagation of the hourglass instability; arrows indicate dispersed particles	74
Figure 6.1: Schematic and model of Eshelby verification problem.....	88
Figure 6.2: Comparison of the particle stress using the eigenstrain-based finite element method and the Eshelby solution for the homogeneous inclusion problem; maximum error=0.52%	89
Figure 6.3: Comparison of the particle stress using the eigenstrain-based finite element method and the Eshelby solution for the inhomogeneous inclusion problem; maximum error=1.13%	90
Figure 6.4: Schematic of looping and relaxation in pure shear with respect to the current configuration with different eigenvelocity gradients and lattice rotation calculations related to (b) unrelaxed and (c) fully relaxed plastic strains. Note the presence and deficit of an extra half-plane of atoms associated with Orowan looping in (b).....	91

Figure 7.1: Finite element model: a) single particle model, b) single grain model; (i) particles aligned with long axis parallel to most active slip plane and (ii) particles aligned with long axis normal to most active slip plane, and c) 20 grain aggregate	102
Figure 7.2: Contour plots of a particle under shear, a) von Mises stress accumulations (normalized by the matrix static yield stress) and b) tensile pressure accumulations (normalized by the matrix Young's modulus) for a single 400 nm by 800 nm particle aligned with the long axis oriented normal to the most active slip plane	103
Figure 7.3: Amount of eigenstrain relaxed at different particle orientations; a) 200 by 400 nm particle and b) 400 by 800 nm particle	104
Figure 7.4: Contour plots of the amount of eigenstrain relaxed at 10% nominal compression; a) particles aligned with long axis parallel to most active slip plane (1-11) and b) particles aligned normal to most active slip plane (1-11)	105
Figure 7.5: Comparison of the amount of eigenstrain relaxed in Figure 4 plotted as a function of the aspect ratio with respect to the most active slip plane	106
Figure 7.6: Contour plots of the von Mises stress in the matrix (normalized by the matrix static yield stress) at 10% nominal compression; a) particles aligned with the long axis parallel to most active slip plane (1-11) and b) particles aligned normal to most active slip plane (1-11)	107
Figure 7.7: Contour plots of the effective plastic shear slip in the matrix at 10% nominal compression; a) particles aligned with long axis parallel to most active slip plane (1-11) and b) particles aligned normal to most active slip plane (1-11)	108
Figure 7.8: Contour plots of the mobile dislocation density (m^{-2}) on the (a) most active (1-11)[-101] and (b) secondary (-1-11)[-110] slip system at 10% nominal compression.	109
Figure 7.9: Evolution of the amount of relaxation for particles a) aligned parallel to the most active slip plane and b) aligned normal to the most active slip plane	110
Figure 7.10: von Mises (normalized by the matrix static yield stress) and pressure (normalized by the matrix Young's modulus) contours for the matrix of 20-grain aggregate subjected to 10% nominal compressive strain	111
Figure 7.11: Contour plots of the number of active slip systems for the simulations with and without the eigenstrain formulation	112
Figure 7.12: Contour plots of a) percent of eigenstrain relaxed and b) lattice rotations for the 20-grain aggregate	113
Figure 8.1: Summary of the investigated models: a) 20 μm by 20 μm single grain with random dispersions of particles and b) 20 μm by 20 μm polycrystalline aggregate with 20, 35, and 48 grains and with one dispersed particle per grain	126
Figure 8.2: Effective plastic slip contours in the matrix at 10% nominal compressive strain for 1.0% volume fraction of particles in a single crystal at a strain-rate of $50 \times 10^{-3} s^{-1}$: a)	

800 nm by 425 nm average dispersed particle size and b) 600 nm by 300 average dispersed particle size. Arrows indicate banded slip	127
Figure 8.3: Pressure contours in the matrix (normalized by the matrix Young's modulus) at 10% nominal compressive strain for 1.0% volume fraction of particles in a single crystal: a) 800 nm by 425 nm average dispersed particle size and b) 600 nm by 300 nm average dispersed particle size. Contour levels set to emphasize decrease in compressive pressures and transition to tensile pressures at the particle-matrix interfaces	128
Figure 8.4: von Mises stress (normalized by the matrix static yield stress) and pressure (normalized by the matrix Young's modulus) contours in the matrix at a 10% nominal compressive strain for particles aligned parallel to the most active slip plane: a) 1.0% volume fraction, 800 nm by 425 nm average dispersed particle size and b) 0.5% volume fraction, 600 nm by 300 nm average dispersed particle size	129
Figure 8.5: Matrix effective plastic shear slip comparison at 10% nominal compressive strain for 600 nm by 300 nm average size particles normal to most active slip plane for 0.5%, 1.0% (arrow indicates banded slip), and 1.5% volume fraction (arrow indicates slip localization between particles).....	130
Figure 8.6: Percent of eigenstrain relaxed	131
$\left(\int D_{12,max_shear}^* dt - \int D_{12,max_shear_relaxed}^* dt \right) / \int D_{12,max_shear}^* dt$ at 10% nominal compressive strain for 600 nm by 300 nm average size particles parallel to the most active slip plane for 0.5%, 1.0% and 1.5% volume fractions.....	131
Figure 8.7: Comparison of effective plastic shear slip in the matrix at 10% nominal compressive strain for a 20-grain aggregate with high angle GB misorientations with and without the eigenstrain formulation included at a) quasi-static (0.004 s^{-1}) and b) $50,000 \text{ s}^{-1}$ strain-rates	132
Figure 8.8: Matrix temperature (normalized by 293 K) at 10% nominal compressive strain for the 20-grain aggregate with the eigenstrain formulation at a strain-rate of $50,000 \text{ s}^{-1}$.	133
Figure 8.9: a) Effective plastic shear slip in the matrix and b) percent of eigenstrain relaxed at 10% nominal compressive strain for the 20-, 35-, and 48-grain aggregates with low angle GB misorientations.....	134
Figure 8.10: Effective plastic shear slip in the matrix and b) percent of eigenstrain relaxed at 10% nominal compressive strain for the 20-, 35-, and 48-grain aggregates with high angle GB misorientations.....	135
Figure 8.11: Vertical normal stress component contours (normalized by matrix static yield stress) detailing the effect of dispersed particles on stress accumulations associated with spall failure.....	136
Figure 9.1: Schematic of the models; Initial alignment of the most active slip system in each grain is indicated	149

Figure 9.2: Effective shear slip and lattice rotation contours of the tri-crystal with no particles at 10% nominal compressive strain; a) Low angle GB misorientation and b) high angle GB misorientation	150
Figure 9.3: Mobile dislocation densities (m^{-2}) on a secondary (-111)[101] slip system with no particles at 10% nominal compressive strain; a) Low angle GB misorientation and b) high angle GB misorientation. Initial orientation of the slip system in grain 3 is shown	151
Figure 9.4: Effective plastic shear slip contours for 600 nm by 300 nm average particle size dispersions with low angle GB misorientations at 10% nominal compressive strain; a) 0.5% volume fraction, b) 1.0% volume fraction, and c) 1.5% volume fraction	152
Figure 9.5: a) Lattice rotation and b) percent of eigenstrain relaxed.....	153
$((\int D_{12,max_shear}^* dt - \int D_{12,max_shear_relaxed}^* dt) / \int D_{12,max_shear}^* dt)$ for 1.5% volume fraction of 600 nm by 300 nm average size particles and low angle GB misorientations at 10% nominal compressive strain.....	153
Figure 9.6: Effective plastic shear slip contours for 600 nm by 300 nm average particle size dispersions with high angle GB misorientations at 10% nominal compressive strain; a) 0.5% volume fraction, b) 1.0% volume fraction, and c) 1.5% volume fraction	154
Figure 9.7: Number of active slip systems at 10% nominal compressive strain for 600 nm by 300 nm average particle size dispersions with high angle GB misorientations; a) 0.5% volume fraction, b) 1.0% volume fraction, and c) 1.5% volume fraction	155
Figure 9.8: Effective plastic shear slip and lattice rotation contours for low angle GB misorientations at 10% compressive strain; a) 425 nm by 212.5 nm average particle size, b) 600 nm by 300 nm average particle size, and c) 850 nm by 425 nm average particle size	156
Figure 9.9: Contours of effective plastic shear slip and percent of particle eigenstrain relaxed for the same particle dispersion and orientation with high angle GB misorientations at 10% nominal compressive strain; a) 425 nm by 212.5 nm average particle size, b) 600 nm by 300 nm average particle size, and c) 850 nm by 425 nm average particle size.	157
Figure 9.10: von Mises stress (normalized by matrix static yield stress) and pressure (normalized by matrix Young's modulus) contours for the same particle dispersion and orientation with high angle GB misorientations at 10% compressive strain; a) 425 nm by 212.5 nm average particle size, b) 600 nm by 300 nm average particle size, and c) 850 nm by 425 nm average particle size. Pressure contour levels set to emphasize decrease in compressive pressures and transition to tensile pressures at the particle-matrix interface.....	158
Figure 9.11: Evolution of mobile dislocation densities on a secondary (-111)[101] slip system as a function of overall nominal compressive strain for matrix only and 850 nm by 425 nm average particle size simulations	159

Figure 9.12: Nominal stress-nominal strain curves for the a) high angle random and b) low angle random GB misorientation tri-crystal investigations, showing a 2.4% spread in values at 10% nominal strain for high angle GB misorientations compared to 0.7% associated with low angle GB misorientations 160

Chapter 1: Introduction

1.1 Overview

Lightweight alloy development is a major focus of industries that require high performance materials for applications that can be hindered by excessive weight, such as aerospace, automotive, or armor applications. Processing techniques and aging of aluminum alloys can be used to develop alloys with high strength, toughness, and ductility, due to the formation of microstructural features, such as nanoscale precipitates and larger dispersoids, which act as barriers to dislocation motion, hence limiting plastic slip in the material. The heat treatment and processing of the alloys can be adjusted to acquire the desired properties by altering the microstructure (Polmear 2004).

The precipitate θ' (Al_2Cu) forms as plates on the $\{100\}_\alpha$ planes of Al-Cu based alloys with a tendency to precipitate on dislocation lines (Polmear and Chester 1989) and low angle GBs (Vaughan 1968). Recently, emphasis has been placed on quaternary Al-Cu-Mg-Ag alloys since the realization that the addition of Ag enhances precipitation of Ω (Al_2Cu), which nucleates homogeneously on the $\{111\}_\alpha$ habit planes within the alloy matrix (Cho, Lisagor et al. 2007) and significantly strengthens the alloy (Chester and Polmear 1980). Plate-like precipitates on these planes have a greater impact on strengthening than precipitates on other planes in aluminum alloys (Nie, Muddle et al. 1996).

The addition of Mn to the quaternary alloy leads to the formation of orthorhombic dispersed particles of the composition $\text{Al}_{20}\text{Cu}_2\text{Mn}_3$ during the heat treatment of the alloy (Starke 1997). These particles strengthen and toughen the alloy through Orowan dislocation

looping (Feng, Lin et al. 1984), and have been strongly associated with failure, which is controlled by a competition between dispersed particles homogenizing deformation, which delays void coalescence, and decreased particle spacing of larger inclusions, which enhances void coalescence (Walsh, Jata et al. 1989). Also, it has been shown that the presence of dispersed particles increases ductility by reducing the tendency for intergranular failure by initiating more homogeneous transgranular failure in the grain matrix (Starke and Sanders 1980).

The effects of dispersed particles on the performance of alloys have been extensively researched in attempts to develop macroscopic models for the behavior of these alloys. Brown and Stobbs (1971a) developed a model based on the Eshelby problem (Eshelby 1957), relating the unrelaxed plastic strain associated with Orowan looping to an eigenstrain (Mura 1987), or in the terminology of Eshelby, transformation strain (Eshelby 1957). Relaxation of this unrelaxed plastic strain was a topic of debate for smaller particle sizes (Brown and Stobbs 1971b, 1976; Atkinson, Brown et al. 1974; Hirsch and Humphreys 1970; Humphreys and Hirsch 1976; Humphreys and Stewart 1972), but for larger dispersed particles, such as $\text{Al}_{20}\text{Cu}_2\text{Mn}_3$, this relaxation has been observed to occur by lattice rotations (Humphreys 1979). Modeling of the dislocation/particle interaction problem has been attempted using molecular dynamics (MD) simulations (Bacon and Osetsky 2005; Hatano 2006) and dislocation dynamics (DD) (Takahashi 2008; Queyreau and Devincre 2009). However, these are limited to small length and temporal scales for MD and small strain or single particles for DD.

The methods mentioned in the previous paragraph have limited capability in developing a predictive model, due to the fact that the dispersion of particles will vary in size and orientation within the matrix, which cannot be captured through the macroscopic models and limited simulations. Dislocation density based crystal plasticity finite element analysis has the capability of capturing the length and temporal scales applicable to the service conditions of these alloys, spanning strain-rates from the quasi-static to the high strain-rates (Elkhodary, Lee et al. 2011). Also, the effects of multiple particles can be investigated. However, the conventional techniques of this finite element method are unable to capture the interaction between the plastically deforming matrix and the elastic particle, due to the displacement compatibility requirements of the finite element method.

1.2 General Research Objectives and Approach

The goals of this research are to identify the microstructural features critical to the deformation behavior of the high strength Al-Cu-Mg-Ag-(Mn) alloy, and to develop a microstructurally based finite element methodology to properly account for the particle-matrix interaction which occurs in these alloys, allowing for a predictive simulation which can predict the microstructural behavior of these alloys under extreme loading conditions.

The effect of the microstructure on the ballistic performance of the alloy was investigated by means of optical microscopy (OM), scanning electron microscopy (SEM), transmission electron microscopy (TEM), and energy dispersive spectroscopy (EDS). Samples were taken from a 1.5” plate of ingot metallurgy (I/M) Al 2139 subjected to a 20 mm 4340 steel fragmentation simulating projectile impact ranging from 813 to 1043 m/s. Also, SEM investigation was performed on shear compression specimens (SCS) subjected to

split Hopkinson pressure bar impact testing at a strain-rate of approximately 2350 s^{-1} . The microstructural features of the alloy were identified, and the deformation and failure modes associated with each constituent were characterized.

Dislocation density based crystal plasticity finite element modeling was used to investigate the effects of the dispersed particles on the deformation behavior of the alloy. First, the effects of these particles and deformation on numerical instabilities in the finite element analysis were investigated, ensuring material instabilities could be delineated from numerical instabilities in subsequent results. A specialized finite element modeling scheme using an eigenstrain formulation to represent the unrelaxed plastic strain associated with Orowan looping was developed to investigate the effects of particle morphology, along with orientation, on the performance of the alloy from the quasi-static to the high strain-rate regimes. Emphasis was placed on the effects of the particles on the localization of the plastic shear slip and the influence of the particles on the stress state at the particle-matrix interface. The unrelaxed plastic strain associated with Orowan looping was represented as an eigenstrain in the particle as a function of the plastic strain in the surrounding matrix grain, calculated using dislocation density based crystal plasticity, which was relaxed by means of incompatible lattice rotations between the dispersed particle and the neighboring matrix grain.

The effects of particle dispersion and morphology were investigated by high strain-rate compressive simulations employing the eigenstrain based specialized dislocation density based crystalline plasticity and finite element framework. The coupled effects of the particles and grain boundary (GB) misorientations were also investigated using high strain-

rate compressive simulations, with emphasis placed on the effects of the particles and GB misorientations on experimentally observed failure modes.

1.3 Dissertation Organization

This dissertation is outlined as follows: Chapter 2 presents the results of microstructural characterization of high strength Al 2139 subjected to high strain-rate loading conditions. Chapter 3 contains the dislocation density based crystalline plasticity constitutive formulation, which is used in conjunction with the finite element numerical methods covered in Chapter 4. Chapter 5 presents the results of an investigation into the effects of deformation and microstructure on the hourglassing numerical instability associated with one-point Gauss integration in finite element analysis. Chapter 6 outlines the eigenstrain-based finite element formulation that accounts for unrelaxed plastic strains associated with Orowan loops and dispersed particles in high strength aluminum alloys. Chapter 7 covers an investigation into the effects of particle dispersion and orientation on the behavior of aluminum alloys subjected to quasi-static loading conditions. Chapter 8 expands on the investigation in Chapter 7 to model the effects of the particles under high strain-rate loading conditions. Chapter 9 presents an investigation into the interrelated effects of GB misorientation and dispersed particles on the possible failure modes in high strength aluminum alloys subjected to high strain-rate loading. Chapter 10 concludes the dissertation with recommendations for future research.

References—Chapter 1

- Atkinson, J. D., L. M. Brown, et al. (1974). “The Work-hardening of Copper-Silica IV. The Bauschinger Effect and Plastic Relaxation.” Philosophical Magazine **30**(6): 1247-1280.
- Bacon, D. J. and Y. N. Osetsky (2005). “Modeling Dislocation-Obstacle Interactions in Metals Exposed to an Irradiation Environment.” Materials Science and Engineering A **400**: 353-361.
- Brown, L. M. and W. M. Stobbs (1971a). “The Work-hardening of Copper-Silica I. A Model Based on Internal Stresses, With No Plastic Relaxation.” Philosophical Magazine, **23**(185): 1185-1199.
- Brown, L. M. and W. M. Stobbs (1971b). “The Work-Hardening of Copper-Silica II. The Role of Plastic Relaxation.” Philosophical Magazine **23**(185): 1201-1233.
- Brown, L. M. and W. M. Stobbs (1976). “The Work-Hardening of Copper-Silica V. Equilibrium Plastic Relaxation by Secondary Dislocations.” Philosophical Magazine **34**(3): 351-372.
- Chester, R. J. and I. J. Polmear (1980). “TEM Investigation of Precipitates in Al-Cu-Mg-Ag and Al-Cu-Mg Alloys.” Micron **11**(3-4): 311-312.
- Cho, A., W. B. Lisagor, et al. (2007). “Development and Processing Improvement of Aerospace Aluminum Alloys—Development of Al-Cu-Mg-Ag Alloy (2139).” NASA Contractor Report CR-2007-215094.
- Elkhodary, K. I., Lee, W. M., et al. (2011). “Deformation Mechanisms of an Ω Precipitate in a High Strength Aluminum Alloy Subjected to High Strain Rates,” Journal of Materials Research **26**(4): 487-497.
- Eshelby, J. D. (1957). “The Determination of the Elastic Field of an Ellipsoidal Inclusion, and Related Problems.” Proceedings of the Royal Society of London A **241**(1226): 376-396.
- Feng, W. X., F. S. Lin, et al. (1984). “The Effect of Minor Alloying Elements on the Mechanical Properties of Al-Cu-Li Alloys.” Metallurgical Transactions A **15**(6): 1209-1220.
- Hatano, T. (2008). “Dynamics of a Dislocation Bypassing an Impenetrable Precipitate: The Hirsch Mechanism Revisited.” Physics Review B **74**(2): 1-4.

- Hirsch, P. B. and F. J. Humphreys (1970). "The Deformation of Single Crystals of Copper and Copper-Zinc Alloys Containing Alumina Particles. II. Microstructure and Dislocation-Particle Interactions." Proceedings of the Royal Society of London A **318**(1532): 73-92.
- Humphreys, F. J. and P. B. Hirsch (1976). "Work-hardening and Recovery of Dispersion Hardened Alloys." Philosophical Magazine **34**(3): 373-390.
- Humphreys, F. J. and A. T. Stewart (1972). "Dislocation Generation at SiO₂ Particles in an α -Brass Matrix on Plastic Deformation." Surface Science **31**(1): 1972. 389-421.
- Humphreys, F. J. (1979). "Local Lattice Rotations at Second Phase Particles in Deformed Metals." Acta Metallurgica **27**(12): 1801-1814.
- Mura, T. (1987). Micromechanics of Defects in Solids (2nd ed.). The Netherlands, Martinus Nijhoff.
- Nie, J. F., B. C. Muddle, et al. (1996). "The Effect of Precipitate Shape and Orientation on Dispersion Strengthening in High Strength Aluminium Alloys." Materials Science Forum **217**: 1257-1262.
- Polmear, I. J. (2004). "Aluminum Alloys-A Century of Age Hardening." Materials Forum **28**: 1-14.
- Polmear, I. J. and R. J. Chester (1989). "Abnormal Age Hardening in an Al-Cu-Mg Alloy Containing Silver and Lithium." Scripta Metallurgica **23**(7): 1213-1218.
- Queyreau, S. and B. Devincere (2009). "Bauschinger effect in precipitation-strengthened materials: A dislocation dynamics investigation." Philosophical Magazine Letters **89**(7): 419-430.
- Starke, E. A. (1997). "NASA-UVa Light Aerospace Alloy and Structure Technology Program Supplement: Aluminum-Based Materials for High Speed Aircraft." NASA Contractor Report CR-97-206248.
- Starke, E. A., and T. H. Sanders (1980). "The Effect of Microstructure on the Properties of High Strength Aluminum Alloys." AFOSR Annual Scientific Report. ADA083768.
- Takahashi, A. (2008). "Parametric Dislocation Dynamics and Boundary Element Modeling of Elastic Interaction Between Dislocations and Precipitates." NATO Science for Peace and Security Series B - Physics and Biophysics 263-274.

Vaughan, D. (1968). "Grain Boundary Precipitation in an Al-Cu Alloy." Acta Metallurgica **16**(4): 563-577.

Walsh, J. A., J. V. Jata, et al. (1989). "The Influence of Mn Dispersoid Content and Stress State on Ductile Fracture of 2134 Type Al Alloys." Acta Metallurgica **37**(11): 2861-2871.

Chapter 2: Microstructural Characterization of a High Strength Aluminum Alloy Subjected to High Strain-Rate Impact

2.1 Introduction

Due to advances in heat treatments and metallurgical processing techniques, precipitate and dispersoid distributions have been used to increase strength and toughness in alloys, such as Al 2139 (Cho and Bes 2006), which can be applied for a myriad of civilian and military applications. This alloy has significant strength and ductility under high strain-rate loading conditions (Elkhodary, Sun et al. 2009) along with improved ballistic behavior in comparison with 7*** and 5*** series aluminum alloys previously used in military applications (Cheeseman, Gooch et al. 2008). Cho and Bes (2006) reported that strengthening constituents, precipitates Ω and θ' and Mn-containing dispersed particles, were present in the Al 2139 alloy. The composition and the quasi-static and dynamic properties of the alloy are given in Tables 2.1-2.2.

The precipitation of Ω (Al_2Cu) as plates on the $\{111\}_\alpha$ planes occurs in Al-Cu-Mg based alloys with high Cu:Mg ratios, and it can be enhanced by the presence of Ag (Polmear and Chester 1989; Gable, Shiflet et al. 2004; Wang, Starink et al. 2005; Chester and Polmear 1996). Plate-like precipitates on these planes have a greater impact on strengthening than precipitates on other planes in aluminum alloys (Nie, Muddle et al. 1996). A dislocation multiple cutting mechanism has also been proposed as one strengthening mechanism for the Ω precipitate under quasi-static loading (Li and Wawner 1998). The Ω precipitate nucleates more readily in the grain matrix than other precipitates (Cho and Bes 2006) without the

tendency for nucleation at dislocation lines or grain boundaries (GBs) (Chester and Polmear 1980; Garg, Chang et al. 1990).

The precipitate θ' (Al_2Cu) forms as plates on the $\{100\}_\alpha$ planes of Al-Cu based alloys with a tendency to precipitate on dislocation lines (Polmear and Chester 1989) and low angle GBs (Vaughan 1968). The strengthening mechanisms associated with θ' are dislocation pile-ups, dislocations adhering to the precipitate, and dislocations being impeded by the precipitates (Koda, Takahashi et al. 1963). Embury (1985) reported that “buckling” of θ' precipitates can occur at high strain levels under quasi-static, multi-directional loading conditions. Beffort et al. (1995) reported that while Ω precipitates can result in increased strength, θ' can result in increased fracture toughness for aluminum alloys.

The presence of Mn in the Al 2139 alloy can also promote the formation of orthorhombic dispersed particles with the composition of $\text{Al}_{20}\text{Cu}_2\text{Mn}_3$ that form as rods elongated in the [010] particle directions (Wang and Starink 2005). These particles have been reported to provide fiber-like reinforcement (Sharma, Amateau et al. 2005) and homogenization of slip through dislocation looping and grain size control (Walsh, Jata et al. 1989). Walsh, et al. (1989) noted that the effects of Mn addition, for quasi-static loading conditions, are governed by a competition between dispersed particles homogenizing deformation, which delays void coalescence, and decreased particle spacing of larger inclusions, which enhances void coalescence. The addition of Mn also reduces the detrimental effect on ductility of $\text{Al}_7\text{Cu}_2\text{Fe}$ inclusions (Tseng, Lee et al. 2002).

Most of the cited microstructural references have been for quasi-static loading regimes, and what has been lacking is an understanding of how the dynamic behavior of a

microstructurally complex aluminum alloy, such as Al 2139, can be affected at the different spatial scales that span the precipitates, the dispersoids, and the inclusions. Dynamic failure in ballistic testing can be caused by damage modes such as shear localization and bending tensile failure associated with discing failure due to high strain-rate loading as a result of projectile impact (Woodward 1984). The precipitates are at the nano scale, the dispersoids and inclusions are at the micro scales, and macroscopic failure modes and localized regions span the micro to macro scales. All of these microstructural characteristics can collectively affect failure evolution. Hence, the major objective of this chapter is to characterize the effects of this complex microstructure on the dynamic impact behavior of Al 2139.

2.2 Experimental Methods

2.2.1 Projectile Impact of a 1.5" (38 mm) plate

A 38 mm plate was subjected to a ballistic test with impact velocities ranging from 813 to 1043 m/s. The plate was impacted by 20 mm fragmentation simulating projectiles in accordance with the USADTC TOP 2-2-710 V_{50} test procedures at the Army Research Laboratory (Cheeseman, Gooch et al. 2008). The shots were fired with zero degrees striking obliquity. Figure 2.1 shows the backside of the plate after the test. Specimens were taken from both deformed and undeformed areas of the plate for comparison.

The broad spectrum of physical scales relevant to the microstructure of Al 2139 necessitated the need for multiple characterization approaches. Optical microscopy (OM), orientation imaging microscopy (OIM), energy dispersive spectroscopy (EDS), transmission electron microscopy (TEM), and selected area diffraction (SAD) were performed on undeformed and deformed samples. Scanning electron microscopy (SEM) was used for

characterization of fracture surfaces of the deformed samples. The focus of this study was to characterize grain size and morphology, dispersed particles and inclusions, and precipitates for deformed and undeformed states.

OM was used to investigate inclusions, grain sizes, and damage on the micro-scale. Samples were mechanically polished to either 1 μm alumina or 0.05 μm colloidal silica. Samples for grain size and damage characterization were etched using a 10 g NaOH to 100 mL H₂O mixture and viewed with a polarized light filter. Nikon Eclipse and Zeiss Axiovert microscopes along with Act-1 and Axiovision software were used for imaging. OIM was used to investigate grain orientations. Samples were polished to 0.5 μm alumina and characterized using an EDAX Hikari Electron Backscatter Diffraction (EBSD) detector on a Phillips XL30 FEG microscope. TEM imaging was used to view the microstructure of the alloy down to the nano-scale, including inclusions, dispersed particles, precipitates. A JEOL JEM-2000FX Electron Microscope and a Hitachi HF2000 TEM were used for imaging at 200 kV. An Oxford INCA EDS system accompanied the Hitachi TEM. A JEOL 2010F equipped with a GATAN Image Filter was used for phase-contrast HRTEM imaging at 200 kV. SEM was used to investigate fracture surfaces of the deformed areas down to the nano-scale. A Hitachi S-3200 SEM equipped with an Oxford Isis EDS system was used for characterization of the fracture surfaces.

Sample preparation methods were chosen as to preserve the microstructure and not induce any damage. Hence, waterjet cutting was used to section the material from the bulk plate. Further sectioning was accomplished using a low-speed diamond saw. TEM samples were prepared using electrochemical polishing. Samples were punched from a diamond-saw

cut foil, mechanically ground and polished to approximately 40 μm thick, and twin-jet polished with a nitric/methanol mixture at 243 K.

2.2.2 Split Hopkinson Impact of Shear Compression Specimens

Al 2139 shear compression specimens subjected to split Hopkinson testing at a strain-rate of 2350 s^{-1} were investigated. A 500 μm hole was drilled in the center of the gage area to localize the failure to the center of the gage area. A Hitachi S-3200 SEM equipped with an Oxford Isis EDS system was used for characterization of the fracture surfaces. Inclusions were distinguished from the dispersed particles by means of the characteristic Fe peak not present in the EDS spectrum of the dispersed particles.

2.3 Results and Discussion-Projectile Impact

2.3.1 Damage Modes

Damage modes similar to Woodward's observation of discing (Woodward 1984) were observed in both impacted areas of the plate that were penetrated and those that were not penetrated. A summary of the different damage modes is given in Figure 2.2 for a penetrated region. Petalling due to the initial impact was observed for all shots. Shear cracking on surfaces initially parallel to the impacted face was noted throughout the cross-section due to intense shear between the grains as the projectile passed through (Figure 2.3), as indicated by a crack running into shear bands. As the projectile continued to penetrate, bulging occurred in the backside of the plate due to a reduction in thickness of the material ahead of the projectile, which initiated shear cracking in planes normal to the impact. The bulging was elongated in the rolling direction. A mode of bending tensile failure was then

activated at the end of a shear crack. Shear punchout of the disc then occurred due to heavy shear parallel to the impact direction after the onset of bending tensile failure.

The extent of macroscopic damage, such as backside bulging and macroscopic cracking, was a function of the shot velocity; the two shots that completely penetrated the target corresponded with the two highest impact velocities. Cracking was observed on the backside of the plate parallel to the rolling direction, indicating more ductility and less damage in the R-S plane. This increased ductility can be attributed to the elongation of grains due to rolling. Therefore, damage in the R-S plane appeared to be the dominant factor for complete penetration of the material. It has been shown that two-directional rolling can increase the isotropy in the rolling and transverse directions for similar Al alloys (Cho, Lisagor et al. 2007).

2.3.2 Microstructural Characteristics

2.3.2.1 Grain Morphology

Grain shapes and sizes were characterized using Image J freeware analysis of microscopic images. The software fit an ellipse to each grain using the images of the GBs. Confidence intervals of the measurements presented are 95%. Grain morphology was highly dependent of both the orientation with respect to rolling and location in the through thickness of the plate. The dimensions of the grains at the edge of the plate were on average $59 \pm 4 \times 155 \pm 14 \times 230 \pm 25 \mu\text{m}$ (S x T x R directionality) and $65 \pm 6 \times 196 \pm 22 \times 400 \pm 55 \mu\text{m}$ at the middle of the plate. OIM analysis revealed that most of the GBs had high angle misorientations (with misorientations greater than 15°).

Grain elongation can lead to increases in dislocation densities in the rolling direction, which would increase the ductility in the rolled direction. This ductility corresponds to the greater amount of observed bulging in the rolling direction (Figure 2.1). Large grains also limit GB surface area, which would reduce GB cracking that can promote shear and spall failure. Hence, controlling the grain sizes near the edges of the plate could lead to greater resistance to the final bending failure and punchout of the disc. Also, reduced GB area along with high angle GBs limit the preferential precipitation of θ' (Vaughan 1968).

2.3.2.2 Dispersed Particles and Inclusions

EDS analysis indicated the presence of dispersoids containing Al, Cu, and Mn, along with the presence of inclusions containing Al, Cu, Fe, and Mn. Inclusions rich in Cu and Fe were also observed to a smaller extent. Standardless quantitative EDS analysis indicated that the Al-Cu-Mn dispersoids were near the composition of the $\text{Al}_{20}\text{Cu}_2\text{Mn}_3$ dispersoid. These particles averaged about 600 nm in length with an approximately 2:1 length to diameter ratio. The Al-Cu-Fe-Mn inclusions had a large concentration of Al and Cu (~70 and ~20 at. %) with smaller amounts of Fe and Mn (~6-7 and ~2-3 at. %). This could indicate that Mn substitutes for Fe in the $\text{Al}_7\text{Cu}_2\text{Fe}$ inclusions that are detrimental to the ductility of the aluminum alloys. It has been reported that the presence of Mn reduces the detrimental effects of Fe on aluminum alloys (Tseng, Lee et al. 2002). These particles were mainly larger than 1 μm , with individual particles as large as 25 μm and clusters approaching 100 μm . TEM observations show that approximately 30% of the sub-micron particles were Al-Cu-Fe-Mn inclusions with the rest being Al-Cu-Mn dispersoids.

The inclusions varied in shape and size as a function of the distance from the edge of the plate. Smaller equiaxed inclusions were observed near the edges of the plate, while larger inclusions, elongated in the rolling direction, were observed near the center of the plate. Some tendency was observed for these particles to grow along GBs. Analysis of OM images indicates a volume fraction of approximately 1.3% for the Al-Cu-Fe-Mn inclusions. Debonding occurred due to rolling to a small extent (~5% of particles) at the ends of elongation.

OM and SEM were used to compare the effects of the inclusions and dispersed particles on the high strain-rate failure of the alloy. The inclusions rotated with the matrix upon impact. Cracking was noted in the particles normal to the particle elongation direction, but did not extend into the matrix, indicating the ductility of the alloy and some energy absorption capability of the inclusions. Inclusion debonding, however, was observed in the elongated direction of smaller particles. Furthermore, the high Cu content of the inclusions reduces the amount of Cu available for precipitation of dispersed particles, Ω , and θ' .

The effects of dispersed particles and inclusions on the different failure modes of alloy Al 2139 on the micro-scale are shown in Figures 2.4-2.8. Figure 2.4 shows a shear crack caused by inclusion debonding that initiated at the particle-matrix interface. Figure 2.5 shows a cracked Al-Cu-Fe-Mn inclusion leading to shear failure in an area dominated by ductile failure. Figures 2.6 and 2.7 show the effect of the dispersed particles. Particles with the long axis in the plane of deformation are observed to be sources of void nucleation, due to the observation of the particles in the center of the dimples. Particles with the long axis inclined to the plane of deformation are observed on the ridges, indicating resistance to the

final failure due to void coalescence. The effects of particle dispersion on the void size at the time of failure can also be seen in this figure. The spacing between the particles determines the size of the voids. Figure 2.8 shows that inclusions also lead to increased void sizes in regions of ductile failure.

The interrelated associations of the dispersed particles and inclusions with the fracture of the alloy can give insights on the high strain-rate behavior of the alloy. First, the inclusions promote shear deformation, reducing the homogenizing effect of the dispersed particles. Secondly, dispersed particles in high strain-rate failure not only act as sites for void nucleation, but also resist coalescence of voids as clearly observed in Figure 2.7. The resistance to coalescence, furthermore, can lead to increased ductility for high strain-rate loading conditions.

2.3.2.3 Precipitates

TEM analysis of undeformed samples confirmed the presence of Ω and θ' in the Al 2139 alloy. Figure 2.9 is an SAD pattern taken on the $[011]$ beam axis, showing some breakup in the $[200]$ direction associated with the precipitation of θ' , and spots at $1/3$ and $2/3$ $[220]$ associated with Ω . Also, θ' precipitates can be identified in the images by the fringing that occurs due to the mismatch in the $(1-1\ 1)_\alpha$ and $(1-1\ 2)_{\theta'}$ diffraction spots. Analysis of on-axis TEM images reveals that the Ω precipitates average approximately 45 nm in diameter with a thickness of 2 nm, whereas the θ' precipitates are 35 nm in diameter with a thickness of 4 nm. The volume fraction of the precipitates was estimated to be 1.04% for Ω and 0.76% for θ' .

The deformation of the precipitates under high strain-rate impact loading is indicative of the dislocation activity associated with the impact. TEM images of precipitates were taken from a highly deformed region of the plate near the impact surface. Figure 2.10 shows both Ω and θ' precipitates in a DF image taken off of $\mathbf{B}=[011]$ with $\mathbf{g}=[200]$. Figure 2.11 is a HRTEM image of a deformed θ' precipitate. Figures 2.12 and 2.13 show HRTEM images of deformed Ω precipitates.

High strain-rate loading conditions can affect precipitate behavior. θ' precipitates, which form on the $\{100\}_\alpha$ planes, exhibit a wavy deformation mode (Figure 2.10). Also, as shown in Figure 11, the precipitates do not retain the plate-like shape and planar relationship with the matrix upon impact. The FFT inset clearly shows that the streak is rotated away from the $[200]$ direction.

In contrast with the θ' deformation, the $\{111\}_\alpha$ Ω precipitates deform in a manner in which they retain their planar shape, relationship, and coherency with the matrix through what is termed a dislocation multiple cutting mechanism (Li and Wawner 1998), due to the multiple indications of precipitate shearing (Figure 2.12). The shear cuts that are observed in Figure 2.13 are much larger than those observed by Li and Wawner (1998) for quasi-static testing. This multiple cutting mechanism can inhibit and diffuse localized shear, and the planar relationship and coherency with the matrix after impact is indicative of the beneficial effects that Ω precipitates have on the strength of the alloy. The dislocations cut through the precipitates, which indicates that the precipitates collectively promote ductility with minimal accumulations in interfacial stresses.

The distinct deformation modes of the precipitates are also crucial to understanding their relative impact on strengthening under high rates of strain. From these observations, two significant points can be made. First, the planar relationship with the matrix of Ω indicates that it can interact with multiple dislocations, increasing the strength of the matrix by resisting, but not preventing, dislocation motion without promoting shear localization. Hence, the extensive ductility of the aluminum can be sustained. Secondly, since the θ' precipitate can both deform in this wavy mode and lose its planar relationship with the matrix, it can rotate with the deformation. Increased precipitation of Ω in proportion to θ' , therefore, may lead to highly favorable ballistic performance of the alloy.

2.4 Results and Discussion-Split Hopkinson

Both shear dominant failure and dimpled void sheet failure are evident (Figure 2.14). Figure 2.14b also contains a region of shear failure within the dimpled void sheet region. The shear dominant failure is associated with the micro-scale Al-Cu-Fe-Mn inclusions. Figure 2.15a also indicates the inclusions are associated with the shear dominant failure. A cracked inclusion (see arrows) is present on the locally sheared fracture surface. The inclusions were also observed in the void sheet dimpled failure region (Figure 2.15b). The size of the dimples associated with the inclusions is approximately 10 μm , much larger than that of the surrounding void sheet.

The $\text{Al}_{20}\text{Cu}_2\text{Mn}_3$ dispersed particles were also observed to influence the failure of the alloy. Figure 2.16 shows the effect of the dispersed particles on the failure of the alloy. The dispersed particles were observed both in the center of the dimples and on the ridges. These images indicate dispersed particle orientation affects how the particle influences void

behavior. Particles with the long axis in the plane of deformation are observed in the center of the dimples. This suggests that these particles are sources of void nucleation. Particles with the long axis inclined to the plane of deformation are observed on the ridges. This is evidence that void initiation and final void coalescence can be delayed. These orientation effects on behavior are similar to those observed for ballistic impact testing. The effects of particle dispersion on the void size at the time of failure can also be seen in this figure. The spacing between the particles determines the size of the voids, which is on the order of 3 μm , which is much smaller than that associated with the Al-Cu-Fe-Mn inclusions.

2.5 Conclusions

The microstructure of Al 2139 plays a critical role in the high strain-rate performance and behavior of the alloy. Large, elongated grains reduce the GB area, which can lead to high ductility and toughness, especially in the rolling direction, and also increased resistance to shear and spall failure caused by GB cracking. Large grains with high angle GBs also allow for more precipitation of Ω and θ' within the grain interiors. Non-shearable dispersed particles associated with tensile failure increase the strength and ductility of the alloy by controlling void nucleation and inhibiting void coalescence. Larger inclusions can absorb energy, but may result in shear localization.

The different modes of deformation for the precipitates, Ω and θ' underscore how the interrelated effects of these precipitates affect behavior. The Ω precipitate maintains its planar relationship with the matrix through an extensive dislocation multiple cutting mechanism, reducing the tendency of shear localization without sacrificing ductility. The θ'

precipitates bend, buckle, and do not maintain the planar relationship with the matrix upon impact.

This study underscores how a high strength aluminum alloy such as Al 2139 can have significant strength and ductility for high strain-rate applications through interrelated microstructural strengthening and toughening mechanisms pertaining to the collective effects of precipitate deformation and distribution, dispersed particles, inclusions, and GB characteristics at physical scales spanning the nano to the micro. These mechanisms are directly linked to the inhibition of observed shear and tensile failure modes, resulting in increased resistance to projectile penetration and dynamic failure modes.

References—Chapter 2

- Beffort, O., C. Solenthaler, et al. (1995). "Improvement of Strength and Fracture Toughness of a Spray-Deposited Al-Cu-Mg-Ag-Mn-Ti-Zr Alloy by Optimized Heat-Treatments and Thermomechanical Treatments." Materials Science and Engineering A-Structural Materials Properties Microstructure and Processing **191**(1-2): 113-120.
- Cheeseman, B., W. Gooch, et al. (2008) "Ballistic Evaluation of Aluminum 2139-T8." 24th International Ballistics Symposium. New Orleans, LA.
- Chester, R. J. and I. J. Polmear (1980). "TEM Investigation of Precipitates in Al-Cu-Mg-Ag and Al-Cu-Mg Alloys." Micron **11**(3-4): 311-312.
- Cho, A. and B. Bes (2006). "Damage Tolerance Capability of an Al-Cu-Mg-Ag Alloy (2139)." Materials Science Forum **519-521**(1-2): 603-608.
- Cho, A., W. B. Lisagor, et al. (2007). "Development and Processing Improvement of Aerospace Aluminum Alloys—Development of Al-Cu-Mg-Ag Alloy (2139)." NASA Contractor Report CR-2007-215094.
- Elkhodary, K., L. Sun, et al. (2009). "Integrated Experimental, Atomistic, and Microstructurally Based Finite Element Investigation of the Dynamic Compressive Behavior of 2139 Aluminum." Journal of Applied Mechanics **76**(5): 051306.
- Embury, J. D. (1985). "Plastic Flow in Dispersion Hardened Materials." Metallurgical Transactions A **16**(12): 2191-2200.
- Gable, B. M., G. J. Shiflet, et al. (2004). "The Effect of Si Additions on Omega Precipitation in Al-Cu-Mg-(Ag) alloys." Scripta Materialia **50**(1): 149-153.
- Garg, A., Y. C. Chang, et al. (1990). "Precipitation of the Ω -Phase in an Al-4.0Cu-0.5Mg Alloy." Scripta Metallurgica et Materialia **24**(4): 677-680.
- Koda, S., S. Takahashi, et al. (1963). "Direct Observation of Interaction of Dislocations with θ' Precipitates in an Aluminium-3.8 Wt.-Percent Copper Alloy." Journal of the Institute of Metals **91**(7): 229-234.
- Lee, W. M. and M. A. Zikry (2011). "Microstructural Characterization of a High-Strength Aluminum Alloy Subjected to High Strain-Rate Impact." Metallurgical and Materials Transactions. A, Physical Metallurgy and Materials Science **42**(5): 1215-1221.

- Li, B. Q. and F. E. Wawner (1998). "Dislocation Interaction with Semicoherent Precipitates (Omega Phase) in Deformed Al-Cu-Mg-Ag alloy." Acta Materialia **46**(15): 5483-5490.
- Nie, J. F., B. C. Muddle, et al. (1996). "The Effect of Precipitate Shape and Orientation on Dispersion Strengthening in High Strength Aluminium Alloys." Materials Science Forum **217**: 1257-1262.
- Polmear, I. J. and R. J. Chester (1989). "Abnormal Age Hardening in an Al-Cu-Mg Alloy Containing Silver and Lithium." Scripta Metallurgica **23**(7): 1213-1218.
- Sharma, M. M., M. F. Amateau, et al. (2005). "Mesoscopic Structure Control of Spray Formed High Strength Al-Zn-Mg-Cu Alloys." Acta Materialia **53**(10): 2919-2924.
- Tseng, C. J., S. L. Lee, et al. (2002). "Effects of Manganese on Microstructure and Mechanical Properties of A206 Alloys Containing Iron." Journal of Materials Research **17**(9): 2243-2250.
- Vaughan, D. (1968). "Grain Boundary Precipitation in an Al-Cu Alloy." Acta Metallurgica **16**(4): 563-577.
- Walsh, J. A., J. V. Jata, et al. (1989). "The Influence of Mn Dispersoid Content and Stress State on Ductile Fracture of 2134 Type Al Alloys." Acta Metallurgica **37**(11): 2861-2871.
- Wang, S. C. and M. J. Starink (2005). "Precipitates and Intermetallic Phases in Precipitation Hardening Al-Cu-Mg-(Li) Based Alloys." International Materials Reviews **50**(4): 193-215.
- Woodward, R. L. (1984). "The Interrelation of Failure Modes Observed in the Penetration of Metallic Targets." International Journal of Impact Engineering **2**(2): 121-129.

Tables and Figures—Chapter 2

Table 2.1: Composition of Al 2139 (Cho and Bes 2006)

	Si	Fe	Cu	Mn	Mg	Ag
Percentage	0.10	0.15	4.5-5.5	0.20-0.60	0.20-0.80	0.15-0.60

Table 2.2: Effect of strain-rate on properties of Al 2139 (Elkhodary, Sun et al. 2009)

Strain-rate	0.001 s ⁻¹	8100 s ⁻¹
Flow Stress (MPa), $\epsilon_{\text{true}}=0.06$	650	850
True Strain to Failure	0.1	0.8

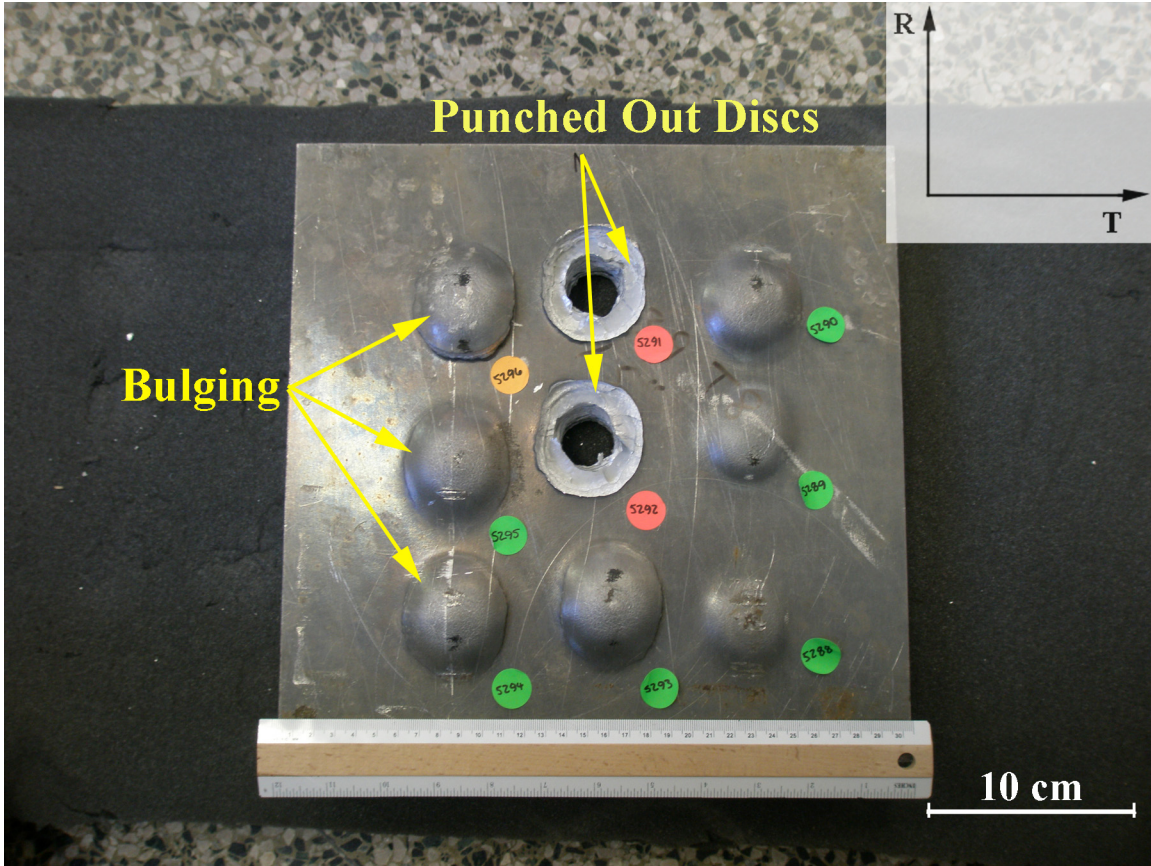


Figure 2.1: Backside of 1.5" (38 mm) plate of Al 2139 after V_{50} test showing bulging and disc punchout

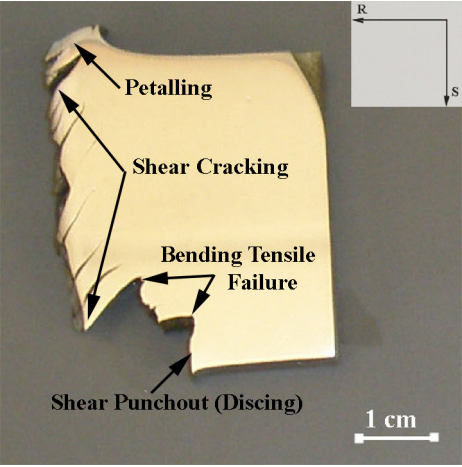


Figure 2.2: Polished cross-section indicating damage modes of penetrated region

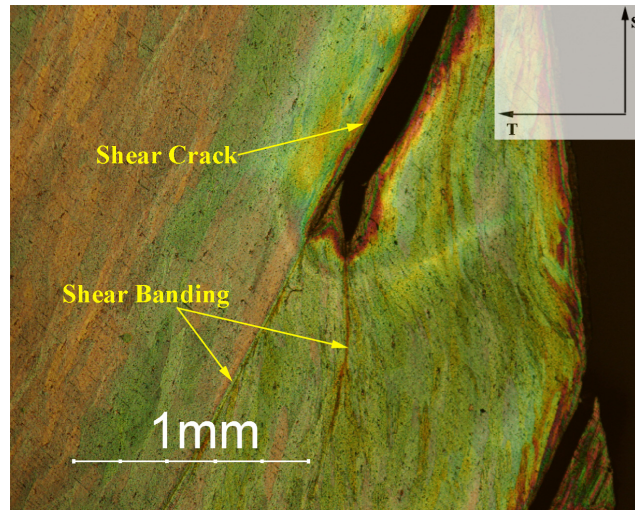


Figure 2.3: OM image of shear crack running into shear bands in a penetrated region

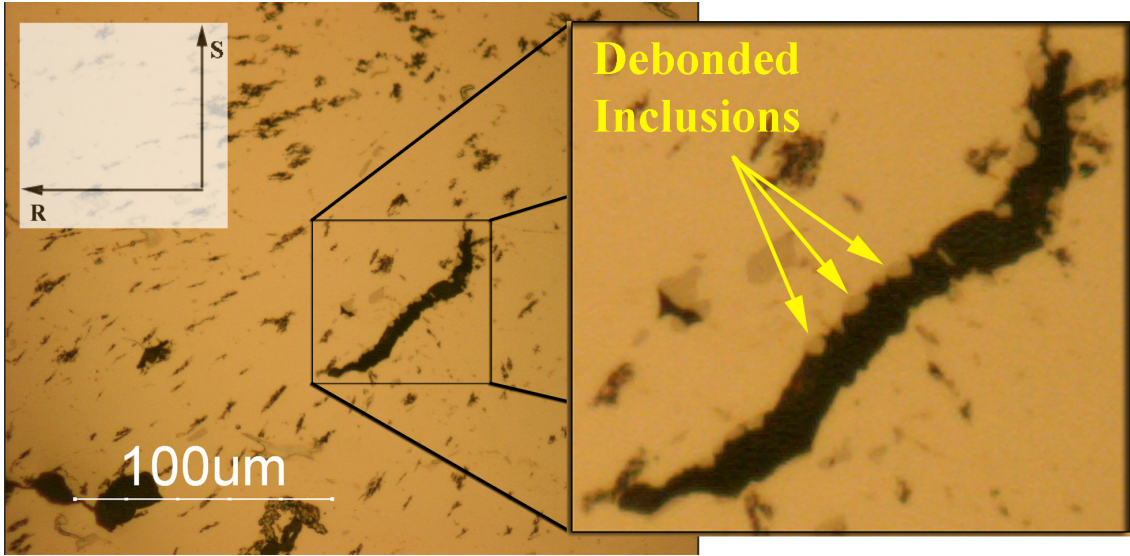


Figure 2.4: OM image of a shear crack due to particle debonding initiated at the matrix/inclusion interface

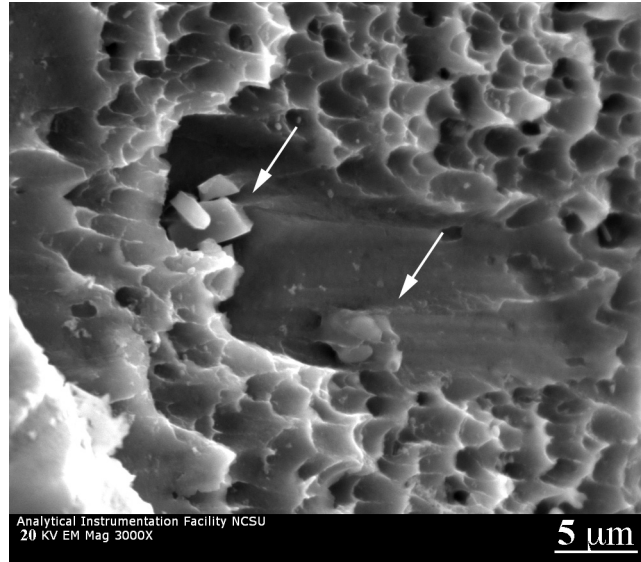


Figure 2.5: SEM image of a cracked Al-Cu-Fe-Mn inclusion promoting shear failure in an area of otherwise ductile failure

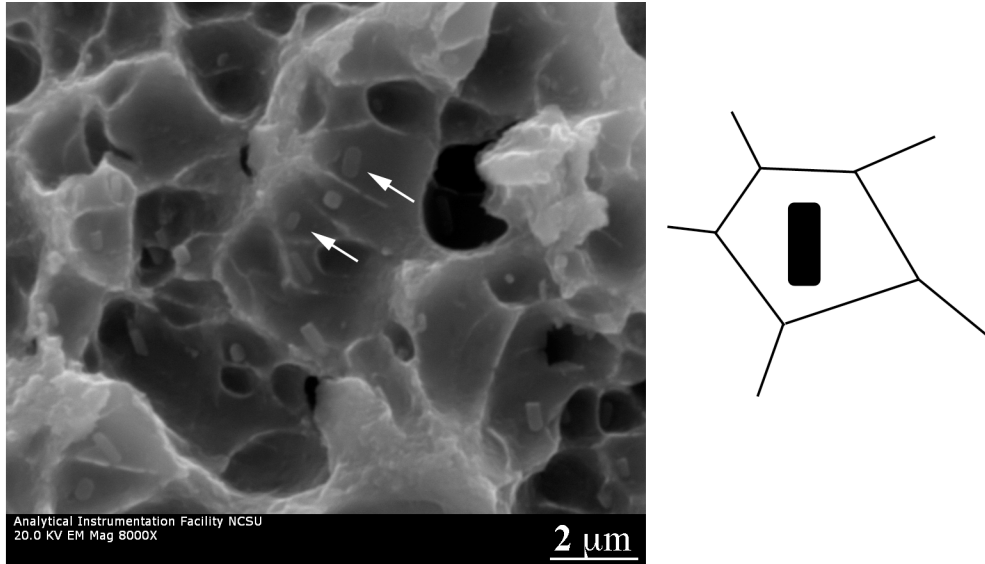


Figure 2.6: SEM image and schematic of dispersed particles in the center of dimples on a ductile fracture surface with the long axis of the particles in the plane of deformation, indicating void nucleation due to particles of this orientation

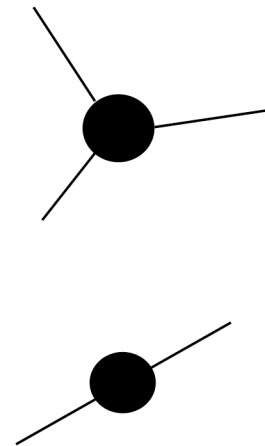
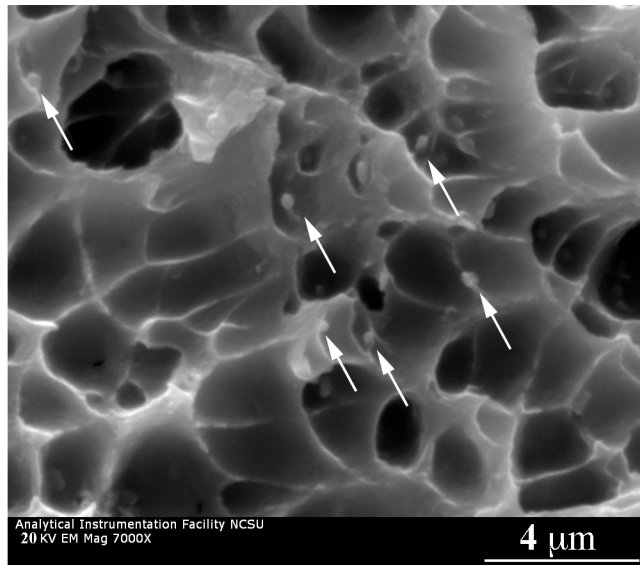


Figure 2.7: SEM image and schematic of dispersed particles on the ridges of a ductile fracture surface with the long axis of the particles inclined to the plane of deformation, indicating resistance to void coalescence and final failure

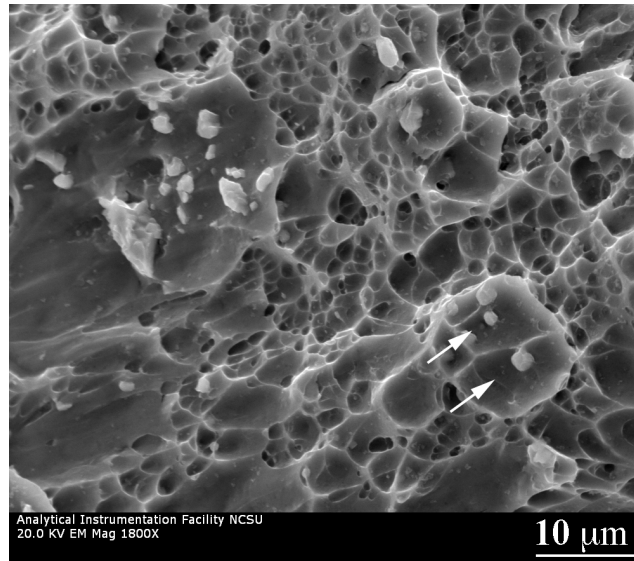


Figure 2.8: Comparison of the effects of inclusions and dispersed particles on a ductile fracture, showing larger void sizes associated with the inclusions (marked with arrows)

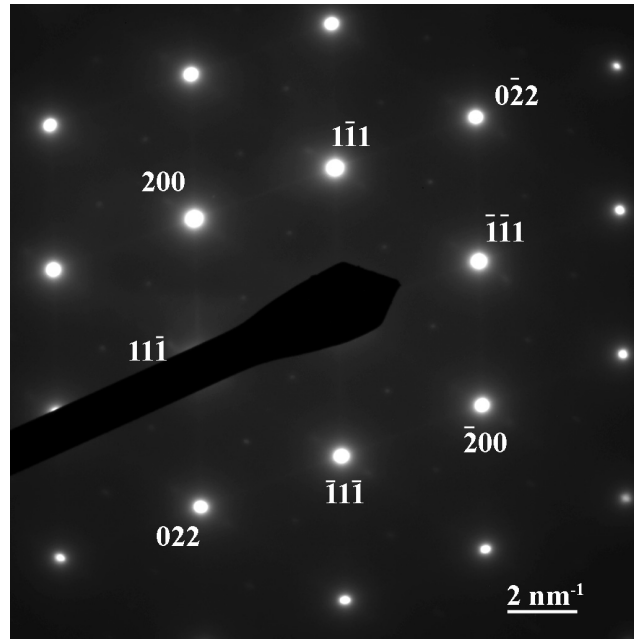


Figure 2.9: SAD pattern ($B=[011]$), of an undeformed specimen, showing some breakup in the $[200]$ direction associated with the precipitation of θ' and spots at $1/3$ and $2/3$ $[220]$ associated with Ω

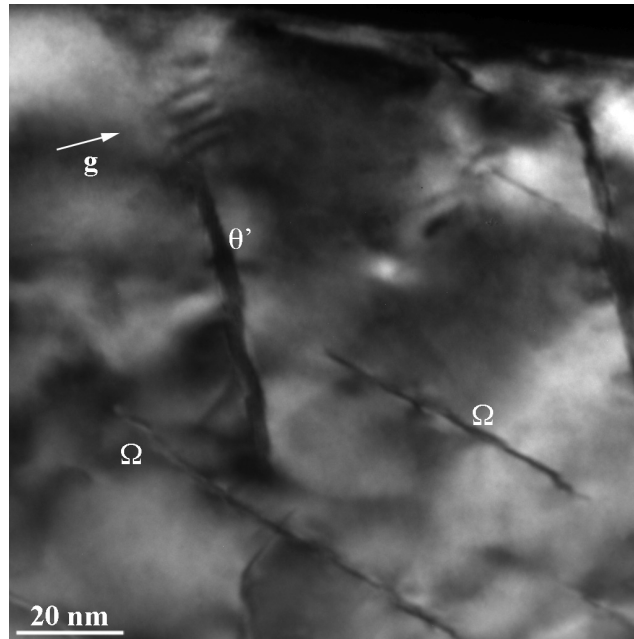


Figure 2.10: DF TEM image of Ω and θ' precipitates; $B=[011]$, $g=[200]$, showing a “wavy” deformation mode for θ' and a “multiple cutting” mechanism for Ω associated with the high strain-rate deformation

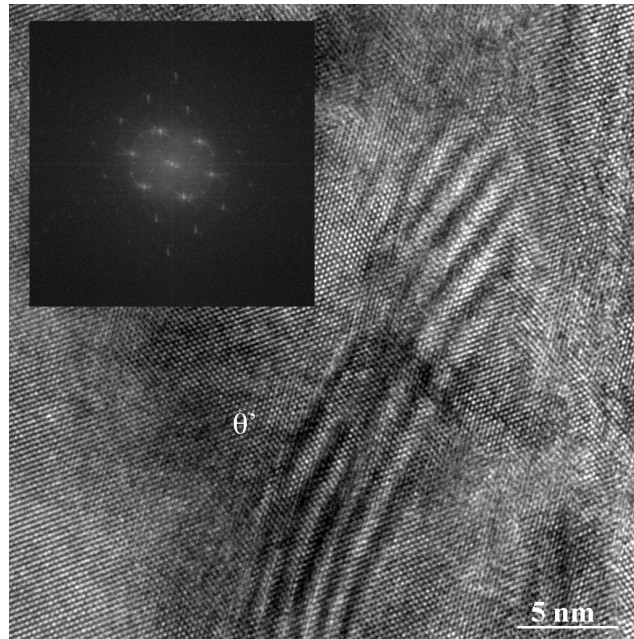


Figure 2.11: HRTEM image of a deformed θ' precipitate, $B=[011]$; FFT inset indicating precipitate can rotate away from matrix habit plane

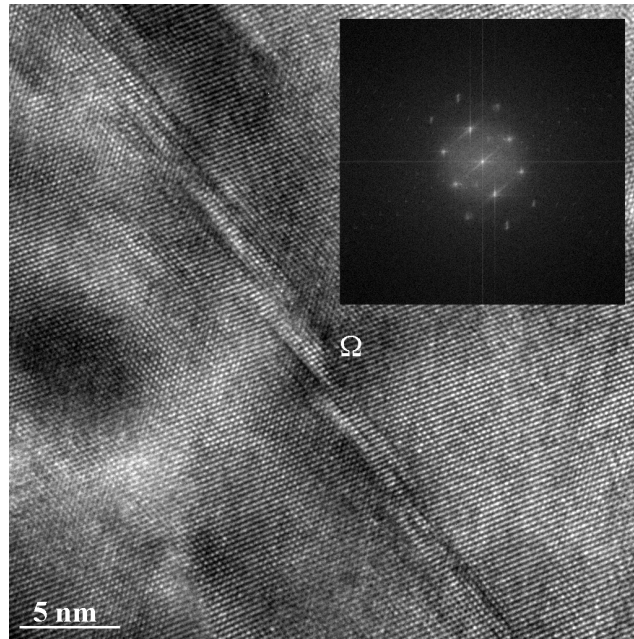


Figure 2.12: HRTEM image of a deformed Ω precipitate, $B=[011]$; FFT inset indicating uncut regions maintain planar relationship with matrix

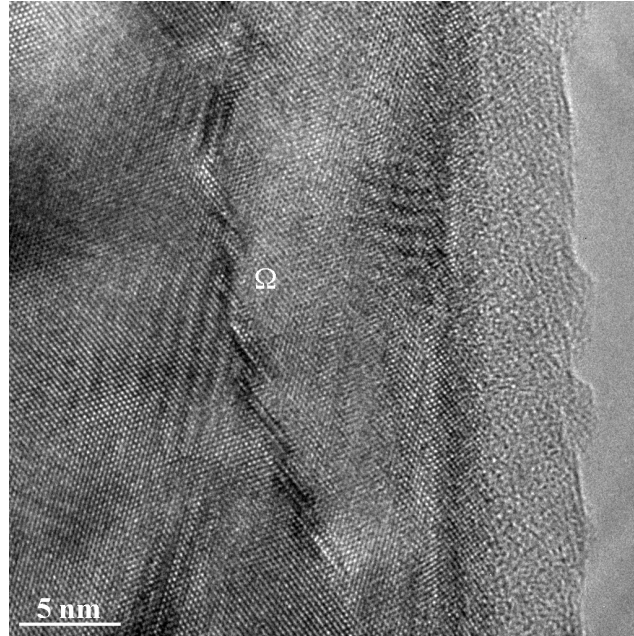
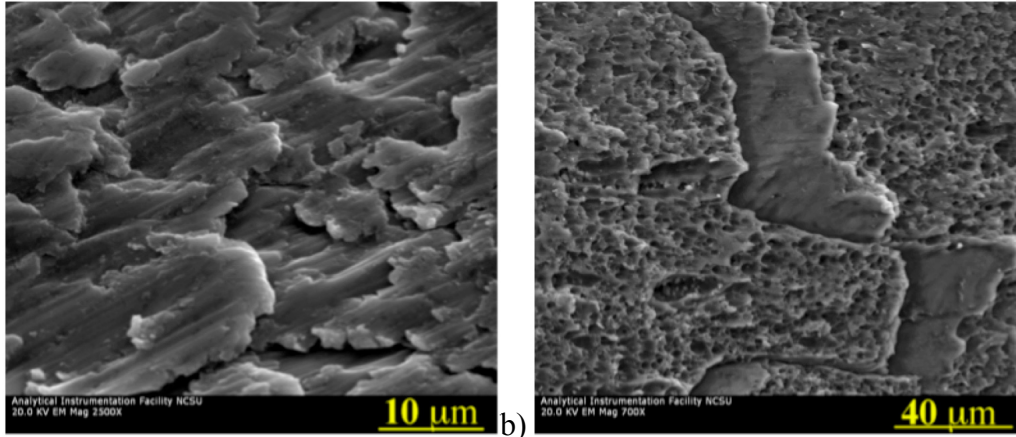


Figure 2.13: HRTEM image of a deformed Ω precipitate, $B=[011]$, showing extensive multiple cutting



a) Typical shear dominated fracture surface; b) Region of mostly void sheet dimpled rupture in the vicinity of shear dominated fracture for split Hopkinson testing

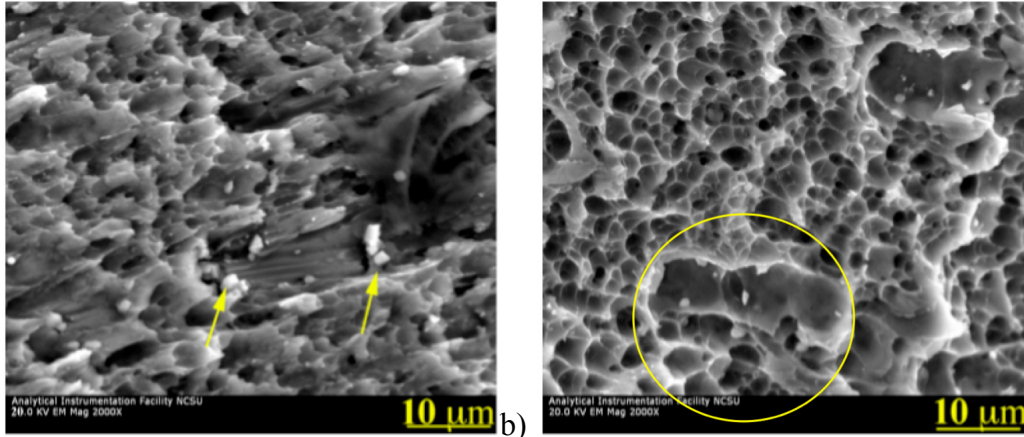
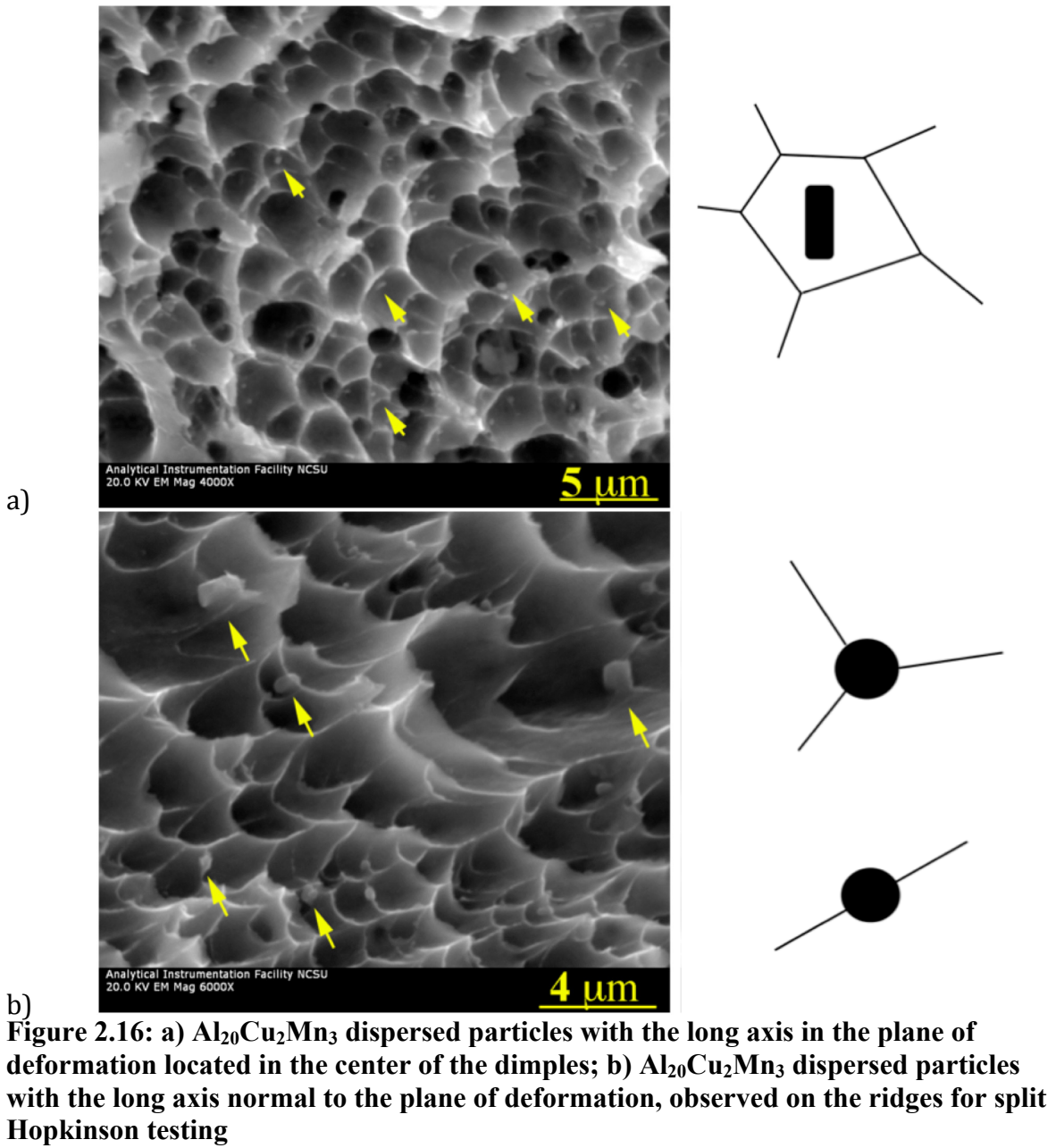


Figure 2.15: a) Al-Cu-Fe-Mn inclusion cracking and associated local shear fracture surface; b) Al-Cu-Fe-Mn inclusions associated with large dimples in area of dimpled void sheet failure for split Hopkinson testing



Chapter 3: Dislocation Density Based Crystalline Plasticity Constitutive Formulation

The observations presented in Chapter 2 are post-mortem observations; that is, no information regarding the evolution of the deformation mechanisms associated with the failure can be obtained. Specifically, how do a dispersion of the microstructural constituents, which deform in different manners, and the dislocation interactions with these constituents, affect the overall failure modes?

Dislocation density based crystalline plasticity finite element modeling can be employed to capture the effects of a dispersion of microstructural features on the evolution of the deformation behavior of the alloy (see, for instance, Elkhodary, Lee et al. 2011). The constitutive formulation for the dislocation density based crystalline plasticity finite element method will be presented in this chapter. The kinematics of multiple slip and the relationship between the material deformation and mechanical response associated with dislocation density accumulation and thermal softening will be outlined.

3.1 Multiple Slip Crystal Plasticity Kinematics

The constitutive formulation for rate-dependent multiple-slip crystalline plasticity, coupled to evolutionary equations for the dislocation densities, will be outlined below (Zikry and Kao 1996; Ashmawi and Zikry 2000; Asaro and Rice 1977).

The velocity gradient tensor, L_{ij} , is calculated from the deformation gradient as

$$L_{ij} = \dot{F}_{ij} F_{ij}^{-1}. \quad (3.1)$$

It is assumed that the velocity gradient can be additively decomposed into elastic and plastic parts, L_{ij}^e and L_{ij}^p . These will be further decomposed into the symmetric deformation rate tensors, D_{ij}^e and D_{ij}^p , and antisymmetric spin tensors, W_{ij}^e and W_{ij}^p , as

$$D_{ij} = D_{ij}^e + D_{ij}^p, \quad W_{ij} = W_{ij}^e + W_{ij}^p. \quad (3.2)$$

The plastic parts are related to the crystallographic slip rates as

$$D_{ij}^p = P_{ij}^{(\alpha)} \dot{\gamma}^{(\alpha)}, \quad W_{ij}^p = \omega_{ij}^{(\alpha)} \dot{\gamma}^{(\alpha)}, \quad (3.3)$$

where α is summed over all slip-systems, and $P_{ij}^{(\alpha)}$ and $\omega_{ij}^{(\alpha)}$ are the symmetric and antisymmetric parts of the Schmid tensor, defined in terms of the slip planes and directions as

$$P_{ij}^{(\alpha)} = \frac{1}{2} (s_i^{(\alpha)} n_j^{(\alpha)} + s_j^{(\alpha)} n_i^{(\alpha)}) \quad \text{and} \quad \omega_{ij}^{(\alpha)} = \frac{1}{2} (s_i^{(\alpha)} n_j^{(\alpha)} - s_j^{(\alpha)} n_i^{(\alpha)}). \quad (3.4)$$

As a measure of plastic strain, the effective plastic shear slip is calculated from the plastic deformation rate tensor as

$$\gamma_{eff} = \frac{2}{3} \int \sqrt{D_{ij}^p D_{ij}^p} dt. \quad (3.5)$$

The stress is updated using the Jaumann stress rate corotational with the lattice, $\sigma_{ij}^{\Delta,e}$, as

$$\sigma_{ij}^{\Delta,e} = C_{ijkl} D_{kl}^e, \quad (3.6)$$

where C_{ijkl} is the fourth-order isotropic elastic modulus tensor defined by

$$C_{ijkl} = \mu (\delta_{ik} \delta_{jl} + \delta_{jk} \delta_{il}) + \lambda \delta_{ij} \delta_{kl} \quad (3.7)$$

The Jaumann stress rate is related to the material stress rate, $\dot{\sigma}_{ij}$, in the reference coordinate system as

$$\dot{\sigma}_{ij} = \sigma_{ij}^{\Delta,e} + W_{ik}^e \sigma_{kj} + W_{jk}^e \sigma_{ki}. \quad (3.8)$$

Power law hardening is assumed, relating the slip rates on the various slip systems to the resolved shear stress as

$$\dot{\gamma}^{(\alpha)} = \dot{\gamma}_{ref}^{(\alpha)} \left[\frac{\tau^{(\alpha)}}{\tau_{ref}^{\alpha}} \right] \left[\left| \frac{\tau^{(\alpha)}}{\tau_{ref}^{\alpha}} \right| \right]^{(1/m)-1} \quad \text{no sum on } \alpha, \quad (3.9)$$

where $\dot{\gamma}_{ref}^{(\alpha)}$ is the reference shear strain-rate which corresponds to a reference shear stress, τ_{ref}^{α} , and m is the strain-rate sensitivity parameter,

$$m = \frac{\partial \ln \tau^{(\alpha)}}{\partial \ln \dot{\gamma}^{(\alpha)}}. \quad (3.10)$$

The reference shear stress includes forest hardening associated with the immobile dislocation density, which accounts for the interaction between slip systems through the coefficient, a_{cj} , and thermal softening through the negative thermal softening exponent, ξ , and reference temperature T_r (293 K) (Franciosi, Berveiller et al. 1980).

$$\tau_{ref}^{\alpha} = \left(\tau_s^{\alpha} + \mu b \sum_{j=1, nss} \sqrt{a_{cj} \rho_{im}^j} \right) \left(\frac{T}{T_r} \right)^{\xi} \quad (3.11)$$

For high strain-rate investigations under the assumption of adiabatic heating, the temperature is updated using

$$\dot{T} = \frac{\chi}{\rho c_p} \sigma_{ij}^{\dot{}} D_{ij}^p, \quad (3.12)$$

where χ is the fraction of plastic work converted to heat, ρ is the mass density, c_p is the specific heat of the material, and $\sigma_{ij}^{\dot{}}$ is the deviatoric stress.

3.2 Dislocation Density Evolution

It will be assumed that the total dislocation density can be decomposed additively into mobile and immobile components (Zikry and Kao 1996).

$$\rho^{(\alpha)} = \rho_{im}^{(\alpha)} + \rho_m^{(\alpha)} \quad (3.13)$$

During an increment of slip, mobile dislocations may be generated, immobile dislocations may be annihilated, or junctions may be formed or destroyed coupling the mobile and immobile dislocation densities, leading to the coupled differential equations governing dislocation density evolution,

$$\dot{\rho}_m^{(\alpha)} = \dot{\rho}_{generation}^{(\alpha)} - \dot{\rho}_{interaction-}^{(\alpha)} \quad (3.14)$$

$$\dot{\rho}_{im}^{(\alpha)} = \dot{\rho}_{interaction+}^{(\alpha)} - \dot{\rho}_{annihilation}^{(\alpha)}. \quad (3.15)$$

The dislocation density evolution follows the formulation of Shanthraj and Zikry (Accepted). Dislocation density generation is related to the distance, y_{back} , traversed by a dislocation emitted from a source with density, ρ_{source} , both related to the spacing of immobile forest obstacles, i.e., Frank Read mechanism. The average velocity of mobile dislocations, $v^{(\alpha)}$, is used to determine the generation rate as

$$\dot{\rho}_{generation} = \rho_{source}^{(\alpha)} \frac{v^{(\alpha)}}{y_{back}}. \quad (3.16)$$

The Orowan equation, $\dot{\gamma}^{(\alpha)} = \rho_m^{(\alpha)} b^{(\alpha)} v^{(\alpha)}$, allows the generation rate to be recast as

$$\dot{\rho}_{generation} = \frac{\phi \sum_{\beta} \sqrt{\rho_{im}^{(\beta)}}}{b^{(\alpha)}} \left(\frac{\rho_{im}^{(\alpha)}}{\rho_m^{(\alpha)}} \right) \dot{\gamma}^{(\alpha)}, \quad (3.17)$$

where ϕ is a geometric parameter and $b^{(\alpha)}$ is the magnitude of the Burger's vector on slip system α .

Dislocation density interaction involves the immobilization of mobile dislocation segments due to junction formation that occurs when dislocation densities on different slip systems interact. The frequencies of interaction between mobile dislocation densities on slip system α and mobile and immobile dislocations on slip system β are defined as $\rho_m^{(\alpha)}\rho_m^{(\beta)}v^{(\alpha\beta)}$ and $\rho_m^{(\alpha)}\rho_{im}^{(\beta)}v^{(\alpha)}$, where the relative velocity between the slip systems, $v^{(\alpha\beta)}$, is defined using the Orowan equation as

$$v^{(\alpha\beta)} = \frac{\dot{\gamma}^{(\alpha)}}{\rho_m^{(\alpha)}b^{(\alpha)}} + \frac{\dot{\gamma}^{(\beta)}}{\rho_m^{(\beta)}b^{(\beta)}}. \quad (3.18)$$

The length of the formed junction is assumed to be proportional to the spacing of immobile dislocations as

$$l_c = \frac{1}{\sum_{\beta} \sqrt{\rho_{im}^{(\beta)}}}, \quad (3.19)$$

and only a fraction of these junctions, f_0 , are stable. The rates of immobilization of dislocation densities on slip system α due to mobile and immobile dislocations on slip system β are therefore $f_0\rho_m^{(\alpha)}\rho_m^{(\beta)}l_c v^{(\alpha\beta)}$ and $f_0\rho_m^{(\alpha)}\rho_{im}^{(\beta)}l_c v^{(\alpha)}$, respectively. The rate of immobilization of mobile dislocation densities on slip system α is therefore

$$\dot{\rho}_{interaction-}^{(\alpha)} = f_0 \sum_{\beta} \left(\rho_m^{(\beta)} l_c \frac{\dot{\gamma}^{(\alpha)}}{b^{(\alpha)}} + \rho_m^{(\alpha)} l_c \frac{\dot{\gamma}^{(\beta)}}{b^{(\beta)}} \right) + f_0 \sum_{\beta} \rho_{im}^{(\beta)} l_c \frac{\dot{\gamma}^{(\alpha)}}{b^{(\alpha)}} \quad (3.20)$$

The addition of immobile dislocation densities due to interactions also takes into account the possibility of dislocation interaction forming immobile junctions. Frank's rule is

used to determine energetically favorable interactions for immobile junction formation. A dislocation density interaction tensor for junction formation on slip system α due to interaction of slip systems β and γ is defined as

$$n_{\alpha}^{\beta\gamma} = \begin{cases} 1 & \text{if } \mu b^{(\alpha)2} < \mu b^{(\beta)2} + \mu b^{(\gamma)2} \text{ and } b^{(\alpha)} = b^{(\beta)} + b^{(\gamma)} \\ 0 & \text{otherwise} \end{cases}. \quad (3.21)$$

The rates of junction formation on slip system α are then defined as

$$n_{\alpha}^{\beta\gamma} f_0 \rho_m^{(\beta)} \rho_m^{(\gamma)} l_c v^{(\beta\gamma)} \quad \text{and} \quad n_{\alpha}^{\beta\gamma} f_{\beta\gamma} l_c \left(\rho_m^{(\beta)} \rho_{im}^{(\gamma)} v^{(\beta)} + \rho_m^{(\gamma)} \rho_{im}^{(\beta)} v^{(\gamma)} \right) \quad (3.22)$$

for mobile/mobile and mobile/immobile interactions. The total addition of immobile dislocation densities due to interactions then becomes

$$\dot{\rho}_{interaction+}^{(\alpha)} = f_0 \sum_{\beta,\gamma} \left(\rho_m^{(\beta)} l_c \frac{\dot{\gamma}^{(\gamma)}}{b^{(\gamma)}} + \rho_m^{(\gamma)} l_c \frac{\dot{\gamma}^{(\beta)}}{b^{(\beta)}} \right) + f_0 \sum_{\beta,\gamma} \left(\rho_{im}^{(\beta)} l_c \frac{\dot{\gamma}^{(\gamma)}}{b^{(\gamma)}} + \rho_{im}^{(\gamma)} l_c \frac{\dot{\gamma}^{(\beta)}}{b^{(\beta)}} \right). \quad (3.23)$$

The interaction tensor for FCC crystals is determined using the 6 energetically favorable interactions: self interaction, co-linear interaction, co-planar interaction, Lomer locks, glissile junctions, Hirth locks (Kubin, Devincere et al. 2008). Table 3.1 summarizes these interactions.

Dislocation density annihilation due to recovery is modeled using an Arrhenius relationship (Vegge, Rasmussen et al. 2000) as

$$\dot{\rho}_{annihilation}^{(\alpha)} = v^{(\alpha)} e^{\left(\frac{-H}{kT}\right)}, \quad (3.24)$$

where the frequency of which immobile dislocations are intersected by mobile dislocations on other slip systems is related to the attempt frequency, $v^{(\alpha)}$, as

$$v^{(\alpha)} = f_0 \sum_{\beta} \rho_{im}^{(\alpha)} l_c \frac{\dot{\gamma}^{(\beta)}}{b^{(\beta)}}. \quad (3.25)$$

The activation enthalpy, H , is related to the immobile dislocation density and saturation density, ρ_s , as

$$H = H_0 \left(1 - \sqrt{\frac{\rho_{im}^{(\alpha)}}{\rho_s}} \right). \quad (3.26)$$

The annihilation rate of dislocation densities on slip system α becomes

$$\dot{\rho}_{annihilation}^{(\alpha)} = \left(f_0 \sum_{\beta} \rho_{im}^{(\alpha)} l_c \frac{\dot{\gamma}^{(\beta)}}{b^{(\beta)}} \right) e^{\left(\frac{-H_0 \left(1 - \sqrt{\frac{\rho_{im}^{(\alpha)}}{\rho_s}} \right)}{kT} \right)}. \quad (3.27)$$

The generation, interaction, and annihilation rates are then substituted into equations 3.14 and 3.15 to obtain a coupled nonlinear set of evolutionary equations for the dislocation densities. The evolutionary equations can be expressed as

$$\frac{d\rho_m^\alpha}{dt} = \dot{\gamma}^\alpha \left(\frac{g_{sour}^\alpha}{b^2} \left(\frac{\rho_{im}^\alpha}{\rho_m^\alpha} \right) - g_{minter}^\alpha \rho_m^\alpha - \frac{g_{immob-}^\alpha}{b} \sqrt{\rho_{im}^\alpha} \right) \quad (3.28)$$

$$\frac{d\rho_{im}^\alpha}{dt} = \dot{\gamma}^\alpha \left(g_{minter+}^\alpha \rho_m^\alpha + \frac{g_{immob+}^\alpha}{b} \sqrt{\rho_{im}^\alpha} - g_{re cov}^\alpha \rho_{im}^\alpha \right) \quad (3.29)$$

to delineate the dislocation activities such as generation, interaction, immobilization, and annihilation (Zikry and Kao 1996). The coefficients, not known a priori, are summarized in Table 3.2. The dislocation activity is coupled to the stress response through the Taylor relationship (eq. 3.11).

References—Chapter 3

- Asaro, R. J. and J. R. Rice (1977). “Strain Localization in Ductile Single-Crystals.” Journal of the Mechanics and Physics of Solids **25**(5): 309-338.
- Ashmawi, W. M. and M. A. Zikry (2000). “Effects of Grain Boundaries and Dislocation Density Evolution on Large Strain Deformation Modes in FCC Crystalline Materials.” Journal of Computer-Aided Materials Design **7**(1): 55-62.
- Elkhodary, K. I., Lee, W. M., et al. (2011). “Deformation Mechanisms of an Ω Precipitate in a High Strength Aluminum Alloy Subjected to High Strain-rates,” Journal of Materials Research **26**(4): 487-497.
- Franciosi, P., M. Berveiller, et al. (1980). “Latent Hardening in Copper and Aluminum Single Crystals.” Acta Metallurgica **28**(3): 273-283.
- Kubin, L., B. Devincere, et al. (2008). “Modeling Dislocation Storage Rates and Mean Free Paths in Face-Centered Cubic Crystals.” Acta Materialia **56**(20): 6040-6049.
- Shanthraj, P. and M. A. Zikry “Dislocation Density Evolution and Interactions in Crystalline Materials.” Acta Materialia Accepted.
- Vegge, T., T. Rasmussen, et al. (2000). “Determination of the Rate of Cross Slip of Screw Dislocations.” Physical Review Letters **85**(18): 3866-3869.
- Zikry, M. A. and M. Kao (1996). “Inelastic Microstructural Failure Mechanisms in Crystalline Materials with High Angle Grain Boundaries.” Journal of the Mechanics and Physics of Solids **44**(11): 1765–1798.

Tables and Figures—Chapter 3

Table 3.1: Summary of interactions and coefficient values in an FCC crystal

Interaction type	Dissipation ($\propto \sqrt{a_{ij}}$)	a_{ij}	a_{ij} from [Kubin, et al., 2008]
Self	$2kGb^2$	0.6	-
Co-linear	$2kGb^2$	0.6	0.625
Lomer lock	kGb^2	0.15	0.122
Glissile junction	kGb^2	0.15	0.137
Co-planar	kGb^2	0.15	0.122
Hirth lock	0	0.00	0.045

Table 3.2: Summary of g-coefficients for dislocation density evolution equations

g Coefficients	Expression
g_{sour}^{α}	$b^{\alpha} \phi \sum_{\beta} \sqrt{\rho_{im}^{\beta}}$
g_{mter-}^{α}	$l_c f_0 \sum_{\beta} \left[\frac{\rho_m^{\beta}}{\rho_m^{\alpha} b^{\alpha}} + \frac{\dot{\gamma}^{\beta}}{\dot{\gamma}^{\alpha} b^{\beta}} \right]$
g_{immob-}^{α}	$\frac{l_c f_0}{\sqrt{\rho_{im}^{\alpha}}} \sum_{\beta} \rho_{im}^{\beta}$
g_{mter+}^{α}	$\frac{l_c f_0}{\dot{\gamma}^{\alpha} \rho_m^{\alpha}} \sum_{\beta, \gamma} n_{\alpha}^{\beta \gamma} \left[\frac{\rho_m^{\gamma} \dot{\gamma}^{\beta}}{b^{\beta}} + \frac{\rho_m^{\beta} \dot{\gamma}^{\gamma}}{b^{\gamma}} \right]$
g_{immob+}^{α}	$\frac{l_c f_0}{\dot{\gamma}^{\alpha} \sqrt{\rho_{im}^{\alpha}}} \sum_{\beta} n_{\alpha}^{\beta \gamma} \rho_{im}^{\gamma} \dot{\gamma}^{\beta}$
$g_{re cov}^{\alpha}$	$\frac{l_c f_0}{\dot{\gamma}^{\alpha}} \left(\sum_{\beta} \frac{\dot{\gamma}^{\beta}}{b^{\beta}} \right) e^{\left(\frac{-H_0 \left(1 - \sqrt{\frac{\rho_m^{\alpha}}{\rho_s}} \right)}{kT} \right)}$

Chapter 4: Numerical Methods

The stress state of the crystalline materials can be updated by means of the constitutive relationship prescribed in Chapter 3 once the total velocity gradient, L_{ij} , and plastic velocity gradient, L_{ij}^P , are known. The specialized finite element scheme implemented for the determination of the velocity gradient tensors will be outlined below.

4.1 Determination of the Total Velocity Gradient

The total velocity gradient can be obtained by means of finite element analysis. For quasi-static analysis, an incremental, iterative approach taking advantage of the quasi-Newton BFGS scheme is used to determine the nodal displacements. For dynamic analyses, an implicit Newmark- β , iterative approach using BFGS to solve the finite element equations linearized about t_n at each timestep is used. Trapezoidal values of $\beta = 1/4$ and $\gamma = 1/2$ were chosen for unconditional stability of the finite element method. The deformation calculated by the finite element method is used to calculate the total velocity gradient in accordance with eq. 3.1.

To avoid numerical locking due to incompressibility pressure constraints, reduced 1-point integration of the Q4 quadrilateral element is used, which has the added benefit of reduced computational time. However, reduced integration can lead to the zero-energy numerical instability of hourglassing. Stiffness-based hourglass control, which will be outlined below, is implemented to control the hourglass instability (Belytschko, Liu et al. 2000).

Following the method of Flanagan and Belytschko (1981), an hourglass base vector $\mathbf{h}^T = [1 \ -1 \ 1 \ -1]$ is used to describe the hourglass mode for a one point integrated Q4 element. The hourglass shape vector, which is orthogonal to the linear velocity field when defined in the corotational frame, is

$$\gamma_i = \frac{1}{4} [\mathbf{h} - (\mathbf{h}^T \mathbf{x}_i) \mathbf{b}_i], \quad i = x, y, \quad (4.1)$$

where \mathbf{b}_i are the shape function derivatives, and \mathbf{x}_i are the nodal coordinates. The generalized hourglass velocity strains are given in terms of the nodal velocities, \mathbf{v}_i , as (expressed in the corotational frame)

$$\dot{q}_x = \gamma^T \mathbf{v}_x \text{ and } \dot{q}_y = \gamma^T \mathbf{v}_y. \quad (4.2)$$

For stiffness based hourglass control, generalized hourglass stress rates are defined as

$$\dot{Q}_x = C^Q \dot{q}_x \quad \text{and} \quad \dot{Q}_y = C^Q \dot{q}_y, \quad (4.3)$$

The stress rates are integrated and used to augment the force vector through a stabilization force,

$$\mathbf{f}^{stab} = A \begin{Bmatrix} Q_x \gamma \\ Q_y \gamma \end{Bmatrix} \quad (4.4)$$

where A is the element area. A corresponding stabilization augments the stiffness matrix as

$$\mathbf{K}_e = \mathbf{K}_{e,1pt} + C^Q A \begin{bmatrix} \gamma\gamma^T & \gamma\gamma^T \\ \gamma\gamma^T & \gamma\gamma^T \end{bmatrix} \quad (4.5)$$

The coefficient for the stabilization force and stiffness is defined as

$$C^Q = \frac{1}{2} \alpha_s c^2 \rho A \mathbf{b}_i^T \mathbf{b}_i, \quad (4.6)$$

where the input parameter is α_s , and c is the shear wavespeed of the material. An effective modulus is used to account for the lower wavespeed of plastic elements as follows (Abaqus Users Manual):

$$\frac{\Delta\sigma_{ij}/3}{D_{ij}dt}; \quad \hat{\mu} = \frac{1}{2} \frac{\hat{\sigma}_{ij}^{el} D_{ij}}{D_{ij} D_{ij}}; \quad \hat{\lambda} = \hat{\kappa} - \frac{2}{3} \hat{\mu} \quad (4.7)$$

$$c = \sqrt{\frac{(\hat{\lambda} + 2\hat{\mu})}{\rho}}. \quad (4.8)$$

4.2 Determination of the Plastic Velocity Gradient

The objective stress rate is coupled with the time derivative of the resolved shear stresses to determine the resolved shear stresses on each slip plane.

$$\dot{\tau}^{(\alpha)} = \frac{d}{dt} (P_{ij}^{(\alpha)} \sigma_{ij}) \quad (4.9)$$

$$\dot{\tau}^{(\alpha)} = C_{ijkl} P_{ij}^{(\alpha)} D_{kl}^{el} \quad (4.10)$$

Eq. 4.10 can be expanded to

$$\dot{\tau}^{(\alpha)} = 2\mu P_{ij}^{(\alpha)} \left[D_{ij} - \sum_{\xi=1, nss} P_{ij}^{(\xi)} \dot{\gamma}_{ref}^{(\xi)} \left(\frac{\tau^{(\xi)}}{\tau_{ref}^{(\xi)}} \right)^{\frac{1}{m}} \right], \quad (4.11)$$

where the reference stress is a function of the immobile dislocation density. The slip rates can be determined using the resolved shear stress (eq. 3.9). The plastic deformation rate tensor and spin rate tensor can then be used along with the Schmid tensor and slip rates to determine the plastic velocity gradient (eq. 3.3).

The elastic spin rate tensor can be determined as a function of the total spin rate tensor and the plastic spin rate tensor using eq. 3.2. It was assumed in the derivation of eq.

4.11 that the time rate of change of the slip normals and directions is related to the lattice spin as

$$\dot{n}_i^{(\alpha)} = W_{ij}^{el} n_j \quad \text{and} \quad \dot{s}_i^{(\alpha)} = W_{ij}^{el} s_j. \quad (4.12)$$

4.3 Solution of Systems of ODE's

The non-linear ODE's governing the resolved shear stresses and dislocation density evolution necessitate a solution method that is both accurate and stable due to their non-linear nature and the possibility of numerical stiffness (Zikry 1994). The non-linear nature of the problem requires a solution method with high order accuracy, while the possibility of numerical stiffness requires a solution method that is stable and will not propagate error due to stiff behavior.

An adaptive timestep fifth-order accurate step halving Runge-Kutta method is employed. Two approximate solutions are taken using the fourth-order Runge-Kutta method, one at step length h and a second with two steps of length $h/2$.

$$\tau(t+h) = \hat{\tau}_1 + (h)^5 \phi + O(h^6) + \dots \quad (4.13)$$

$$\tau(t+2(h/2)) = \hat{\tau}_2 + 2(h/2)^5 \phi + O(h^6) + \dots \quad (4.14)$$

The two solutions are combined to yield

$$\tau(t+h) = \hat{\tau}_2 + \frac{\Delta_1}{15} + O(h^6), \quad (4.15)$$

where $\Delta_1 = \hat{\tau}_1 - \hat{\tau}_2$ is the local truncation error, which is used to measure the accuracy of the solution. If the accuracy is not less than a specified tolerance, Δ_0 , the timestep size is reduced by

$$h_{new} = F h_{old} \left| \frac{\Delta_0}{\Delta_1} \right|^{0.20}, \quad (4.16)$$

where h_{new} is the new timestep size, h_{old} is the initial timestep size, and F is used to keep the new timestep small enough to be accepted.

When the timestep is becomes excessively small, the timestep restriction can be due to stability issues caused by numerical stiffness (Zikry 1994). The integration method is switched to the first-order accurate, unconditionally stable, backward Euler method,

$$\tau_{n+1}^{(\alpha)} = \tau_n^{(\alpha)} + hf(\tau_{n+1}^{(\alpha)}, t_{n+1}), \quad (4.17)$$

which is solved using quasi-Newton iteration.

References—Chapter 4

Abaqus Version 6.7 Documentation

Belytschko, T., W. K. Liu, et al. (2000). Nonlinear Finite Elements for Continua and Structures. Wiley, New York.

Flanagan, D. P. and T. Belytschko (1981). “A Uniform Strain Hexahedron and Quadrilateral with Orthogonal Hourglass Control.” International Journal for Numerical Methods in Engineering **17**(5): 679-706.

Zikry, M. A. (1994). “An Accurate and Stable Algorithm for High Strain Rate Finite Strain Plasticity.” Computers and Structures; **50**(3): 337–350.

Chapter 5: Microstructurally Induced Hourglass Modes

5.1 Introduction

The inelastic deformation of materials, which can occur due to mechanisms such as dislocation motion in metals or shear yielding in polymers, is generally incompressible. When the number of displacement degrees of freedom is less than the number of incompressibility pressure constraints, an element can numerically lock (Belytschko, Liu et al. 2000). For most elements, it is possible to reduce the number of incompressibility constraints by reducing the order of the Gauss quadrature. This can be accomplished by using selective integration or reduced integration. Selective integration, a generalization of the B-bar method (Hughes 1980), entails reduced Gauss integration of the volumetric terms and full Gauss integration of the deviatoric terms. Reduced integration has the advantage, however, of improving computational efficiency, which is critical in intensive finite-element analyses, such as finite strain inelastic analyses.

It is well known, though, that reduced one point integration leads to spurious zero energy modes, or hourglassing modes. Many methods have been developed to deal with this problem. Some examples include viscous and stiffness based perturbation stabilization normal to the linear velocity field (Flanagan and Belytschko 1981), viscous hourglass stabilization to resist components of the velocity field normal to the strain calculation (Goudreau and Hallquist 1982), and physical stabilization based on the Hu-Washizu variational principle (Belytschko and Bindeman 1991; Reese, Kussner et al. 1999; Reese 2005).

These cited methods have proven to be effective techniques in controlling hourglassing. The role of material instabilities, however, such as shear strain localization, which can arise due to the presence of microstructural characteristics, such as inclusions, dispersed particles, and grain boundaries (GBs), is not well understood. Specifically, can hourglassing occur due to microstructural characteristics of materials subjected to large inelastic strains? If these modes occur due to microstructural characteristics, then care must be taken to control these microstructurally induced numerical instabilities with the appropriate hourglass control techniques.

The major objective, therefore, of this investigation is to identify how material mechanisms at the microstructural scale can induce numerical instabilities, such as hourglassing. If these numerical instabilities are not accurately identified and controlled, they can preclude the modeling of the physical processes of microstructurally induced material instabilities and failure modes. In the present study, the dislocation density based crystalline plasticity framework and finite element methods outlined in Chapters 3 and 4 are used to account for large inelastic deformations. The identification of hourglassing is based on the hourglass perturbation stabilization algorithm proposed by Flanagan and Belytschko (1981), outlined in Chapter 4. Numerical examples are presented to demonstrate how deformation behavior and microstructural features, such as shear strain localization and the presence of dispersed particles embedded within an inelastic crystalline matrix, can induce hourglass modes.

5.2 Approach—Measure of Hourglass Modes

The constitutive relationship outlined in Chapter 3 and numerical methods outlined in Chapter 4 are employed to investigate the effects of deformation and microstructure on the hourglassing instability. Following the method of Flanagan and Belytschko (1981) outlined in Section 4.1, an hourglass strain quantity is chosen to measure the amount of hourglassing in each element. Simply integrating the generalized hourglass strain-rates (eq. 4.2) gives a dimensional quantity with the dimension of length. Therefore, the root of the element area was used to normalize the time integration of the element hourglass strain-rate as

$$\varepsilon_{hgx}^{n+1} = \varepsilon_{hgx}^n + \frac{\gamma^T \mathbf{v}_x dt}{\sqrt{A}} \text{ and } \varepsilon_{hgy}^{n+1} = \varepsilon_{hgy}^n + \frac{\gamma^T \mathbf{v}_y dt}{\sqrt{A}} . \quad (5.1)$$

The L2 norm of the hourglass strain is used to measure the hourglass instability. Note that an element with the deformation shown in Figure 5.1 results in an hourglass strain of approximately 10% in the x-direction.

5.3 Results

5.3.1 Microstructural Representation

A 20-grain, 20 μm x 20 μm aggregate was modeled for quasi-static, plane strain isothermal, tension and compression, with a displacement loading at the top surface and symmetry boundary conditions at the bottom and left surfaces. Aluminum aggregates with and without dispersed particles were investigated. The grains were generated by Voronoi tessellation, and the misorientation between the grains was random with an average misorientation of less than 15°. The matrix material was FCC aluminum with 12 potentially active $\{111\}\langle 110 \rangle$ slip systems.

For the simulations with dispersed particles, an incoherent dispersed particle representative of the manganese-based $\text{Al}_{20}\text{Cu}_2\text{Mn}_3$ dispersed particle in aluminum alloys was modeled. The crystal structure of the particle was taken to be orthorhombic Bbmm (Robinson 1952; Robinson 1954), with lattice parameters $a=2.42$ nm, $b=1.25$ nm, and $c=0.775$ nm. Six theoretical slip systems were taken as the six most packed planes and shortest directions.

The particles were dispersed as a single particle within each grain. The size distribution was based on a Gaussian distribution about an experimentally observed mean (Lee and Zikry 2011) of 300×600 nm with a volume fraction of approximately 1%. The long axis of the particle was aligned with the [010] particle direction (Wang, Chunzhi et al. 1989). The material properties of the matrix and dispersed particles are summarized in Table 5.1. A mesh of 9346 elements was used for both cases with and without dispersed particles to fully understand the effects of the dispersed particles on deformation and hourglass modes. To quantify the effects of microstructure and inelastic deformation modes on hourglassing, hourglass controls were not used.

5.3.2 Effect of Matrix Deformation

Figure 5.2 shows the contour plots of the hourglass strain measure (L2 norm of hourglass strain) and the effective plastic shear slip for the 20-grain matrix (no dispersed particles) model at 10% nominal compressive strain. A localized band of heavy plastic slip is formed at the bottom left of the model and extends to the top right free boundary. The maximum values of the L2 norm of the hourglass strain (Figure 5.2a, with an overall

maximum value of 0.312), occur in the vicinity of the maximum effective plastic shear slip (Fig 5.2b). This is not an element-to-element correspondence, however.

Figure 5.3 shows similar contour plots for the matrix aluminum aggregate at 10% nominal tensile strain. As in the compression case, the local plastic slip, though less intense, is localized in a band, and the maximum hourglass strain occurs in the vicinity of this band.

It must be noted, however, that the plastic deformation calculated based on eq. 3.3 is the sum of simple shears, which is only associated with the linear velocity field, eliminating plastic deformation as a direct cause of the hourglass instability.

5.3.3 Effects of Dispersed Particles

The hourglass strain measure and the effective plastic shear slip for the 20-grain model with dispersed particles at 10% nominal compressive and tensile strain are shown in Figs. 5.4-5.5. As in the matrix only case, hourglassing (as measured by the hourglass strain norm) occurs in the localized band near regions that have the maximum plastic strains.

The effects of the dispersed particles on the hourglassing instability can also be seen in Figs. 5.4-5.5. High values of hourglass strain measures occur near the dispersed particles, with no significant plastic strain near the dispersed particles. These results are consistent for both the compression and tension cases. From these results, it is clear that the presence of the dispersed particles results in the hourglass modes.

5.3.4 Influence of Microstructure and Deformation on Hourglass Modes

To further understand how the hourglass modes initiate and evolve, hourglass instability has to be investigated at the element level. Three major factors contribute to hourglass initiation and propagation, and they can be summarized as (i) deformable regions

can trigger hourglassing in more rigid neighboring regions; (ii) the constraint imposed by these rigid regions can trigger hourglass modes in the more deformable neighboring regions; and (iii) the ease of propagation of the hourglass modes determines the onset of the hourglassing instability.

The first factor applies to the effects of both local plastic slip and the presence of the dispersed particles on the hourglass instability. In the case of accumulated plastic slip in the matrix, the difference in deformability of two neighboring regions or elements is related to the amount of plastic deformation of the elements; the more deformable element is one that has more shear slip than its more rigid, less plastic neighbor. In the case of the particle-matrix interface, the difference in deformability of the two neighboring elements is a function of the material properties; the more deformable element is that of the matrix attached to the more rigid dispersed particle element.

The neighboring, more rigid elements must maintain displacement compatibility with the more deformable elements. The corresponding deformation in the more rigid elements can be either associated with the linear velocity field (strain energy) or hourglassing (zero energy). Because hourglassing motion can displace the two nodes of the more rigid neighboring element, which are connected to the more deformable element, with little displacement of the other two nodes of the more rigid element, compatibility can be maintained through hourglassing, which may involve less strain energy than linear deformation of the more rigid neighboring elements.

To substantiate these arguments, an intensely plastically deformed matrix element is circled in Figure 5.6a. This element acts as a trigger for hourglassing in the neighboring

elements. The more deformable matrix element with the highest value of plastic shear slip does not hourglass, but it can trigger an hourglass mode in the surrounding, less deformable elements. This can also be illustrated by highly sheared elements at a triple junction (circled in Figure 5.6b) triggering hourglass modes in neighboring regions. Hourglass modes can evolve within a rigid dispersed particle due to the surrounding matrix deformation, which is not highly plastic, but elastically more deformable than the particle elements (shown by arrow, Figure 5.6c). Also, hourglassing of the matrix elements can make the particle-matrix interface nodes more deformable, also triggering hourglassing in the element with the particle.

The particles' ability to trigger hourglassing in the matrix (factor (ii)) can be seen in Figure 5.7. The presence of the dispersed particle constrains the matrix elements attached to the particle due to the different material properties of the particle and the matrix. Since interface nodes of the matrix element are constrained by the presence of the particle, more deformable matrix elements at the interface can maintain compatible displacements with their surroundings by displacing the two nodes not attached to the particle in an hourglassing manner. The constrained natural (linear) deformation of the matrix element at the interface could lead to a higher energy state than that of hourglassing deformation. Therefore, this constraint can be a cause of the hourglass instability in the matrix.

The occurrence of hourglass modes is not only dependent on the energetically favorable deformation state of one element, but that of the whole model (factor (iii)). Hourglass deformation in an element is a zero energy mode, associated with nodal displacements representing deformation orthogonal to the natural linear velocity field.

However, for an hourglassing mode to occur in an element or region of elements, linear deformation, associated with strain energy, may be necessary in neighboring elements or regions. Therefore, the occurrence of hourglass modes depends on the competition between deformation associated with the linear velocity field of the elements, which contributes to strain energy, and deformation associated with hourglassing (orthogonal to the linear velocity field), which, due to the zero energy nature in hourglassing elements, can be energetically favorable.

Whether the particle hourglassing is due to the matrix deformation or the hard particle triggers the hourglass modes in the matrix can be explained by the ease of hourglass propagation within the particle in comparison with propagation within the matrix. Figure 5.8 shows the effects of three different particle mesh arrangements on the hourglass instability. From these plots, it is clear that the 2 x 3 element particle mesh arrangement can hourglass in the direction of the long axis of the particle with minimal disturbance of the matrix due to the particle mesh arrangement. In this case, the particle-matrix interface parallel with the long axis is minimally disturbed.

For the 1 x 4 particle mesh arrangement, there is more hourglassing within the particle in comparison with the 1 x 3 particle mesh arrangement. Hourglassing in a 1 x 4 element particle consists of end deformations that are symmetric. However, if a particle meshed with 1 x 3 arrangement were to hourglass, the displacements on opposite ends would be antisymmetric. This would most likely lead to a higher strain energy state in the matrix, explaining why the 1 x 4 element particle itself hourglassing and the 1 x 3 element particle only triggers the hourglass mode in the surrounding matrix. Particles containing an even

number of elements along one or both sides were more susceptible to the hourglass instability within the particles.

It must be noted that at the particle-matrix interface, the first occurrence of hourglassing is usually in the matrix itself. This instability can then propagate into the particle due to the increased deformability of the matrix at these interface nodes compared to the particle rigidity (factor (i)), where the deformability of the interface nodes, at the particle-matrix interface, is enhanced by the hourglassing in the matrix.

5.4 Conclusions

The effects of microstructure and deformation modes on hourglass instability were investigated by the implementation of a dislocation density based crystal plasticity finite element model and an hourglass strain measure orthogonal to the linear velocity field. The effects of microstructure and deformation on the initiation and evolution of hourglass modes were identified, and three major factors contributing to the tendency to hourglass were identified. First, the element interface between a more rigid and more deformable element can lead to hourglass modes in the more rigid regions. This occurs when heavily sheared matrix elements border matrix elements with less plasticity, and at particle-matrix interfaces where the difference in deformability is due to material properties. Secondly, the constraint of the more deformable regions due to the presence of the more rigid regions can lead to hourglassing. Finally, the determining factor in whether the hourglassing occurs in the more rigid or the more deformable region depends on the ease of propagation of the hourglass mode in the two neighboring regions, and in this case the mesh arrangement pertaining to the dispersed particle can have a critical effect.

References—Chapter 5

- Belytschko, T. and L. P. Bindeman (1991). “Assumed Strain Stabilization of the 4-Node Quadrilateral with 1-Point Quadrature for Nonlinear Problems.” Computer Methods in Applied Mechanics and Engineering **88**(3): 311-340.
- Belytschko, T., W. K. Liu, et al. (2000). Nonlinear Finite Elements for Continua and Structures. Wiley, New York.
- Flanagan, D. P. and T. Belytschko (1981). “A Uniform Strain Hexahedron and Quadrilateral with Orthogonal Hourglass Control.” International Journal for Numerical Methods in Engineering **17**(5): 679-706.
- Goudreau, G. L. and J. O. Hallquist (1982). “Recent Developments in Large-Scale Finite Element Lagrangian Hydrocode Technology.” Computer Methods in Applied Mechanics and Engineering **33**(1-3): 725-757.
- Hughes, T. J. R. (1980). “Generalization of Selective Integration Procedures to Anisotropic and Nonlinear Media.” International Journal for Numerical Methods in Engineering **15**(9): 1413-1418.
- Lee, W. M. and M. A. Zikry (2011). “Microstructural Characterization of a High-Strength Aluminum Alloy Subjected to High Strain-Rate Impact.” Metallurgical and Materials Transactions. A, Physical Metallurgy and Materials Science **42**(5): 1215-1221.
- Reese, S. (2005). “On a Physically Stabilized One Point Finite Element Formulation for Three-Dimensional Finite Elasto-Plasticity.” Computer Methods in Applied Mechanics and Engineering **194**(45-47): 4685-4715.
- Resse, S., M. Kussner, et al. (1999). “A New Stabilization Technique for Finite Elements in Non-Linear Elasticity.” International Journal for Numerical Methods in Engineering **44**(11): 1627-1652.
- Robinson, K. (1952). “The Unit Cell and Brillouin Zones of $\text{Ni}_4\text{Mn}_{11}\text{Al}_{60}$ and Related Compounds.” Philosophical Magazine 1952; **43**(342): 775-782.
- Robinson, K. (1954). “The Determination of the Crystal Structure of $\text{Ni}_4\text{Mn}_{11}\text{Al}_{60}$.” Acta Crystallographica; **7**(6-7): 494-497.
- Wang, S., L. Chunzhi, et al. (1989). “Determination of $\text{Al}_{20}\text{Cu}_2\text{Mn}_3$ Phase in Al-Cu-Mn Alloys.” Materials Research Bulletin **24**(10): 1267-1270.

Tables and Figures—Chapter 5

Table 5.1: Material properties of aluminum matrix and manganese-bearing dispersed particles

Property	Matrix Value	Particle Value
Elastic Modulus, E	70 GPa	110 GPa
Poisson's Ratio, ν	0.33	0.33
Static Yield Strength, τ_s^α	200 MPa	400 MPa
Rate Sensitivity, m	0.01	0.01
Reference Strain-rate, $\dot{\gamma}_{ref}$	0.001 s^{-1}	0.001 s^{-1}
Burgers Vector, \bar{b}	$0.289 \times \{111\}\langle 110 \rangle \text{ nm}$	$0.270 \times (010)[001] \text{ nm}$ $0.438 \times (-101)[101] \text{ nm}$ $0.438 \times (101)[10-1] \text{ nm}$ $0.438 \times (010)[101] \text{ nm}$ $0.438 \times (010)[10-1] \text{ nm}$ $0.432 \times (001)[010] \text{ nm}$
Initial ρ_m	10^{11} m^{-2}	10^7 m^{-2}
Initial ρ_{im}	10^{13} m^{-2}	10^9 m^{-2}
Saturation ρ_{sat}	10^{14} m^{-2}	10^{14} m^{-2}

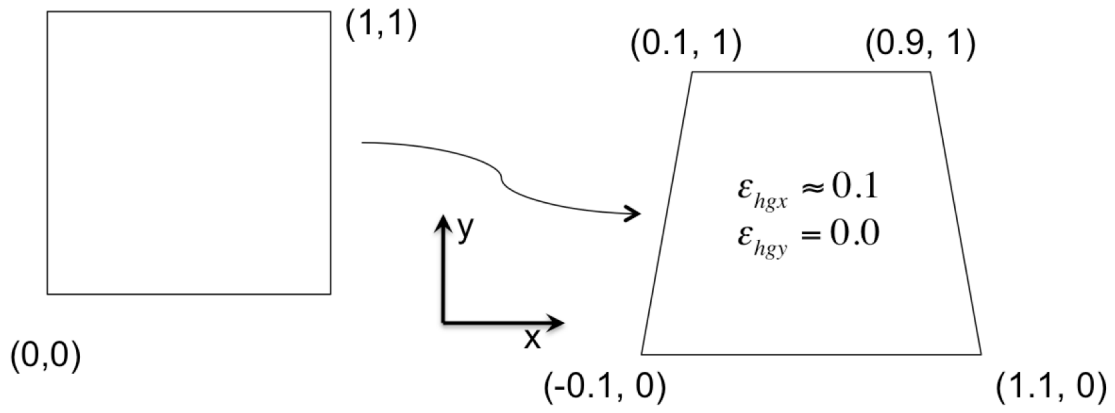


Figure 5.1: Hourglassing deformation associated with a 10% hourglass strain in the x-direction

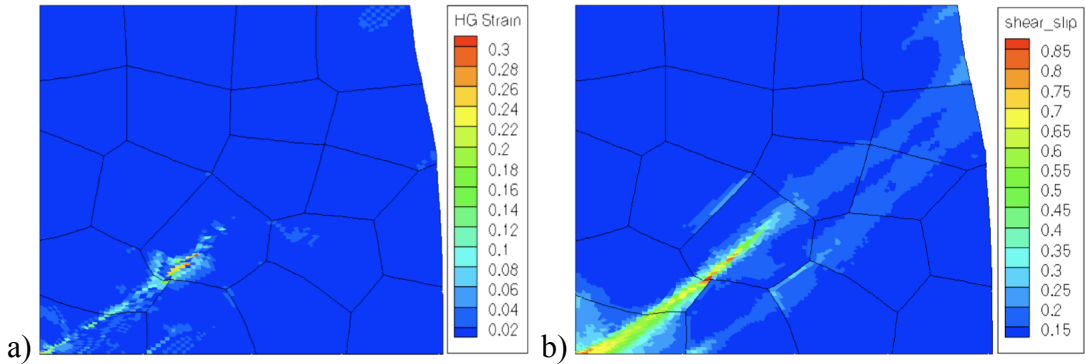
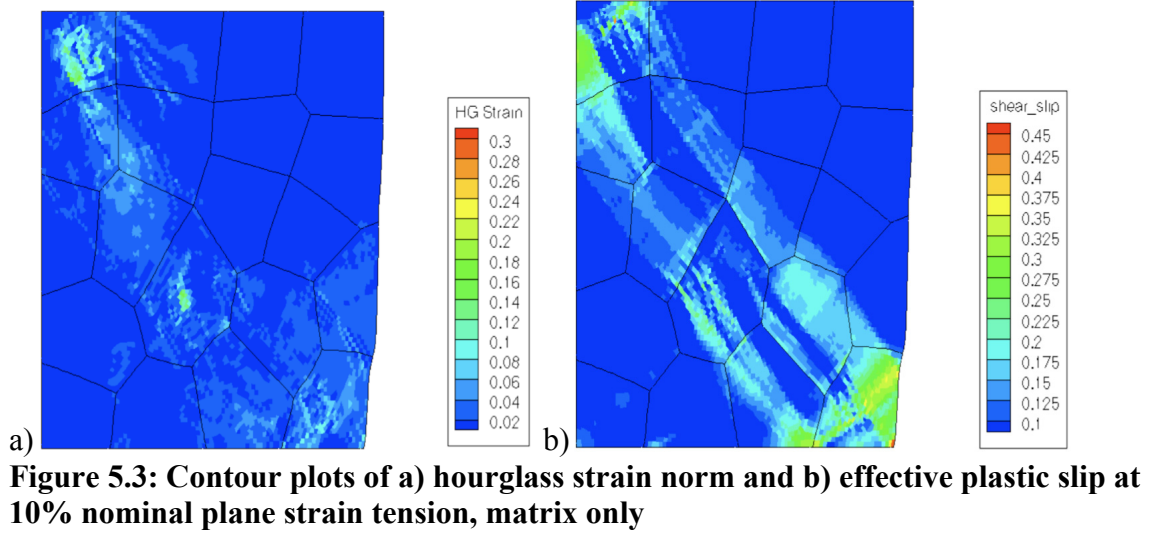


Figure 5.2: Contour plots of a) hourglass strain norm and b) effective plastic slip at 10% nominal plane strain compression, matrix only



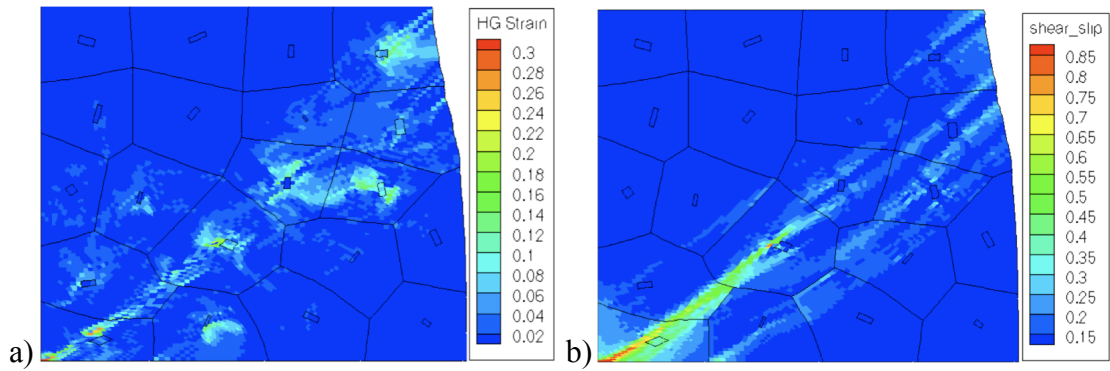


Figure 5.4: Contour plots of a) hourglass strain norm and b) effective plastic slip at 10% nominal plane strain compression, dispersed particles included

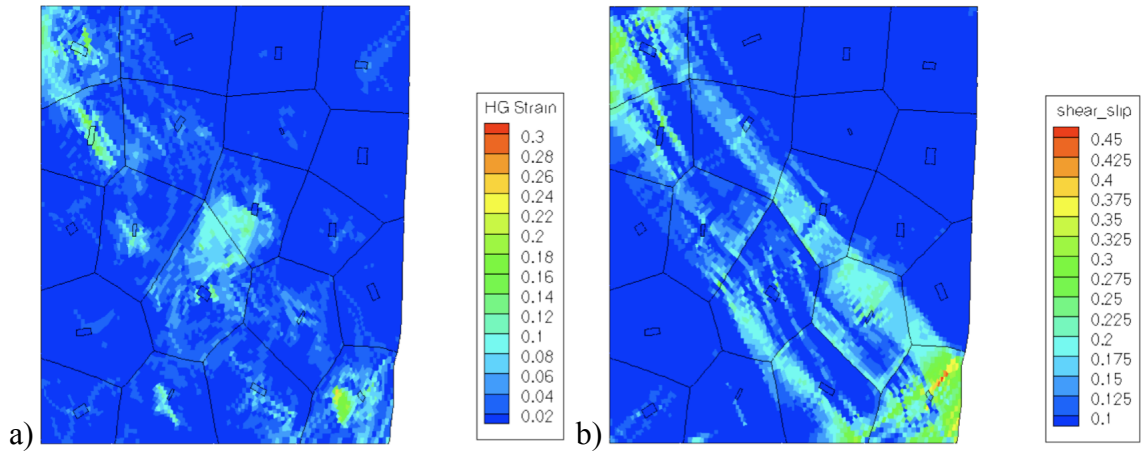


Figure 5.5: Contour plots of a) hourglass strain norm and b) effective plastic slip at 10% nominal plane strain tension, dispersed particles included

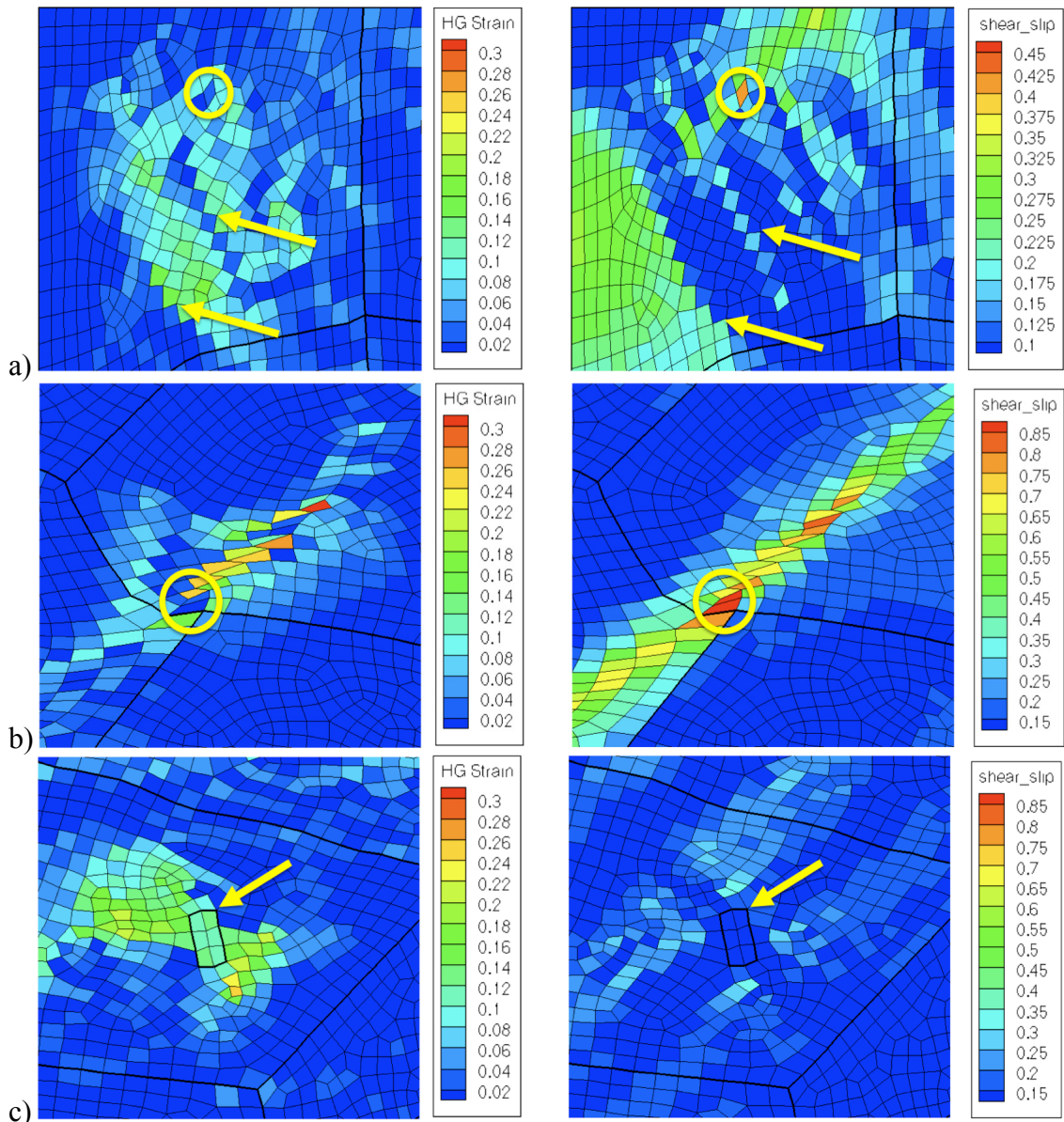


Figure 5.6: Contour plots of hourglass strain norm and effective plastic slip, factor (i). a) Localized shear slip in matrix element triggering hourglass modes in surrounding regions; b) localized shear in matrix elements at triple junction triggering hourglass modes in neighboring elements; c) deformable matrix elements triggering hourglass modes in a dispersed particle

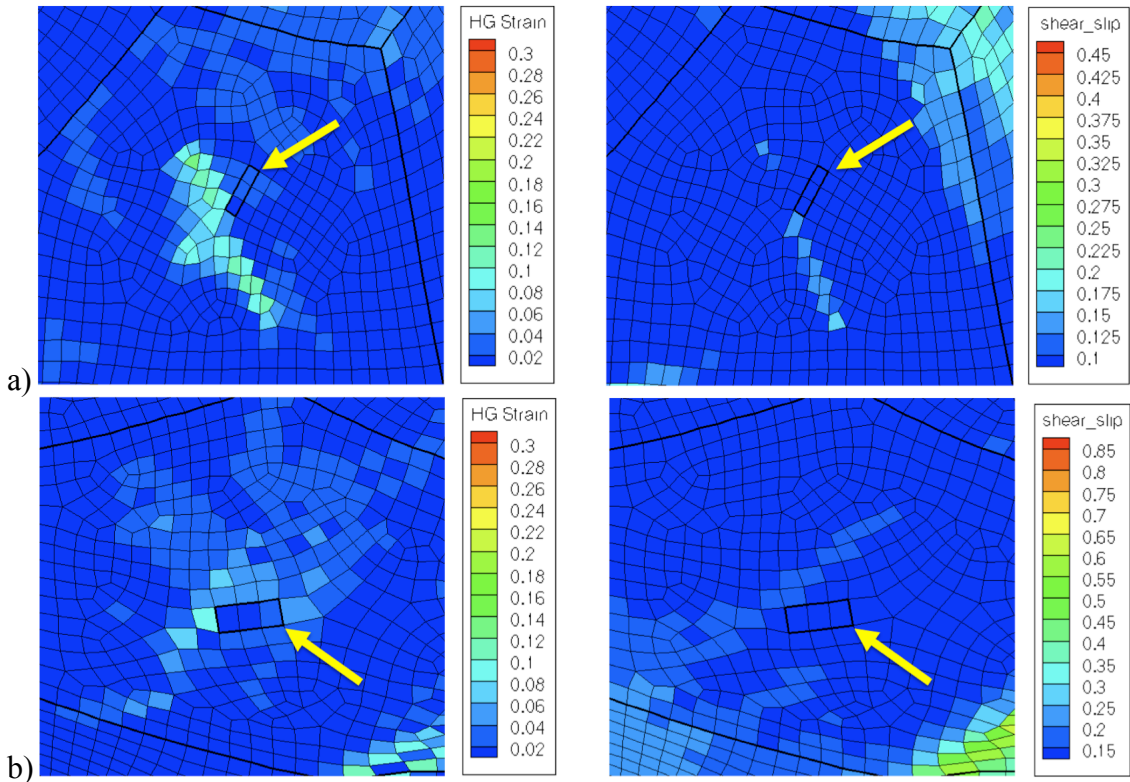


Figure 5.7: Contour plots of hourglass strain norm and effective plastic slip, factor (ii): hourglassing in matrix caused by constraint associated with single element thick dispersed particles at a) 10% nominal tension and at b) 10% nominal compression; arrows indicate dispersed particles

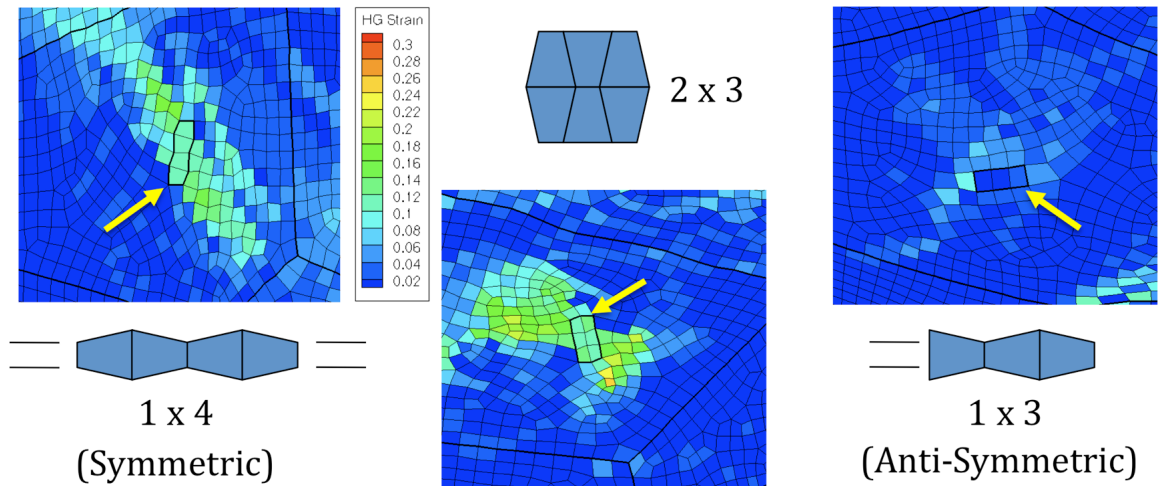


Figure 5.8: Effect of particle meshing on propagation of the hourglass instability; arrows indicate dispersed particles

Chapter 6: Orowan Looping and Plastic Relaxation in Crystalline Plasticity Finite Element Analysis

6.1 Introduction

It is evident from the characterization results in Chapter 2 that the dispersed particles are critical in the final failure behavior of the high strength Al 2139 alloy. Therefore, it is of great interest to develop a predictive analysis capability to model the effects of these particles on the deformation and damage behavior of the alloy that can be used to optimize the microstructure by simulation techniques such as the finite element method.

The interaction between dislocations and particles dispersed in a metallic matrix clearly affects the behavior of high strength alloys. These interfacial interactions are directly related to the yield strength (Nie, Muddle et. al. 1996), post-yield hardening and subsequent softening (Brown and Stobbs 1971a-b, 1976; Atkinson, Brown et al. 1974), and failure (Yeh and Liu, 1996; Mawsouf, 2000; Kwon, 1988; Kwon, Lee et. al. 1992; Goods and Brown 1978; Argon, Im et. al. 1975). Post-yield behavior is directly related to these accumulated Orowan loops, which are unrelaxed plastic strains as noted by (Brown and Stobbs, 1971a-b, 1976; Atkinson, Brown et al. 1974). The accumulation of these Orowan loops leads to hardening and accumulation of stresses in the particle and interfacial regions, which subsequently results in either matrix plastic relaxation to relieve these stress accumulations, or failure when the matrix is unable to relax these strain incompatibilities (Brown and Stobbs 1971a). For particles larger than approximately 100 nm, as is the case with the $\text{Al}_{20}\text{Cu}_2\text{Mn}_3$ particles, this relaxation has been observed to occur by lattice rotations (Humphreys 1979).

The experimental observation of these Orowan loops and how they *evolve* is difficult, if not impossible, due to the ability of the loops to anneal out of TEM samples (Humphreys and Stewart 1975). Therefore, models that can accurately predict the effects of the dislocation interactions are essential to understanding how these interactions affect the deformation evolution when the material is subjected to extreme loading conditions. Atomistic modeling of the interaction of particles and metallic matrices has been conducted at approximate scales of 3 to 4 nm precipitates, see for example, Bacon and Osetsky (2005, 2007), Shim, Kim et al. (2008), and Kohler, Kizler et al. (2005), who have modeled coherent, irradiation-induced BCC-Cu precipitates in a BCC-Fe matrix. In these investigations, the interaction of a single dislocation and particle has been modeled. Hatano (2006) also used atomistic simulations to investigate Orowan-type and Hirsch-type (related to cross-slip) looping of an edge dislocation in copper about a rigid precipitate for different boundary conditions. However, these atomistic simulations are severely limited by length and temporal scales. The length scales are generally on the order of nanometers and the time scales are on the order of picoseconds. Dislocation dynamics has also been utilized for simulations limited to single particles and small strain simulations (Queyreau and Devincere 2009; Takahashi 2008).

Dislocation density based crystalline plasticity models (see, for example, Bate 1999; Elkhodary, Lee et al. 2011) can be used to surmount these scale issues, allowing a detailed microstructural investigation of the collective effects of dispersed particles, grain sizes, particle distribution and morphology, and volume fraction at physically realistic strain-rates and lengths.

However, the crystal plasticity finite-element based computations outlined in Chapters 3 and 4 have limitations associated with modeling interfacial behavior, such as Orowan looping and the relaxation of plastic strain incompatibilities. The computation of dislocation densities is based on obtaining plastic deformation at the element level. Matrix elements adjacent to the particle interface will be less likely to deform if the elements are associated with the region of the particle-matrix interface that intersects the slip plane, due to the presence of the more rigid particle. The dislocation densities computed at these matrix elements will be lower than those of the surrounding matrix. This is not consistent with the physics of Orowan looping, where the hardening associated with the particles is due to the loops formed in the matrix around the particle at interfacial regions that intersect the active slip planes, which is the mechanism that leads to plastic slip incompatibilities.

To address this and to represent the appropriate physics associated with looping and unrelaxed strains, we have used the concept of eigenstrains in our dislocation density based crystalline plasticity formulation. The concept of eigenstrains in the particle-matrix problem dates back to the work of Eshelby (1957). These eigenstrains, as noted by Mura (1987), are inelastic strains, and the incompatibilities of these eigenstrains can lead to eigenstress fields. Brown and Stobbs (1971a) and Mura (1987) used eigenstrains to relate Orowan looping to phenomenological models by representing the unrelaxed plastic strains in a single particle as eigenstrains.

The major objective, therefore, is to develop a formulation to account for the unrelaxed plastic strains associated with Orowan looping using the eigenstrain philosophy, which can be coupled with the dislocation density based crystalline plasticity formulation

developed in Chapters 3 and 4 to investigate the effects of dispersed particles at physically realistic length and temporal scales. Lattice rotation incompatibilities between the particle and the matrix will be used to model plastic relaxation. The eigenstrain representation of Orowan looping and plastic relaxation is summarized in this chapter.

6.2 Approach

6.2.1 Orowan Looping

The calculation of the interfacial unrelaxed plastic strain is based on an eigenstrain formulation. The velocity gradient in the particle elements (elastic particles), coupled to the dislocation density based finite element formulation, can be additively decomposed as

$$L_{kl} = L_{kl}^e + L_{kl}^*, \quad (6.1)$$

where L_{kl}^* is the eigenvelocity gradient.

The eigenvelocity gradient in each particle due to the plastic deformation of the surrounding matrix is taken as the negative of the volume average of the plastic velocity gradient of the surrounding matrix grain (see, for example, Mura 1987).

$$L_{kl}^* = -\frac{1}{V_{matrix}} \int L_{matrix}^p dV. \quad (6.2)$$

The stress update is

$$\sigma_{ij}^{\Delta,e} = C_{ijkl} (D_{kl} - D_{kl}^*). \quad (6.3)$$

6.2.2 Verification of Eigenstrain Representation

The eigenstrain method was verified using the Eshelby analytical solution. A quasi-static plane strain finite element analysis was used to compare the eigenstrain formulation to

the analytical results of Eshelby (1957). The 10 μm x 10 μm model consisted of an elastic matrix and an elastic 1 μm diameter circular particle. The outer boundary was fully constrained. The results from the plane strain finite element analysis were compared with the analytical solution of Eshelby for the elliptic cylinder case where $a_1=a_2 \ll a_3$, where the a values are the respective half-axis lengths of the ellipsoidal inclusion, and the 3-direction is pointing out of the page (Mura 1987).

An eigenvelocity gradient was applied in the particle to represent the deformation associated with Figure 6.1. This follows the method of Brown and Stobbs (1971a), by assigning the negative of the plastic shear slip as the transformation strain (eigenstrain) in the particle. The simulations were continued to represent a matrix plastically strained to 10%.

First, the homogeneous inclusion problem, where the particle and the matrix share identical elastic constants, was investigated. The well-known solution to the stress in the inclusion for this Eshelby problem, $\sigma_{ij} = C_{ijkl} (S_{klmn} \varepsilon_{mn}^P)$, in this situation becomes

$$\sigma_{12} = -\frac{2\mu}{1-\nu} \frac{a_1 a_2}{(a_1 + a_2)^2} \varepsilon_{12}^P, \quad (6.4)$$

where the values μ and ν are elastic constants, a_i $i = 1, 2, 3$ are the half axis lengths, and

$\varepsilon_{12}^P = -\frac{\gamma^P}{2}$. Table 6.1 contains the values for the parameters used in this investigation. Figure

6.2 compares the values of the stress in the particles from the simulations with the values from the Eshelby solution. The finite element values are adjusted to account for the image stress that is present due to the fixed boundaries by subtracting this mean stress from the finite element values. The maximum error computed was 0.52%.

The inhomogeneous inclusion case was also investigated. For this case, where the elastic constants of the particle and matrix differ, $\sigma_{ij} = C_{ijkl}^* (S_{klmn} \varepsilon_{mn}^{**} - \varepsilon_{kl}^P)$ is used, where $\varepsilon_{ij}^{**} = \varepsilon_{ij}^* + \varepsilon_{ij}^P$ and C_{ijkl}^* is a tensor containing the elastic constants of the particle. For the infinite rod, the pertinent components of the Eshelby tensor become

$$S_{1212} = S_{1221} = S_{2121} = S_{2112} = \frac{1}{2(1-\nu)} \left(\frac{a_1^2 + a_2^2}{2(a_1 + a_2)^2} + \frac{1-2\nu}{2} \right) = 0.31343. \quad (6.5)$$

The total eigenstrain (using the terminology of Mura (1987)), ε_{12}^{**} , with no externally applied strain, then becomes

$$\varepsilon_{12}^{**} = \frac{2\mu^* \varepsilon_{12}^P}{4(\mu^* - \mu)S_{1212} + 2\mu} = 1.229\varepsilon_{12}^P \quad (6.6)$$

Therefore, the stress can be found using the following:

$$\sigma_{12} = C_{1212}^* (S_{1212} \varepsilon_{12}^{**} + S_{1221} \varepsilon_{21}^{**} - \varepsilon_{12}^P) + C_{1221}^* (S_{2121} \varepsilon_{21}^{**} + S_{2112} \varepsilon_{12}^{**} - \varepsilon_{21}^P) \quad (6.7)$$

Due to symmetry of the strain tensor, this becomes

$$\sigma_{12} = 2\mu^* (.77041 - 1) \varepsilon_{12}^P \quad (6.8)$$

Table 6.2 summarizes the parameters used for the inhomogeneous inclusion case, and Figure 6.3 compares the finite element results with the analytical calculations. The maximum calculated error was 1.13%.

6.2.3 Representation of Plastic Relaxation

For particles larger than approximately 100 nm, as is the case with the $\text{Al}_{20}\text{Cu}_2\text{Mn}_3$ dispersed particle (Lee and Zikry 2011), relaxation of this eigenstrain in the particle will occur due to dislocation generation at the interface (Humphreys 1979). The effect of this

dislocation generation can be captured by relating the lattice rotations of the particles to that of the surrounding matrix grains. Figure 6.4, adapted from Humphreys and Kalu (1990), summarizes the looping and relaxation sequence with reference to the current configuration. Prior to plastic relaxation, there is no incompatibility between the lattice rotations of the particle and the surrounding matrix. However, once relaxation occurs, the particle lattice rotates with respect to the matrix lattice (Figure 6.4).

For the general problem, the eigenvelocity gradient, L_{ij}^* is determined from the plastic velocity gradient of the surrounding matrix grain L_{ij}^p using eq. 6.2 (also shown in Fig. 6.4), and relaxed based on the mismatch in the lattice rotations of the particles and the surrounding matrix grain. When the eigenstrain in the grain in which the particle is located attains a threshold value of 0.1%, which is approximately the eigenstrain that would generate a single Orowan loop for the particles on the length scale of interest (see, for example, Brown and Stobbs 1971a, eq. 1), the relaxation rate of the eigenstrain is determined by eq. 6.9 as

$$\dot{\theta}_{relax} = sign(\overline{W}_{21matrix}^p)(\dot{\theta}_{particle} - \dot{\theta}_{matrix}), \quad (6.9)$$

where the particle and matrix lattice rotations are averaged as

$$\dot{\theta}_{particle} = \frac{1}{V_{particle}} \int_{V_{particle}} W_{21particle}^e dV, \dot{\theta}_{matrix} = \frac{1}{V_{matrix}} \int_{V_{matrix}} W_{21matrix}^e dV, \overline{W}_{21matrix}^p = \frac{1}{V_{matrix}} \int_{V_{matrix}} W_{21matrix}^p dV. \quad (6.10)$$

Note that the lattice rotation of the particle is not affected by the eigenspin rate

($W_{kl}^* = asym(L_{kl}^*)$), since this rotation is from the stress-free state and not the previous state of deformation. The sign function is used, since a matrix plastic deformation with a positive

multiple slip deformation rate shear component relaxes in different directions depending on the sign of the plastic spin rate in the matrix. Eq. 6.9 ensures that the relaxation rate of the eigenstrain is calculated as positive when the rotations lead to relaxation. These rotations are volume averages associated with the previous timestep.

This relaxation is associated with the shear part of the eigenstrain. Therefore, implementation requires rotating the eigenstrain rate tensor to the maximum shear strain-rate configuration to obtain $D_{\max\ shear}^*$. The maximum shear eigenstrain rate is

$$D_{12,\max\ shear}^* = \sqrt{\frac{1}{4}(D_{11}^* - D_{22}^*)^2 + D_{12}^{*2}}, \quad (6.11)$$

and the rotation of the eigenstrain rate tensor to obtain this state of strain is

$$\tan 2\theta_p = \frac{2D_{12}^*}{D_{11}^* - D_{22}^*}, \quad (6.12)$$

$$\theta_s = -(45^\circ - \theta_p), \quad (6.13)$$

$$R = \begin{bmatrix} \cos \theta_s & -\sin \theta_s \\ \sin \theta_s & \cos \theta_s \end{bmatrix}, \quad (6.14)$$

$$D_{\max\ shear}^* = R^T D^* R, \quad (6.15)$$

where this maximum shear rate is always taken as positive to correspond with the positive angular rate of relaxation (eq. 6.9). Once the maximum shear eigenstrain rate is obtained, the relaxed eigenstrain rate tensor is

$$D_{\max\ shear_relaxed}^* = D_{\max\ shear}^* - \begin{bmatrix} 0 & 1 \\ 1 & 0 \end{bmatrix} \frac{\dot{\theta}_{relax}}{2}. \quad (6.16)$$

The eigenstrain is defined as the time integral of the shear component of the relaxed shear eigenstrain rate ($D_{12, \max \text{ shear } _relaxed}^*$). The relaxed eigenstrain rate tensor is rotated back into the global reference frame as

$$D_{relaxed}^* = R D_{\max \text{ shear } _relaxed}^* R^T \quad (6.17)$$

The antisymmetric part of the eigenvelocity gradient must also be updated due to relaxation and is

$$W_{21relaxed}^* = W_{21}^* - \text{sign}(W_{21}^*) \frac{\dot{\theta}_{relax}}{2}. \quad (6.18)$$

This relaxation is calculated only when the term $\dot{\theta}_{relax}$ is positive, accounting for the possibility of dislocation activity at the interface that does not relax the eigenstrain associated with Orowan looping.

References—Chapter 6

- Argon, A. S., J. Im, et al. (1975). “Cavity Formation From Inclusions in Ductile Fracture.” Metallurgical Transactions A **6**(4): 825-837.
- Atkinson, J. D., L. M. Brown, et al. (1974). “The Work-hardening of Copper-Silica IV. The Bauschinger Effect and Plastic Relaxation.” Philosophical Magazine **30**(6): 1247-1280.
- Bacon, D. J. and Y. N. Osetsky (2005). “Modeling Dislocation-Obstacle Interactions in Metals Exposed to an Irradiation Environment.” Materials Science and Engineering A **400**: 353-361.
- Bacon, D. J. and Y. N. Osetsky (2007). “The Atomic-Scale Modeling of Dislocation-Obstacle Interactions in Irradiated Metals.” Journal of Materials **59**(4): 40-44.
- Bate, P., (1999). “Modeling Deformation Microstructure with the Crystal Plasticity Finite-Element Method.” Philosophical Transactions of the Royal Society of London A **357**(1756): 1589-1601.
- Brown, L. M. and W. M. Stobbs (1971a). “The Work-Hardening of Copper-Silica I. A Model Based on Internal Stresses, With No Plastic Relaxation.” Philosophical Magazine, **23**(185): 1185-1199.
- Brown, L. M. and W. M. Stobbs (1971b). “The Work-Hardening of Copper-Silica II. The Role of Plastic Relaxation.” Philosophical Magazine **23**(185): 1201-1233.
- Brown, L. M. and W. M. Stobbs (1976). “The Work-Hardening of Copper-Silica V. Equilibrium Plastic Relaxation by Secondary Dislocations.” Philosophical Magazine **34**(3): 351-372.
- Elkhodary, K. I., Lee, W. M., et al. (2011). “Deformation Mechanisms of an Ω Precipitate in a High Strength Aluminum Alloy Subjected to High Strain Rates,” Journal of Materials Research **26**(4): 487-497.
- Eshelby, J. D. (1957). “The Determination of the Elastic Field of an Ellipsoidal Inclusion, and Related Problems.” Proceedings of the Royal Society of London A **241**(1226): 376-396.
- Goods, S. H. and L. M. Brown (1978). “The Nucleation of Cavities By Plastic Deformation.” Acta Metallurgica **27**(1): 1-15.

- Hatano, T. (2008). "Dynamics of a Dislocation Bypassing an Impenetrable Precipitate: The Hirsch Mechanism Revisited." Physics Review B **74**(2): 1-4.
- Humphreys, F. J. (1979). "Local Lattice Rotations at Second Phase Particles in Deformed Metals." Acta Metallurgica **27**(12): 1801-1814.
- Humphreys, F. J. and A. T. Stewart (1972). "Dislocation Generation at SiO₂ Particles in an α -Brass Matrix on Plastic Deformation." Surface Science **31**(1): 389-421.
- Humphreys, F. J. and P. N. Kalu (1990). "The Plasticity of Particle-Containing Polycrystals," Acta Metallurgica et Materialia **38**(6): 917-930.
- Kohler, C., P. Kizler, et al. (2005). "Atomistic Simulation of Precipitation Hardening in Alpha-Iron: Influence of Precipitate Shape and Chemical Composition." Modeling and Simulation in Materials Science and Engineering **13**(1): 35-45.
- Kwon, D., (1988). "Interfacial Decohesion Around Spheroidal Carbide Particles." Scripta Metallurgica **22**(7): 1161-1164.
- Kwon, D., S. Lee, et al. (1992). "Prediction of Matrix-Particle Interfacial Separation in Particle-Strengthened Materials." Materials Science and Engineering A **159**(2): 151-157.
- Lee, W. M. and M. A. Zikry (2011). "Microstructural Characterization of a High-Strength Aluminum Alloy Subjected to High Strain-Rate Impact." Metallurgical and Materials Transactions. A, Physical Metallurgy and Materials Science **42**(5): 1215-1221.
- Mawsouf, N. M. (2000). "A Micromechanical Mechanism of Fracture Initiation in Discontinuously Reinforced Metal-Matrix Composite." Materials Characterization **44**(3): 321-327.
- Mura, T. (1987). Micromechanics of Defects in Solids (2nd ed.). The Netherlands, Martinus Nijhoff.
- Nie, J. F., B. C. Muddle, et al. (1996). "The Effect of Precipitate Shape and Orientation on Dispersion Strengthening in High Strength Aluminium Alloys." Materials Science Forum **217**: 1257-1262.
- Queyreau, S. and B. Devincre (2009). "Bauschinger Effect in Precipitation-Strengthened Materials: A Dislocation Dynamics Investigation." Philosophical Magazine Letters **89**(7): 419-430.

Shim, J.-H., D.-I. Kim, et al. (2008). "Atomistic Study of Temperature Dependence of Interaction Between Screw Dislocation and Nanosized BCC Cu Precipitate in BCC Fe." Journal of Applied Physics **104**(8), 083523.

Takahashi, A. (2008). "Parameteric Dislocation Dynamics and Boundary Element Modeling of Elastic Interaction Between Dislocations and Precipitates." NATO Science for Peace and Security Series B - Physics and Biophysics 263-274.

Yeh, J.-W. and W.-P. Liu (1996). "The Cracking Mechanism of Silicon Particles in an A357 Aluminum Alloy." Metallurgical and Materials Transactions A **27**(11): 3558-3568.

Tables and Figures—Chapter 6

Table 6.1: Parameters used for homogeneous inclusion investigation

	Matrix	Particle
Shear Modulus, GPa	26.3	26.3
Poisson's Ratio	0.33	0.33
a_1 μm		0.5
a_2 μm		0.5
a_3 μm		∞

Table 6.2: Parameters used for inhomogeneous inclusion investigation

	Matrix	Particle
Shear Modulus, GPa	26.3	52.6
Poisson's Ratio	0.33	0.33
a_1 μm		0.5
a_2 μm		0.5
a_3 μm		∞

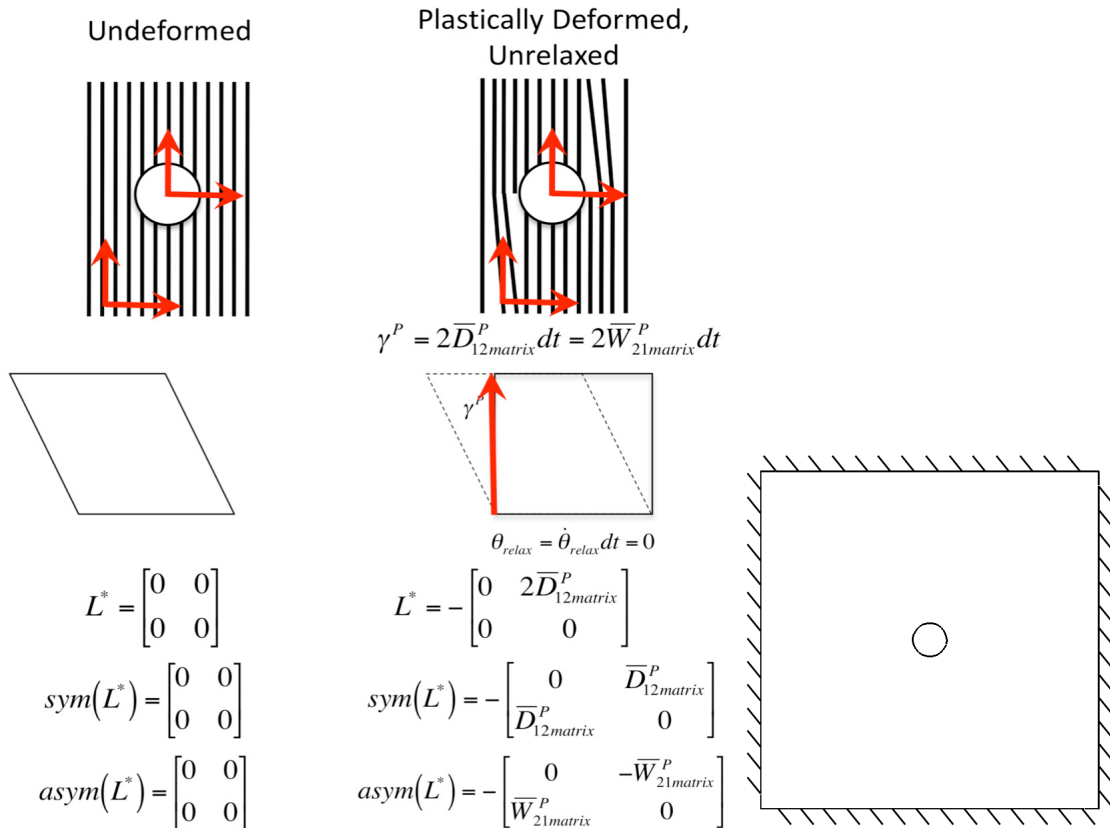


Figure 6.1: Schematic and model of Eshelby verification problem

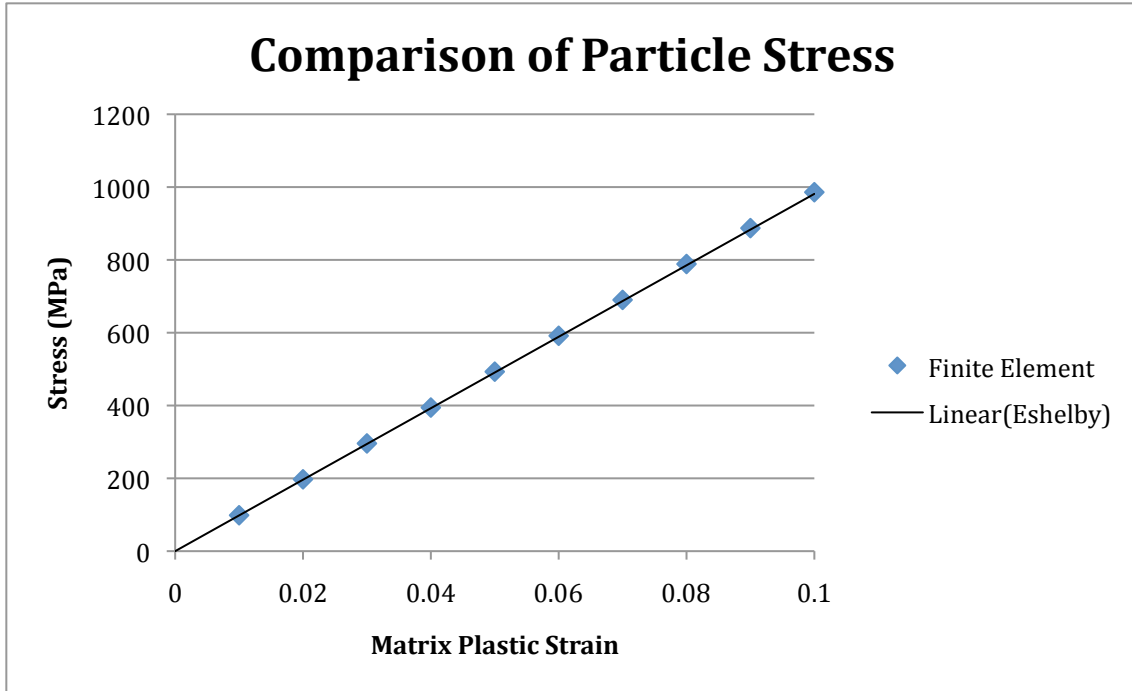


Figure 6.2: Comparison of the particle stress using the eigenstrain-based finite element method and the Eshelby solution for the homogeneous inclusion problem; maximum error=0.52%

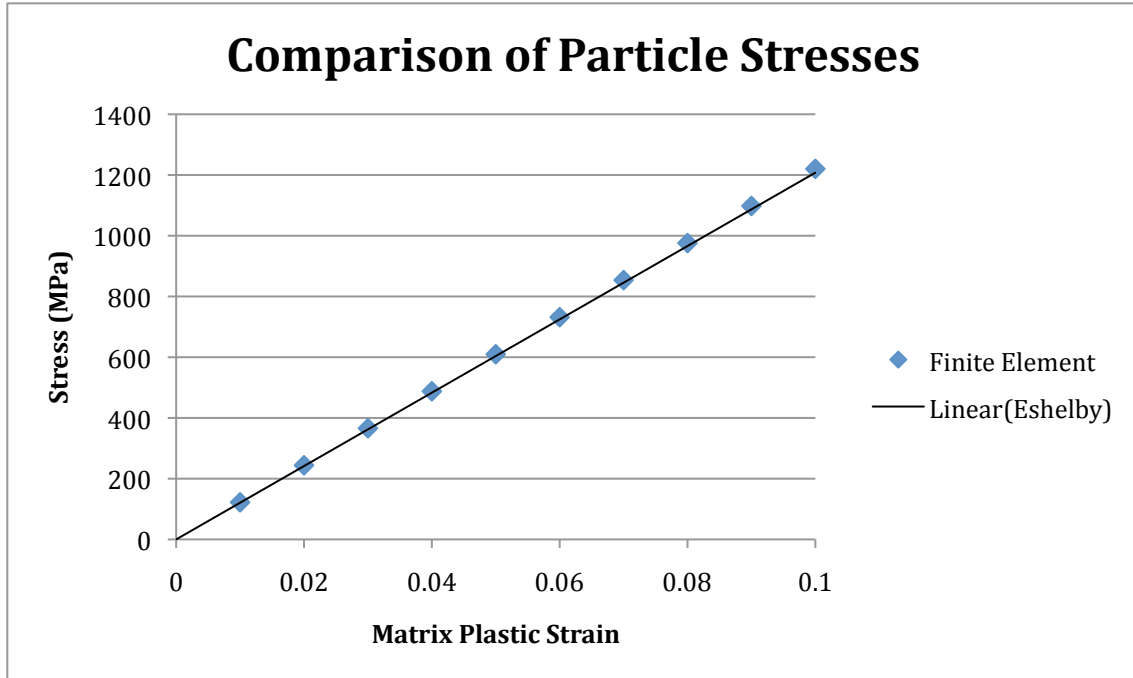


Figure 6.3: Comparison of the particle stress using the eigenstrain-based finite element method and the Eshelby solution for the inhomogeneous inclusion problem; maximum error=1.13%

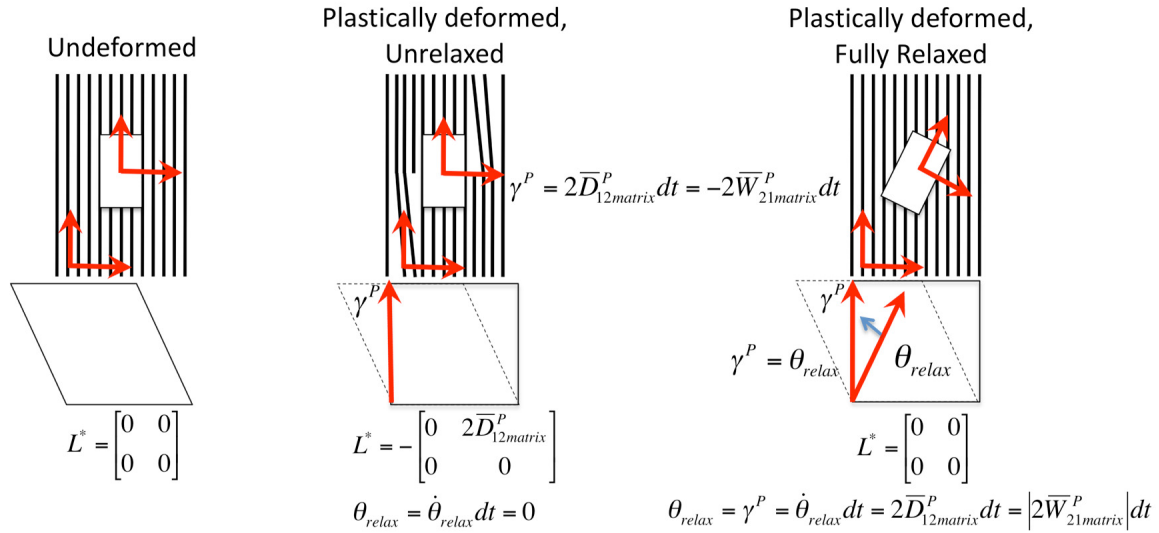


Figure 6.4: Schematic of looping and relaxation in pure shear with respect to the current configuration with different eigenvelocity gradients and lattice rotation calculations related to (b) unrelaxed and (c) fully relaxed plastic strains. Note the presence and deficit of an extra half-plane of atoms associated with Orowan looping in (b)

Chapter 7: Quasi-static Modeling of the Interfacial Plastic Strain Incompatibilities Associated with Dispersed Particles in High Strength Aluminum Alloys

7.1 Introduction

The major objective of this investigation is to use the dislocation density based crystal plasticity formulation and specialized microstructurally based finite element models outlined in Chapters 3 and 4 in conjunction with the eigenstrain representation of Orowan looping and unrelaxed strains outlined in Chapter 6 to investigate the unrelaxed plastic strain and its evolution and subsequent relaxation as a function of particle morphology, distribution, and orientation when subjected to quasi-static deformation. This behavior at each dispersed particle interface will then be collectively used to understand and predict failure modes, such as shear localization, in particle-reinforced high strength aluminum alloys.

7.2 Results

7.2.1 Microstructural Representation

Three quasi-static, plane strain isothermal finite element investigations were conducted, with stiffness based hourglass control used as outlined in Section 4.1. The first model (Model 1) is a single elastic particle with a vertically aligned (1-11) active slip plane subjected to displacement based vertical shear. The matrix lattice was aligned for preferential slip along the vertically aligned (1-11) slip plane using Euler angles (based on the Bunge definition) of $\varphi_1 = -45^\circ$, $\Phi = 35.3^\circ$, and $\varphi_2 = 0.0^\circ$. The model size is 4 μm by 4 μm with the left side fixed and the right side vertically displaced and horizontally constrained

for simple shear. Particle sizes of 200 nm by 400 nm and 400 nm by 800 nm with various orientations with respect to the most active (1-11) slip plane were investigated. A convergent mesh of approximately 1000 elements was employed, with a minimum of three elements along each side of the particle.

The second model (Model 2) that was investigated was the compressive plane strain deformation of a 20 μm by 20 μm single grain with 22 dispersed particles of random sizes and aspect ratios generated using a Gaussian distribution about the experimentally observed mean of 300 by 600 nm and a volume fraction of approximately 1% (Lee and Zikry 2011). The matrix lattice was aligned for preferential slip along the (1-11) plane as indicated by Figure 1 with Euler angles of $\varphi_1 = -45^\circ$, $\Phi = -19.7^\circ$, and $\varphi_2 = 0.0^\circ$. Symmetry boundary conditions were used and two dispersed particle configurations were investigated: (i) the long axis of all particles parallel to the most active slip plane of (1-11) and (ii) the long axis of all particles normal to the most active (1-11) slip plane. The aspect ratio is defined as the length of the particle parallel to the most active (1-11) slip plane divided by the length normal to the (1-11) slip plane (Figure 7.1b). A mesh of approximately 18,500 elements was employed, with a minimum of three elements along each particle side.

The third model (Model 3) is 20-grain, 20 μm by 20 μm aggregate with randomly oriented and sized particles. The grains were randomly oriented with an average misorientation of less than 15° for a low angle misorientation distribution. Plane strain compression was investigated with symmetry boundary conditions. A mesh of 16,158 elements was employed, with a minimum of three elements along each particle side. Figure

7.1 summarizes the three models, and the properties of the particles and matrix grains are summarized in Table 7.1.

7.2.2 Single Particle: Model 1

Figure 7.2 shows the contours of the von Mises stress and the pressure for the single 400 nm x 800 nm particle aligned with the long axis normal to the vertically aligned most active slip plane at a nominal shear strain of 5%. Contours are presented in Figure 7.2 for models without the eigenstrain formulation, with the eigenstrain formulation and no relaxation, and with the eigenstrain formulation and relaxation.

From these figures, the following can be noted: there are increases and decreases in the von Mises stresses due to the elastic particle when the eigenstrain formulation used. The increases and decreases local to the particle are consistent with the calculations of Brown and Stobbs (1971). The increases in the von Mises stresses occur in the areas of the particles that would have the extra half-planes associated with Orowan looping, and can result in shear failure modes. The decreases in the von Mises stresses are coincident with the most active (1-11) slip plane, and also extend beyond the particle to have a far-field effect, which is consistent with the backstresses (Atkinson, Brown et al. 1974), which would reduce the slip on the active slip plane. It can also be seen that there are increases in tensile pressures at the particle at the corners that would be associated with the deficit of a half-plane in Orowan looping. This increase in tensile pressures would result in particle-matrix decohesion due to the tensile pressure accumulation. The relaxation of the eigenstrain leads to stresses that are between the extremes of no eigenstrain and no relaxation.

In Figure 7.3, the amount of eigenstrain due to Orowan looping that was relaxed

$(\int D_{12,\max\ shear}^* dt - \int D_{12,\max\ shear_relaxed}^* dt)$ for various particle orientations (ψ) and particle sizes is shown. It is clear that the most relaxation occurs for the particle with the long axis aligned normal to the most active slip system ($\psi=0^\circ$). For the larger particle, no relaxation occurred when the long axis was 22.5° or less from the most active slip plane. The relaxation is similar for the case of $\psi=0^\circ$ for the particle sizes investigated, but more relaxation occurs for the smaller particle as the long axis rotates closer to the vertically aligned most active slip plane (1-11). It is also clear that the particle orientation with respect to the loading is less significant than the orientation with respect to the slip system. This is due to similar relaxation values occurring for angles of $\psi=135^\circ$ and $\psi=45^\circ$, 157.5° and $\psi=22.5^\circ$, and $\psi=112.5^\circ$ and $\psi=67.5^\circ$ (Figure 7.3). The orientation of the dispersed particles is therefore crucial in understanding how the relaxation of the eigenstrain leads to a relaxation of the stresses that can lead to failure at the particle-matrix interface.

7.2.3 Orientation Effects: Model 2

Figure 7.4 shows contour plots of the amount of eigenstrain relaxed at 10% nominal compressive strain for particles aligned with the long axis parallel to the most active slip plane (a) and normal to the most active slip plane (b). It is evident that the relaxation is more prevalent for the case with the particles aligned normal to the slip system. The aspect ratio of the particle with respect to the most active slip plane also has a significant effect on the amount of relaxation. In Figure 7.5, a comparison between the amount of eigenstrain relaxed as a function of the aspect ratio with respect to the most active slip plane (defined in Figure

7.1) is depicted. Particles with small aspect ratios relax more readily than those with large aspect ratios. No relaxation was calculated for particles with an aspect ratio larger than 2.5.

The von Mises stress contours for the cases with the particles aligned with the long axis parallel to the most active slip plane and normal to the most active slip plane are shown in Figure 7.6. The stress buildups in the vicinity of the particle are greater in the direction of the long axis of the particle. This allows for more particle interaction when the particles are aligned with the long axis parallel to the most active slip plane.

These stress buildups lead to increased plastic shear slip (Figure 7.7). The plastic slip is highly localized at the particle-matrix interface when the particles are aligned with the long axis parallel to the most active slip plane. Also, the distribution of plastic slip is more localized in this case, forming more localized bands in comparison to the case where the particles are normal to the most active slip plane.

Figure 7.8 shows the mobile dislocation density on the most active $(1-11)[-101]$ and secondary $(-1-11)[-110]$ slip systems. The distribution of these densities follows the distribution of the stress accumulations. This change in slip distribution near the particle-matrix interface allows for the particles to rotate, which relaxes the eigenstrain. Particles that relaxed the most are those associated with secondary dislocations generated away from the intersection of the particle and the most active slip plane.

Figure 7.9 details the evolution of the amount of relaxation in each particle for orientations normal to and parallel to the most active slip-system. It is apparent that the particles aligned parallel to the most active slip plane relax less than those aligned normal to the most active slip plane. Many of the particles (16 of 22) aligned with the long axis

parallel to the most active slip plane lose the ability to relax at approximately 3% macroscopic strain. This is significant due to the fact that if relaxation did not occur, the eigenstrain would continue to build with increased plastic straining of the matrix, increasing the stress accumulations and leading to particle failure or failure at the particle-matrix interface.

7.2.4 20 Grain Aggregate: Model 3

To further investigate the effects of orientation and particle dispersion, a 20-grain aggregate with 20 randomly oriented particles was modeled. Figure 7.10 shows the stress distribution using von Mises and pressure contours. There are the build-ups of von Mises stresses in the vicinity of the particles that extend both parallel to and normal to the most active slip plane. There is also a buildup of tensile pressures at the particle-matrix interfaces for vertically aligned interfaces, which are parallel with the loading. This would not occur at this strain if the eigenstrain was not accounted for in the formulation.

These predictions are consistent with experimental characterization observations. For quasi-static experiments, nanocracks, propagating at right angles with respect to each other, and void nucleation at the particle-matrix interfaces have been observed, and the predicted von Mises stress build-ups occur in regions of observed nanocracking. Void nucleation due to shear and compressive deformation was also observed (Salem, Lee et al. Submitted). The predictions indicate this can be due to increased tensile pressures at the particle-matrix interfaces due to Orowan looping. This tendency for tensile failure can change the mode of failure from shear localization to a void sheet mechanism.

In Figure 7.11, a comparison between the calculated slip activity with and without the eigenstrain formulation is shown. Two trends can be noted. First, as should be expected, the slip activity increased local to the particle due to the build-ups in stress at the interface. Also, it can be seen that slip is limited further away from the particle in line with the particle in the most active slip plane. This indicates the backstress effects of the eigenstrain associated with Orowan looping.

Figure 7.12 shows the percent of the eigenstrain that was relaxed ($(\int D_{12,max\ shear}^* dt - \int D_{12,max\ shear_relaxed}^* dt) / \int D_{12,max\ shear}^* dt$) and the lattice rotations. There are more positive lattice rotations in the particle than in the matrix, which would lead to relaxation. The matrix at the interface rotates to accommodate this particle rotation (Humphreys and Kalu 1990). Also evident is the orientation relationship with the most active slip plane, as with the single grain models, namely the eigenstrain in particles most normal to the most active slip plane relaxed more than the eigenstrain in particles with the long axis aligned nearly parallel to the most active slip plane.

7.3 Conclusions

An eigenstrain formulation for Orowan looping to account for incompatibilities in plastic strain associated with Orowan looping and plastic relaxation was coupled to a dislocation density based crystalline plasticity formulation and a microstructurally-based finite-element framework to understand the effects of dispersed particles on the behavior of a high strength aluminum alloy on physically relevant microstructural scales. This eigenstrain was determined from the plastic shear slip in the surrounding matrix grain and the relaxation

was determined by the differences in lattice rotation between the particle and matrix. The eigenstress field associated with Orowan looping includes increased von Mises stresses at locations that would be associated with extra half-planes of atoms due to Orowan loops and increased tensile pressures at the opposing corners. This can lead to matrix nanocracking and particle-matrix debonding. The long-range stress is reduced coincident with the most active slip plane due to the eigenstrain, which is the back-stress effect.

The orientation of the particles with respect to the most active slip plane had a major effect on how the matrix relaxed the eigenstrain in the particle by lattice rotation mechanisms. Decreasing the aspect ratio of the particle with respect to the most active slip plane increased the ability of the matrix to relax the eigenstrain in the particle. The modeling of relaxation and Orowan looping, with a dislocation density based crystalline plasticity formulation at the microstructural scale, can be a first step in tailoring the microstructure and optimizing the strengthening and toughening mechanisms of alloys and metals.

References—Chapter 7

- Atkinson, J. D., L. M. Brown, et al. (1974). “The Work-Hardening of Copper-Silica IV. The Bauschinger Effect and Plastic Relaxation.” Philosophical Magazine **30**(6): 1247-1280.
- Brown, L. M. and W. M. Stobbs (1971). “The Work-Hardening of Copper-Silica I. A Model Based on Internal Stresses, With No Plastic Relaxation.” Philosophical Magazine, **23**(185): 1185-1199.
- Humphreys, F. J. and P. N. Kalu (1990). “The Plasticity of Particle-Containing Polycrystals,” Acta Metallurgica et Materialia **38**(6): 917-930.
- Lee, W. M. and M. A. Zikry (2011). “Microstructural Characterization of a High-Strength Aluminum Alloy Subjected to High Strain-Rate Impact.” Metallurgical and Materials Transactions. A, Physical Metallurgy and Materials Science **42**(5): 1215-1221.
- Salem, H. A. G., W. M. Lee, et al. “Quasi-Static and High Strain-Rate Experimental Microstructural Investigation of a High Strength Aluminum Alloy.” Metallurgical Transactions A Submitted.

Tables and Figures—Chapter 7

Table 7.1: Material properties of aluminum matrix and manganese-bearing dispersed particles

Property	Matrix Value	Particle Value
Elastic Modulus, E	70 GPa	110 GPa
Poisson's Ratio, ν	0.33	0.33
Static Yield Strength, τ_s^α	200 MPa	∞
Rate Sensitivity, m	0.01	N/A
Reference Strain-rate, $\dot{\gamma}_{ref}$	0.001 s^{-1}	N/A
Burgers Vector, \vec{b}_v	$0.289 \times \{111\}\langle 110 \rangle \text{ nm}$	N/A
Initial ρ_m	10^{11} m^{-2}	N/A
Initial ρ_{im}	10^{13} m^{-2}	N/A
Saturation ρ_{im}	10^{14} m^{-2}	N/A

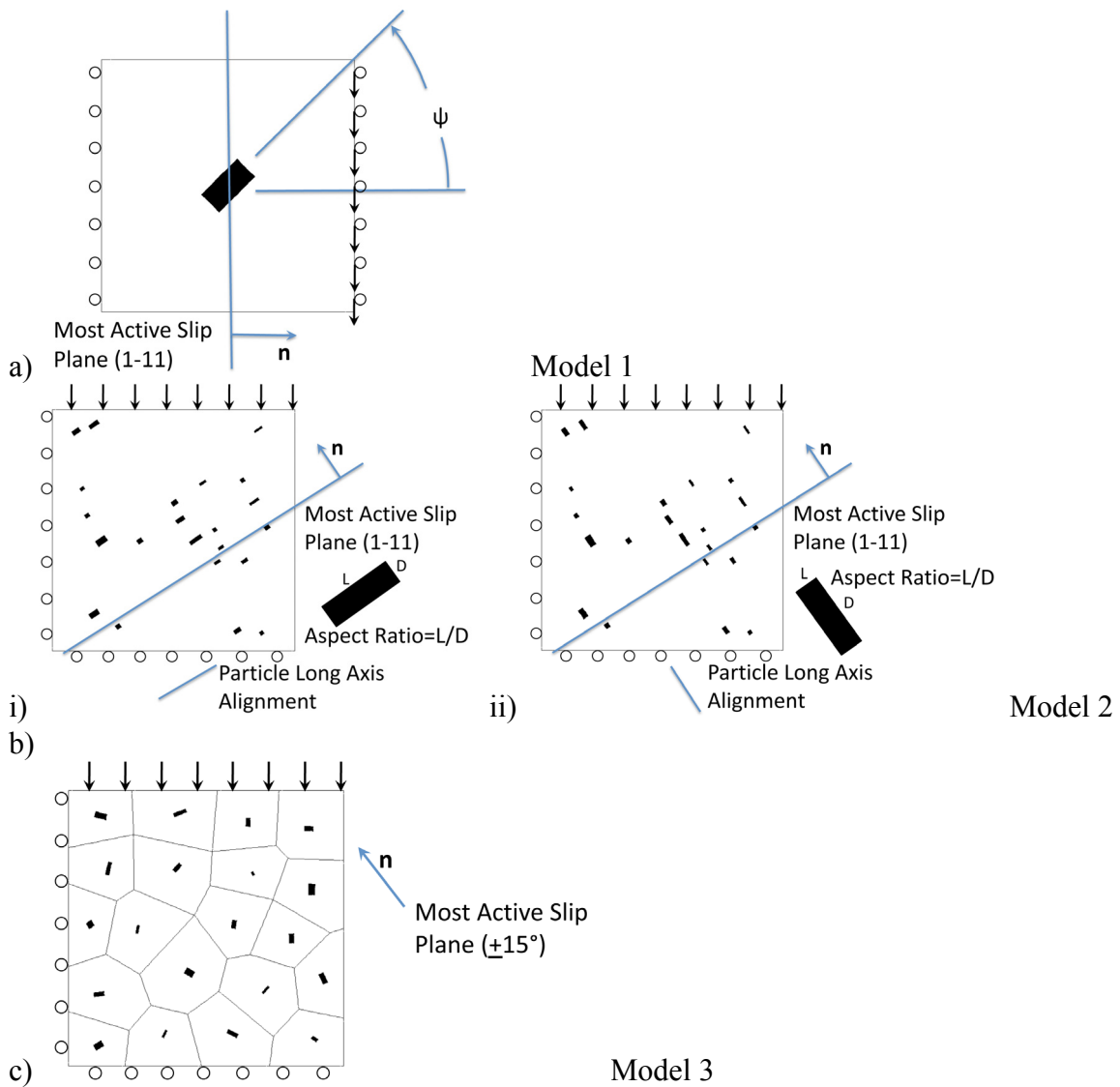


Figure 7.1: Finite element model: a) single particle model, b) single grain model; (i) particles aligned with long axis parallel to most active slip plane and (ii) particles aligned with long axis normal to most active slip plane, and c) 20 grain aggregate

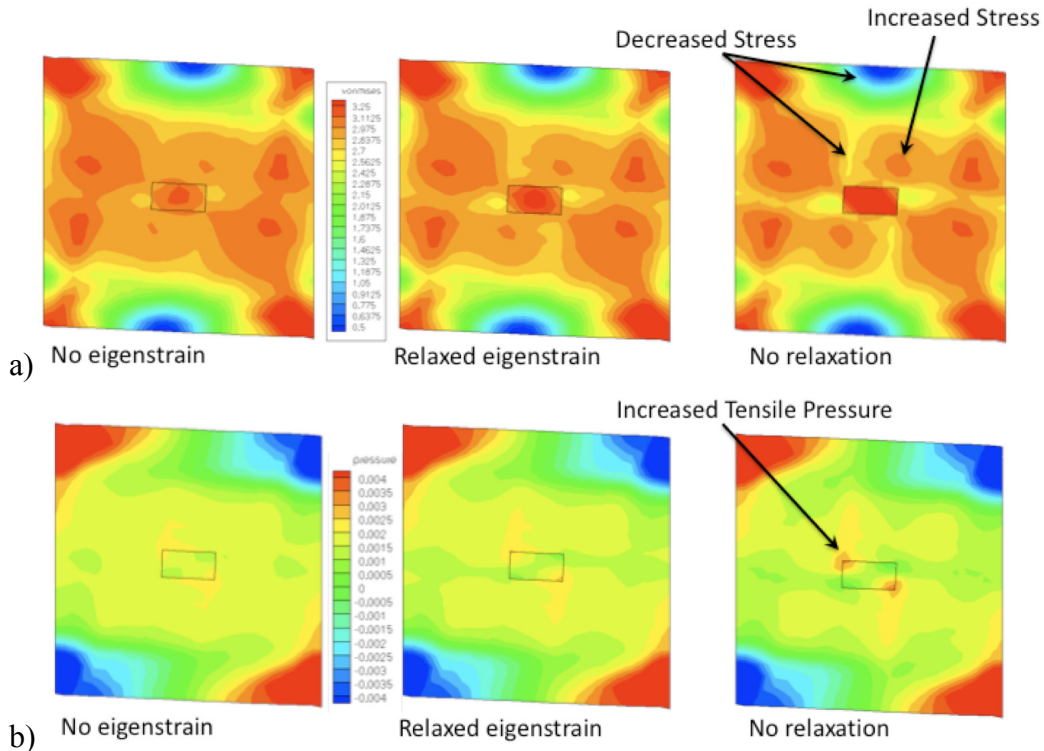
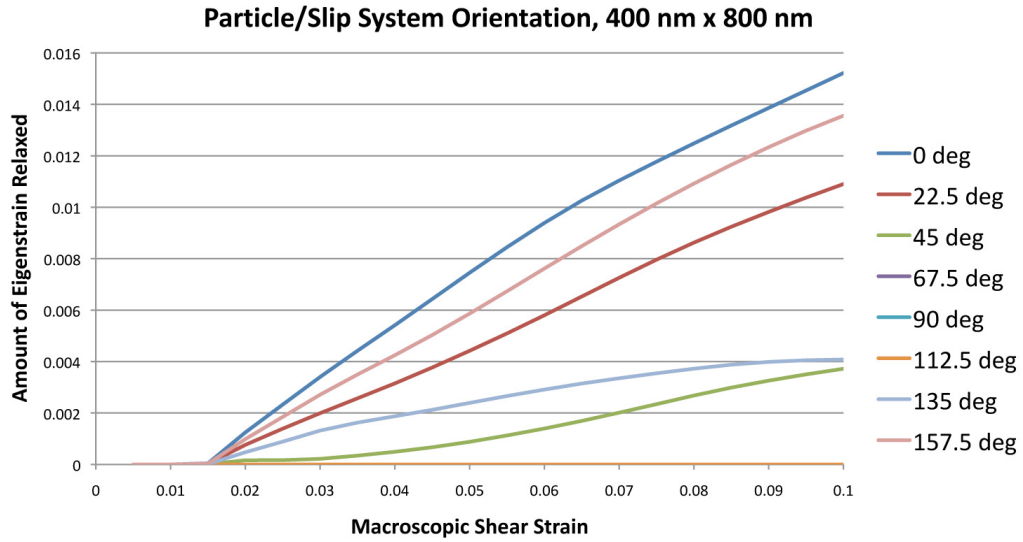
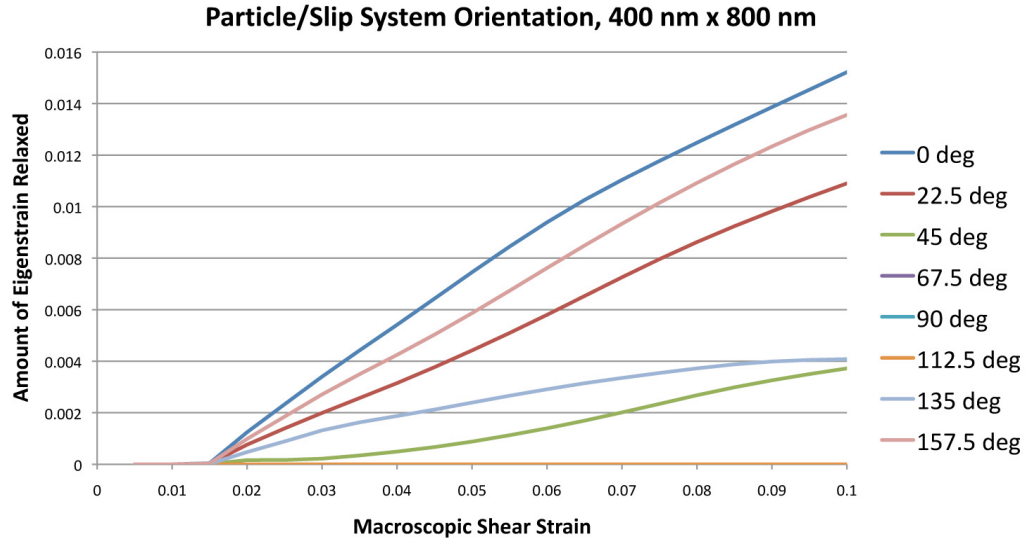


Figure 7.2: Contour plots of a particle under shear, a) von Mises stress accumulations (normalized by the matrix static yield stress) and b) tensile pressure accumulations (normalized by the matrix Young's modulus) for a single 400 nm by 800 nm particle aligned with the long axis oriented normal to the most active slip plane



a)



b)

Figure 7.3: Amount of eigenstrain relaxed at different particle orientations; a) 200 by 400 nm particle and b) 400 by 800 nm particle

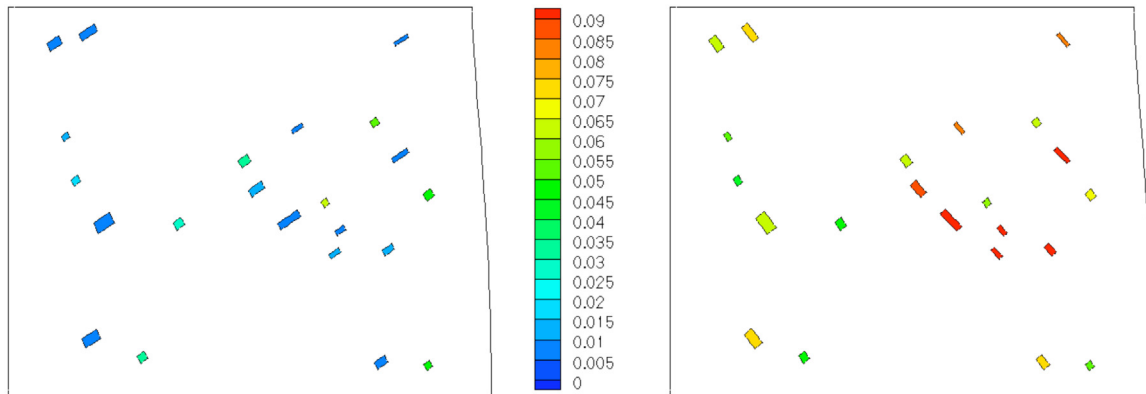


Figure 7.4: Contour plots of the amount of eigenstrain relaxed at 10% nominal compression; a) particles aligned with long axis parallel to most active slip plane (1-11) and b) particles aligned normal to most active slip plane (1-11)

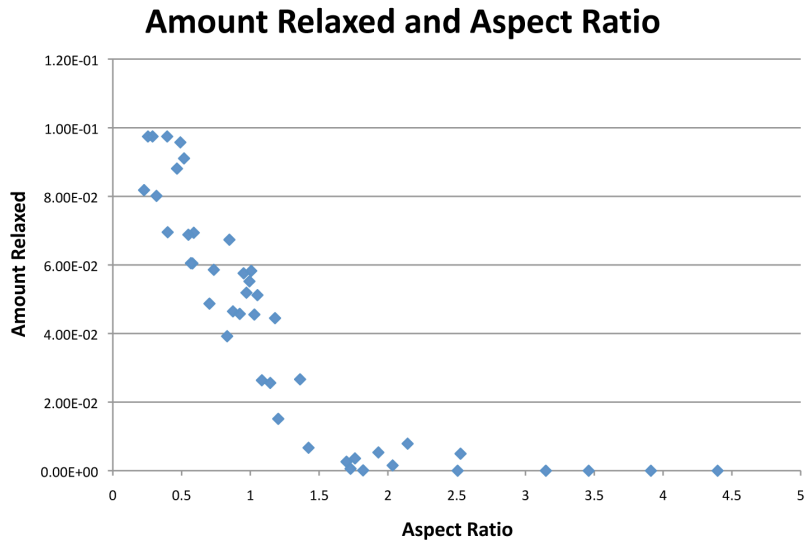


Figure 7.5: Comparison of the amount of eigenstrain relaxed in Figure 4 plotted as a function of the aspect ratio with respect to the most active slip plane

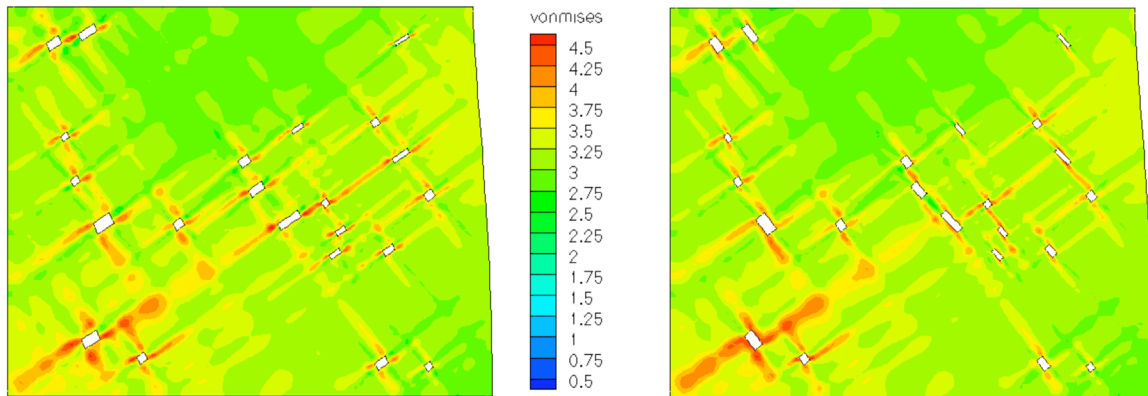


Figure 7.6: Contour plots of the von Mises stress in the matrix (normalized by the matrix static yield stress) at 10% nominal compression; a) particles aligned with the long axis parallel to most active slip plane (1-11) and b) particles aligned normal to most active slip plane (1-11)

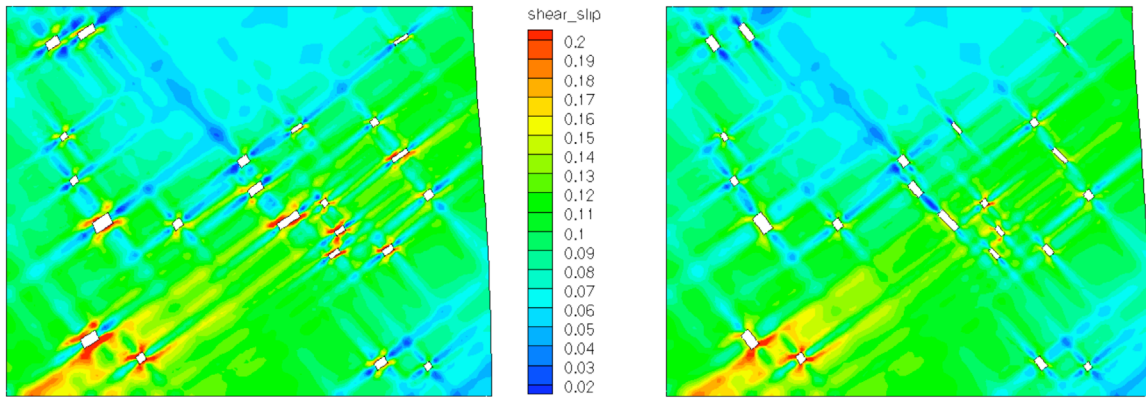


Figure 7.7: Contour plots of the effective plastic shear slip in the matrix at 10% nominal compression; a) particles aligned with long axis parallel to most active slip plane (1-11) and b) particles aligned normal to most active slip plane (1-11)

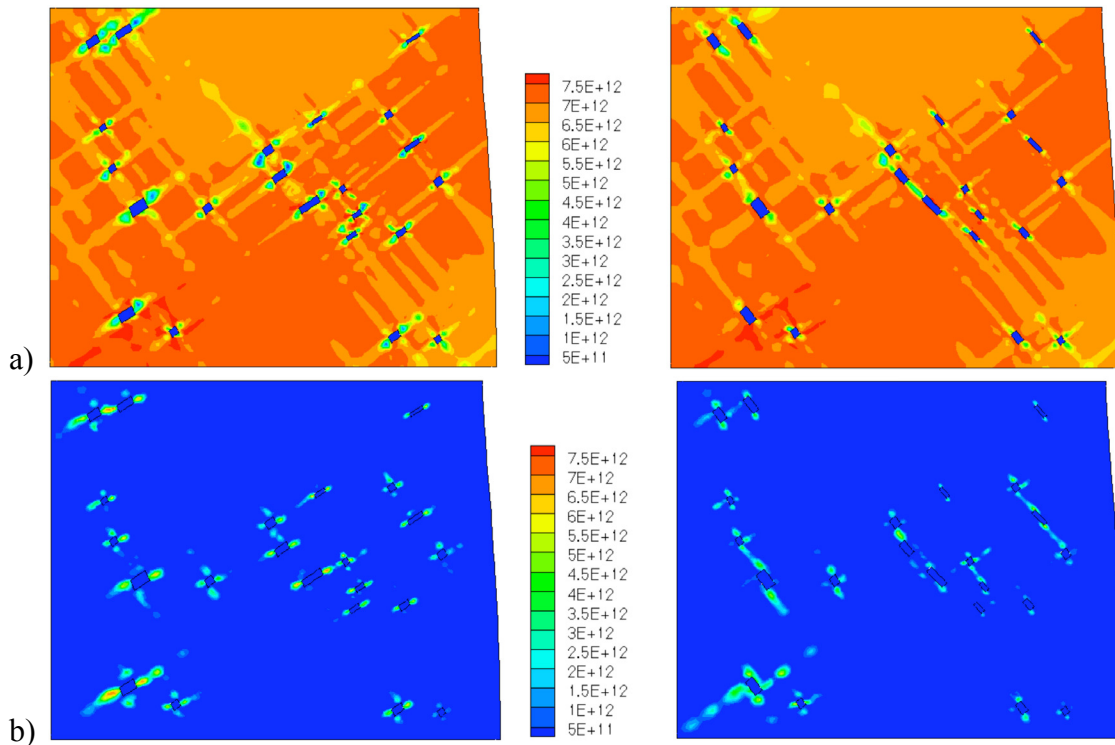


Figure 7.8: Contour plots of the mobile dislocation density (m^{-2}) on the (a) most active $(1-11)[-101]$ and (b) secondary $(-1-11)[-110]$ slip system at 10% nominal compression

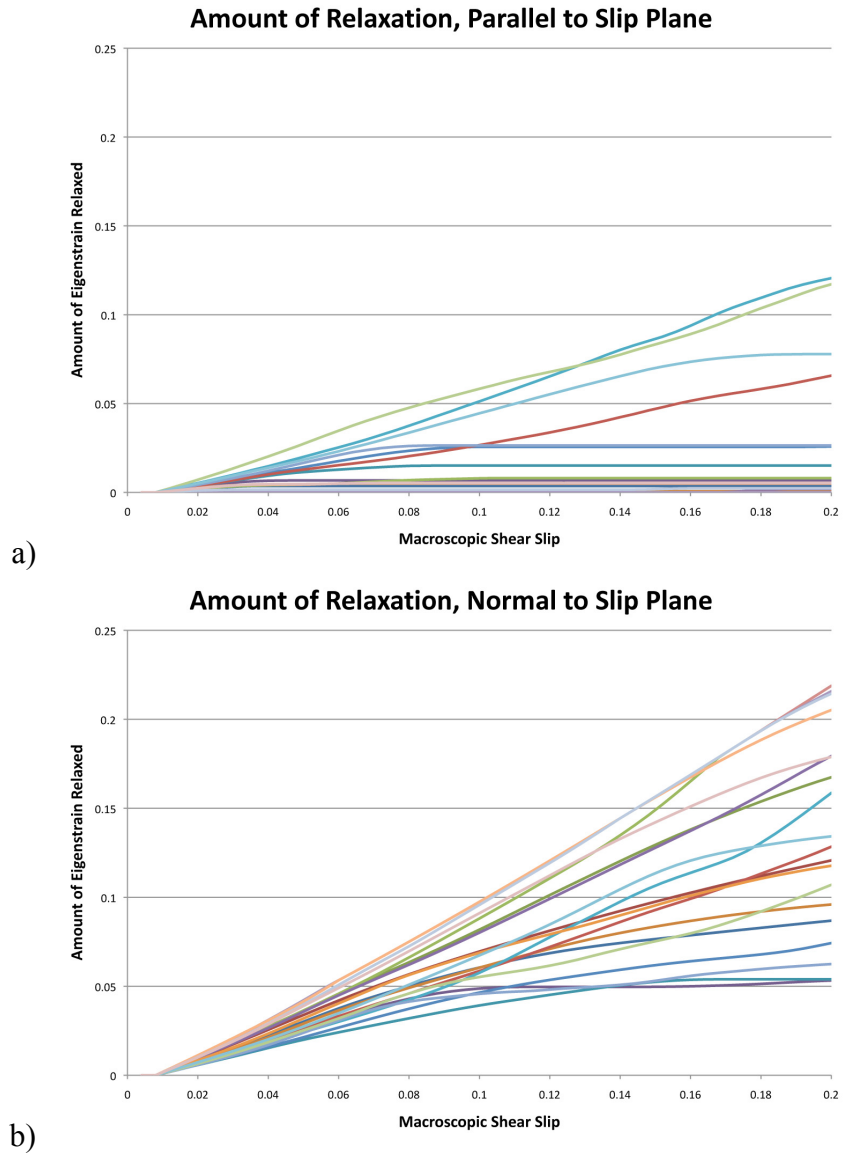


Figure 7.9: Evolution of the amount of relaxation for particles a) aligned parallel to the most active slip plane and b) aligned normal to the most active slip plane

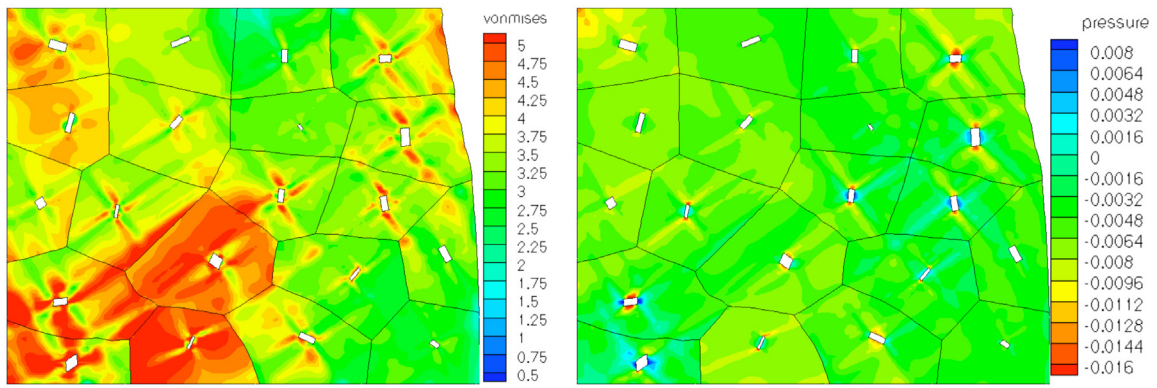


Figure 7.10: von Mises (normalized by the matrix static yield stress) and pressure (normalized by the matrix Young's modulus) contours for the matrix of 20-grain aggregate subjected to 10% nominal compressive strain

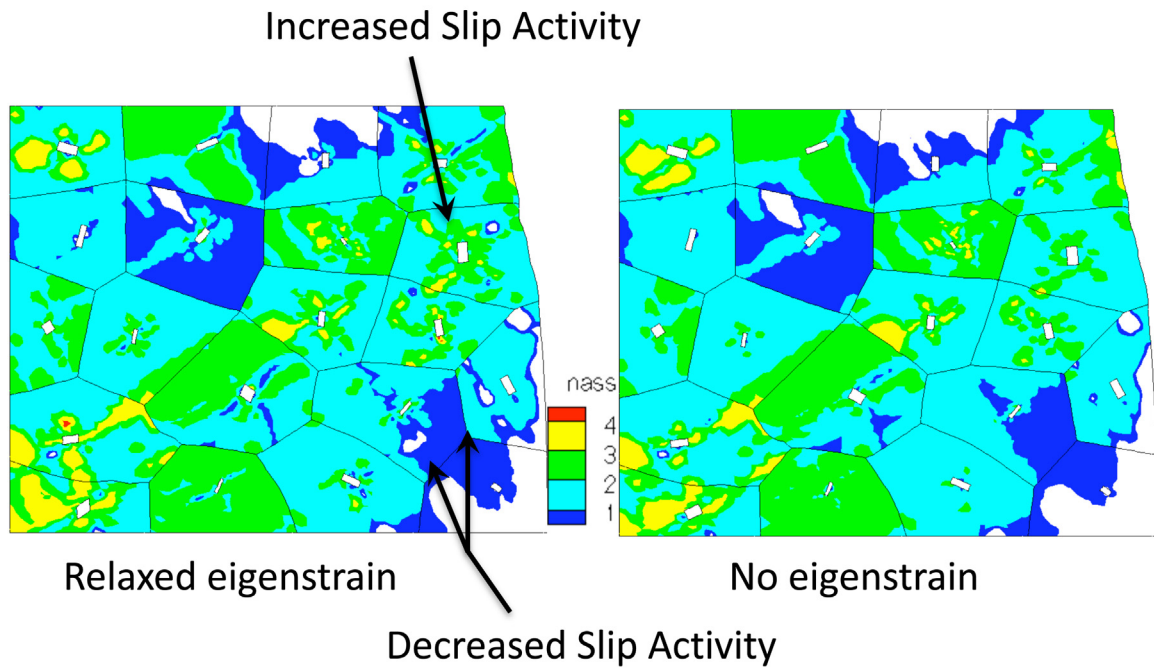


Figure 7.11: Contour plots of the number of active slip systems for the simulations with and without the eigenstrain formulation

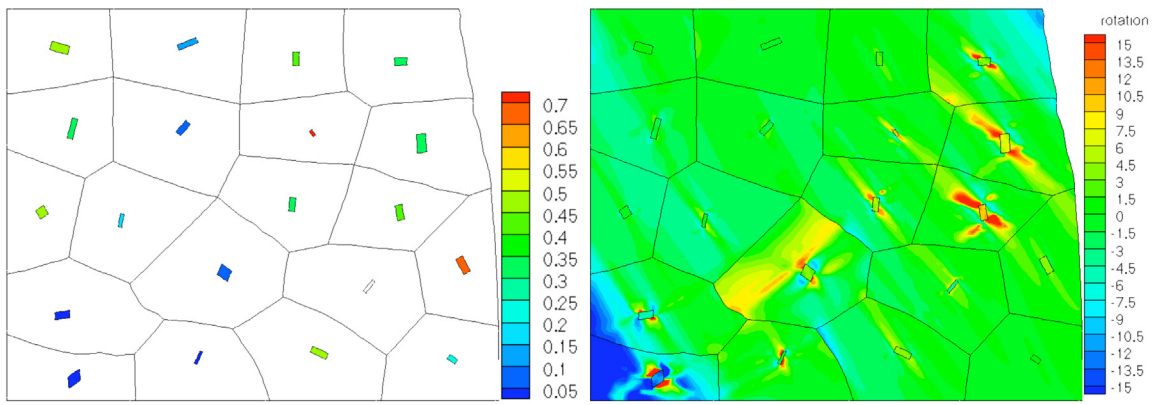


Figure 7.12: Contour plots of a) percent of eigenstrain relaxed and b) lattice rotations for the 20-grain aggregate

Chapter 8: High Strain-Rate Modeling of the Interfacial Effects of Dispersed Particles in High Strength Aluminum Alloys

8.1 Introduction

The major objective of this investigation is to use the dislocation density based crystal plasticity formulation and specialized microstructurally based finite element models outlined in Chapters 3 and 4 in conjunction with the eigenstrain representation of Orowan looping and unrelaxed strains outlined in Chapter 6 to investigate the effects of dispersed particles, including unrelaxed plastic strain and its evolution and subsequent relaxation, as a function of particle morphology, distribution, and orientation, as well as grain boundary (GB) misorientations, when the alloy is subjected to high strain-rate deformation. Specifically, how do the dispersed particles, which have been shown to promote transgranular failure (Starke and Sanders 1980), interrelate with the GB misorientations to control the response of the alloy to high strain-rate loading, as was investigated by microstructural characterization in Chapter 2. Therefore, a major focus will be placed on delineating the effects of dispersions of these particles and GB misorientations on possible failure modes, such as shear strain localization and particle-matrix interfacial stress accumulations, which can lead to void nucleation and debonding at particle-matrix interfaces.

8.2 Results

8.2.1 Microstructural Representation

Two high strain-rate cases were investigated, with stiffness based hourglass control used as outlined in Section 4.1. The first investigated case was a 20 μm by 20 μm single

crystal, modeled in adiabatic plane strain, subjected to a compressive strain-rate of $50 \times 10^3 \text{ s}^{-1}$ with different particle dispersions and particle sizes. The effects of particle spacing were investigated by modeling 1.0% volume fraction of randomly distributed dispersed particles with different particle sizes. The particle sizes were generated by a Gaussian distribution about averages of 600 nm x 300 nm for the smaller particle spacing and 850 x 425 nm for the larger particle spacing. The effects of particle size were investigated by modeling different particle sizes while maintaining the same particle distribution. Particles were randomly distributed and sized about an average of 600 nm x 300 nm to account for a volume fraction of 0.5%, and scaled up to 850 nm x 425 nm to account for a volume fraction of 1.0% to investigate larger particle sizes. Finally, volume fraction effects were investigated using randomly distributed particles sized about the experimentally observed mean of 600 nm by 300 nm (Lee and Zikry 2011) at volume fractions of 0.5%, 1.0%, and 1.5%. The matrix lattice was aligned for preferential slip along the (1-11) plane as indicated in Figure 8.1 with Euler angles of $\varphi_1 = -45^\circ$, $\Phi = -19.7^\circ$, and $\varphi_2 = 0.0^\circ$. Symmetry boundary conditions were used and two dispersed particle configurations were investigated: (i) the long axis of all particles aligned parallel to the initially preferential slip plane of (1-11), and (ii) the long axis of all particles aligned normal to the initially preferential (1-11) slip plane. A mesh of approximately 18,600 elements was used with a minimum of three elements along each particle side.

The second case that was investigated was 20 μm by 20 μm polycrystalline aggregates with randomly oriented and sized particles to understand how and whether grain orientations affect interfacial behavior pertaining to the dispersed particles. Three aggregates

with a distribution of one particle per grain to account for a 1.0% volume fraction were investigated: a 20-grain aggregate with an average particle size of 600 nm x 300 nm, a 35-grain aggregate with an average particle size of 500 nm x 250 nm, and a 48-grain aggregate with an average particle size of 400 nm x 200 nm. Random high angle and low angle GB misorientations between the crystal grains were used. Table 8.1 summarizes the average grain misorientations for each scenario. A strain-rate of $50 \times 10^3 \text{ s}^{-1}$ with plane strain adiabatic compression and symmetry boundary conditions were used. An isothermal quasi-static case with a strain-rate of 0.004 s^{-1} was also conducted to fully understand how variations in strain-rate affect behavior. A mesh of approximately 16,000 elements was used, with a minimum of three elements along each particle side. Figure 8.1 summarizes the models used for the two cases. The properties of the particles and matrix grains are summarized in Table 8.2.

The third investigated case was a 20 μm by 20 μm , 20-grain polycrystalline aggregate with low angle random GB misorientations subjected to a 1 GPa compressive pressure load. Plane strain, adiabatic simulations were conducted without dispersed particles and with dispersed particles with an average size of 600 nm by 300 nm. The load was applied for 1.57×10^{-9} s, at which point the wave had propagated through approximately 50% of the model, then immediately released. Fixed BCs were implemented along the bottom edge.

8.2.2 *Single Grain*

8.2.2.1 Particle Spacing Effects

The effects of particle spacing were investigated for a 1.0% volume fraction of randomly distributed dispersed particles with different average particle sizes of 600 nm x 300

nm (smaller spacing) and 850 nm x 425 nm (larger spacing) as shown in Figure 1a. The contours of effective plastic shear slip for particles aligned parallel to and normal to the most active slip plane are shown in Figure 8.2. For both particle alignments, with more closely spaced dispersed particles, the effective shear slip develops into three slip bands that extend to approximately one-third of the crystal, as compared to the more diffuse shear slip associated with the larger particle spacing. This indicates that the spacing of particles has a pronounced effect on the shear slip distribution.

Figure 8.3 details the pressure distribution for the different particle spacings. It is evident that for the models with particles aligned parallel to the most active slip plane (Figure 8.1), tensile pressures accumulate at the particle-matrix interface to a greater extent than for the particles aligned normal to the most active slip plane. Particle interactions can also be clearly seen for the particles aligned parallel to the most active slip plane. The compressive pressures between the particles are smaller than the mean value in the matrix. This reduction in the compressive pressures can promote faster void coalescence once voids are nucleated at the particle-matrix interface. This effect is more pronounced for the larger particles (Figure 8.3).

8.2.2.2 Particle Size Effects

The effects of particle size were investigated by modeling different average particle sizes, 600 nm x 300 nm (0.5% volume fraction) and 850 nm x 425 nm (1.0% volume fraction) while maintaining the same particle dispersion and orientation (Figure 8.1a). The pattern of shear slip is largely unaffected by particle size, but the intensity of plastic shear slip increases as the particle size increases, with plastic strains that are generally larger than

those associated the smaller dispersed particles. This is due to the difference in stress accumulations for the particles of different sizes, as can be seen from the von Mises stress and pressure contours of Figure 8.4. The larger dispersed particles generally have larger accumulations near the interfaces of the dispersed particles.

This difference in stress accumulations can be understood in terms of the unrelaxed plastic strain at the interfaces of the dispersed particles. The eigenstrain in each particle initially is the negative of the plastic strain in the surrounding matrix grain (eqn. 6.2). For both particle sizes, the amount of plastic relaxation was similar. Therefore, the relaxed eigenstrain in each particle is similar. The eigenstrain is proportional to the number of Orowan loops and the particle size (Brown and Stobbs 1971), with the number of Orowan loops increasing with particle size. The loops lead to a greater eigenstresses, and therefore greater stress accumulations at the particle matrix interface.

The effect of these greater eigenstresses can be seen by the pressure contours of Figure 8.4. The interaction between the particles, leading to decreases in the compressive pressures between the larger particles, can enhance the nucleation and eventual coalescence of voids, which indicates that smaller particles may be beneficial in delaying final void coalescence. This underscores that particle size has a critical role in failure evolution.

8.2.2.3 Volume Fraction Effects

The effects of volume fraction were investigated by comparing particle dispersions with volume fractions of 0.5%, 1.0%, and 1.5% and an average particle size of 600 nm by 300 nm in a single 20 μm by 20 μm single crystal (Figure 8.1a). The volume fraction clearly affects the pattern of plastic slip, which can be seen in Figure 8.5, for particles initially

aligned normal to the most active slip plane. For the 0.5% volume fraction case, the particle effects on the shear slip distribution are minimal, since there is a larger particle spacing (Figure 8.5, see also Figure 8.2b). As the volume fraction is increased to 1%, the shear slip forms a banded distribution, with distinct bands associated with the dispersed particles (Figure 8.5). As the particle spacing is reduced due to the further increase of volume fraction to 1.5%, the shear slip becomes highly localized between the particles, which can lead to the onset of shear failure between the particles, with shear band initiation at the particle-matrix interface.

The effect of volume fraction on the relaxation of the eigenstrain can be seen in Figure 8.6. For particles aligned parallel to the most active slip plane, which show little relaxation for all cases, there is a much greater percentage of particles that do not relax for the highest volume fraction of 1.5%. This indicates that as the volume fraction increases, relaxation becomes more difficult. This effect was greater for the particles aligned parallel to the most active slip plane than those aligned normal to the most active slip plane.

8.2.3 Polycrystalline Aggregate and Dispersed Particle Distributions

To investigate the interrelated effects of dispersed particles and grain orientations, three 20 μm by 20 μm polycrystalline aggregates were studied: a 20-grain aggregate with an average particle size of 600 nm x 300 nm, a 35-grain aggregate with an average particle size of 500 nm x 250 nm, and a 48-grain aggregate with an average particle size of 400 nm x 200 nm. In each case, the particle volume fraction was 1%, and both random high angle and random low angle GB misorientations were investigated (Table 8.2). Figure 8.7 compares the behavior of the high angle 20-grain aggregate for compressive strain-rates of $4 \times 10^{-3} \text{ s}^{-1}$

and $50,000 \text{ s}^{-1}$ with and without the eigenstrain formulation to determine how strain-rate variation affects eigenstrains.

For all the cases, a shear band develops at the triple junction located at the bottom left of the top right grain. The band propagates to the free boundary bypassing the dispersed particle near the free boundary at the particle-matrix interface. The propagation of the band in the other direction depends on the strain-rate and whether or not the eigenstrain formulation is included in the simulation. Under quasi-static loading conditions, without the eigenstrain, the band propagates to the interface of the particle marked by an arrow in Figure 8.7a. When the eigenstrain formulation is included, the eigenstress field associated with the eigenstrain alters the path of the shear band away from the particle, which also reduces the intensity of the band.

The difference in the two bands, for the strain-rate of $50,000 \text{ s}^{-1}$, with and without the eigenstrain, is minimal in comparison with the quasi-static cases. Some broadening of the band is seen near the particle marked by an arrow in Figure 8.7b. However, the general path of the band is largely unaffected by the eigenstrains. This indicates that the effects of thermal softening, which occurs due to the temperature rise associated with the high strain-rate deformation (Figure 8.8), may be more dominant than the eigenstrain effects. As evident from Figure 8.8, there is considerable thermal accumulation within the band.

The effects of the grain orientations and eigenstrain relaxation can be seen in for low angle (Figures 8.9) and for high angle (Figure 8.10) GB misorientations. For all low angle GB aggregates, slip localizes to some extent in the general orientation of the most active slip plane (see Figure 8.1b). For the 20-grain aggregate, plastic shear slip localization occurs at

the particle matrix interface of two particles that are associated with the lowest relaxation (Figure 8.9b). The localization does not fully extend to the free boundary, where the particles near the free boundary do relax. The local deformation behavior of the 35-grain and 48-grain low angle aggregates is associated with particles that minimally relax and at grain junctions of 3 and 4 grains. It is also evident that the highest effective plastic shear slip values occur at the particle-matrix interfaces.

Similar trends can be seen for the high angle GB aggregates (Figure 8.10). Highly localized deformation occurs for the 20-grain and 48-grain aggregates at the GBs, at grain junctions, and at particle-matrix interfaces of particles where the eigenstrain does not relax. Minimal localization is seen for the 35-grain aggregate, but some local behavior (see arrows, Figure 8.10a) is associated with a particle that shows minimal relaxation. The major difference between the deformation of the low angle and high angle GB aggregates is the interrelated effects of the particles and the GBs. The deformation of the low angle GB aggregates is associated with more local shear slip (Figure 8.9a) behavior at the particle-matrix interface, whereas the deformation of the high angle grain aggregates is more local at the GBs and grain junctions. The GBs at the lower left of the 20-grain and 48-grain aggregates are associated with highly localized shear slip, as is the triple junction at the top right of the 20-grain aggregate. These bands propagate to the interfaces of particles for which the matrix does not relax the eigenstrain.

Figure 8.11 displays the contours of the vertical component of the stress tensor associated with the wave propagation through the 20-grain aggregate model with low angle GB misorientations, both with and without dispersed particles. Figure 8.11a shows the stress

component at $t=2.985 \times 10^{-9}$ s. By this time, the pressure has been released from the top of the model. A compressive wave covers approximately half of the model, with a smaller tensile wave due to the sudden release of the pressure following the compressive wave.

As the waves reflect off of the fixed end, the compressive wave reflects as a compressive wave, and the tensile release wave reflects as a tensile wave. These waves propagate upward through the model, and reflect off of the free end. Figure 8.11b depicts the vertical stress component contours at $t=7.227 \times 10^{-9}$ s, after the leading edge of the compressive wave reflects off of the free end as a tensile wave. Figure 8.11c shows the contours of the vertical stress component at $t=7.384 \times 10^{-9}$ s, when the tensile reflection interacts with the tensile release wave. The effects of the particles can be seen in this figure. The stress field associated with the dispersed particles can increase the tensile stress in the region near the particle, which can enhance the possibility of spall failure. Therefore, it is suggested that larger dispersed particles, which are associated with higher tensile pressures and longer reaching stress fields, have a more detrimental effect on spall failure.

8.3 Conclusions

An eigenstrain formulation accounting for incompatibilities in plastic strain associated with Orowan looping and plastic relaxation coupled to dislocation density based crystalline plasticity and a microstructurally-based finite-element framework was used to investigate the interrelated effects of particle dispersion, orientation, size and spacing, and GB misorientations for a high strength aluminum alloy subjected to high strain-rate deformation. Particle spacing had a significant effect on plastic shear slip distribution, with interaction between the particles, including shear slip localization and decreasing

compressive pressure fields, occurring for smaller spacing. Larger particles had a greater effect on the stress fields near the particle-matrix interfaces, which led to longer range interaction of particle stress fields, including the tendency for decreasing compressive pressure fields developing between particles, which can enhance void nucleation and eventual coalescence.

For the polycrystalline aggregates with dispersed particles, shear strain localization occurred as a function of the particle eigenstrain, GB misorientations, and thermal softening. For low angle GB misorientations, shear strain localization can be triggered at the particle-matrix interfaces of particles where the eigenstrain is not relaxed. High angle GB misorientations led to the onset of shear slip localization, occurring first at GBs and grain junctions, and propagating to the particle-matrix interface of particles where the eigenstrains were not relaxed.

The interaction of the stress fields of the dispersed particles and those associated with wave propagation can enhance the stresses associated with spall local to the dispersed particles, indicating that the stress fields associated with the particles can enhance spall failure of the alloy when subjected to high strain-rate loading.

References—Chapter 8

- Brown, L. M., Stobbs, W. M., 1971. The Work-hardening of Copper-Silica I. A Model Based on Internal Stresses, With No Plastic Relaxation. Philosophical Magazine **23**:1185-1199.
- Lee, W. M., Zikry, M. A., 2011. Microstructural Characterization of a High-Strength Aluminum Alloy Subjected to High Strain-Rate Impact. Metallurgical and Materials Transactions A **42**:1215-1221.
- Starke, E. A., Sanders, T. H., 1980. The Effect of Microstructure on the Properties of High Strength Aluminum Alloys. AFOSR Annual Scientific Report. ADA083768.

Tables and Figures—Chapter 8

Table 8.1: Grain misorientation averages for polycrystalline aggregates (degrees)

	Low angle GB Misorientations	High angle GB Misorientations
20-Grain	12.9399	38.6500
35-Grain	13.0177	38.9619
48-Grain	12.8471	37.8406

Table 8.2: Material properties of aluminum matrix and manganese-bearing dispersed particles

Property	Matrix Value	Particle Value
Elastic Modulus, E	70 GPa	110 GPa
Poisson's Ratio, ν	0.33	0.33
Static Yield Strength, τ_s^α	200 MPa	∞
Rate Sensitivity, m	0.01	N/A
Reference Strain-rate, $\dot{\gamma}_{ref}$	0.001 s^{-1}	N/A
Burgers Vector, \vec{b}_v	$0.289 \times \{111\}\langle 110 \rangle \text{ nm}$	N/A
Initial ρ_m	10^{11} m^{-2}	N/A
Initial ρ_{im}	10^{13} m^{-2}	N/A
Saturation ρ_{im}	10^{14} m^{-2}	N/A

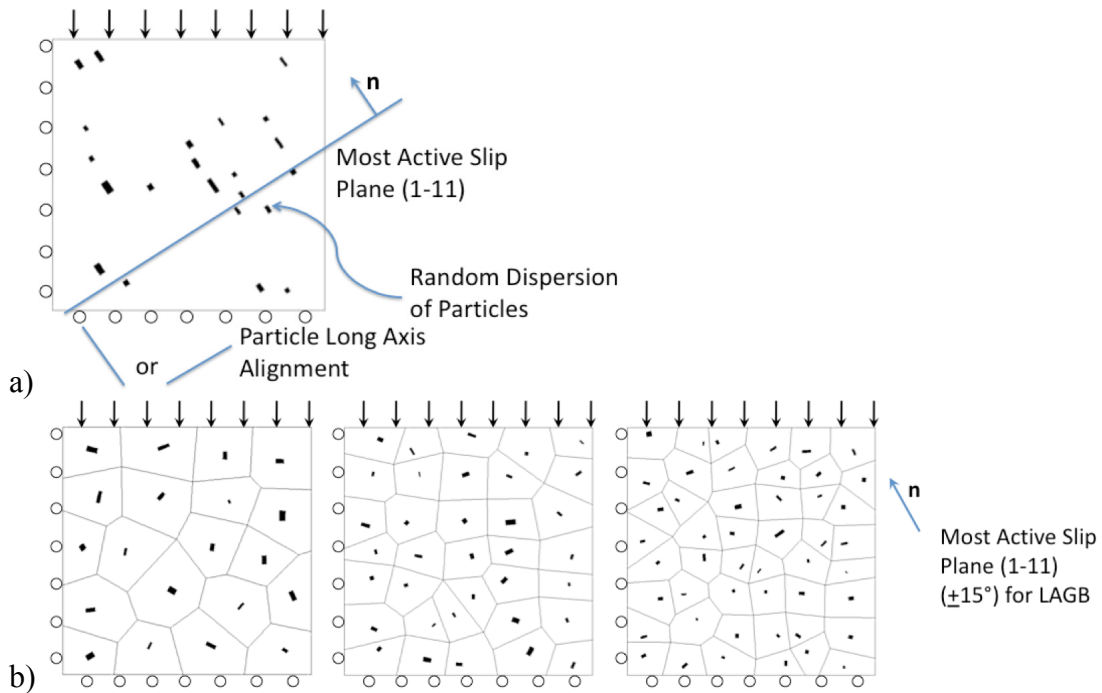


Figure 8.1: Summary of the investigated models: a) 20 μm by 20 μm single grain with random dispersions of particles and b) 20 μm by 20 μm polycrystalline aggregate with 20, 35, and 48 grains and with one dispersed particle per grain

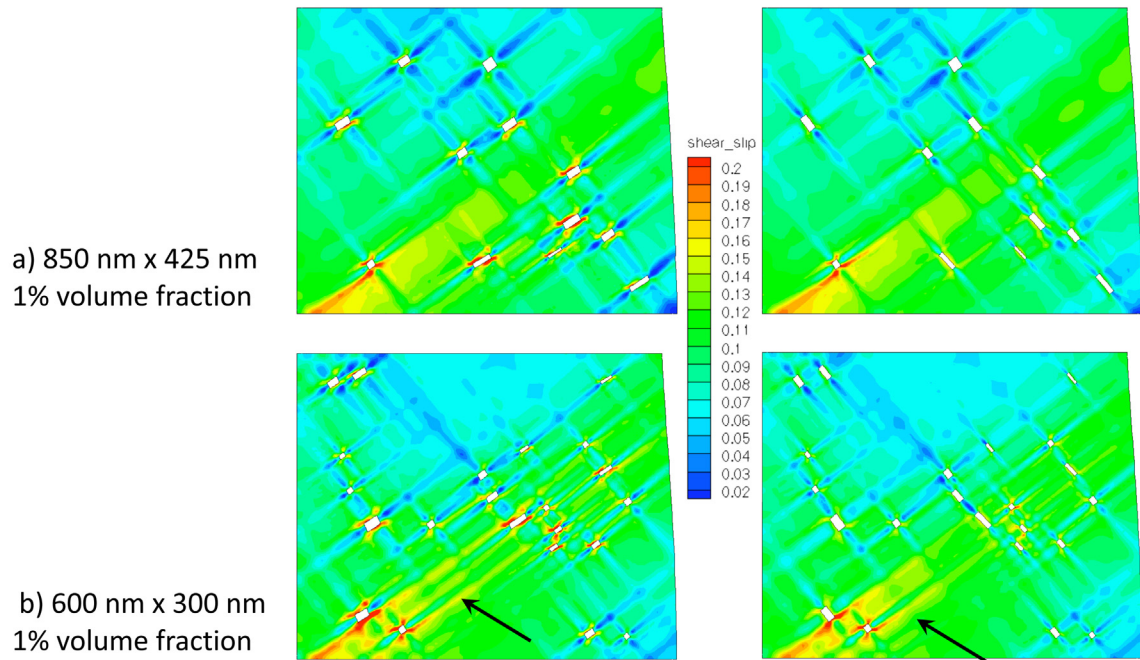


Figure 8.2: Effective plastic slip contours in the matrix at 10% nominal compressive strain for 1.0% volume fraction of particles in a single crystal at a strain-rate of $50 \times 10^{-3} \text{ s}^{-1}$: a) 800 nm by 425 nm average dispersed particle size and b) 600 nm by 300 average dispersed particle size. Arrows indicate banded slip

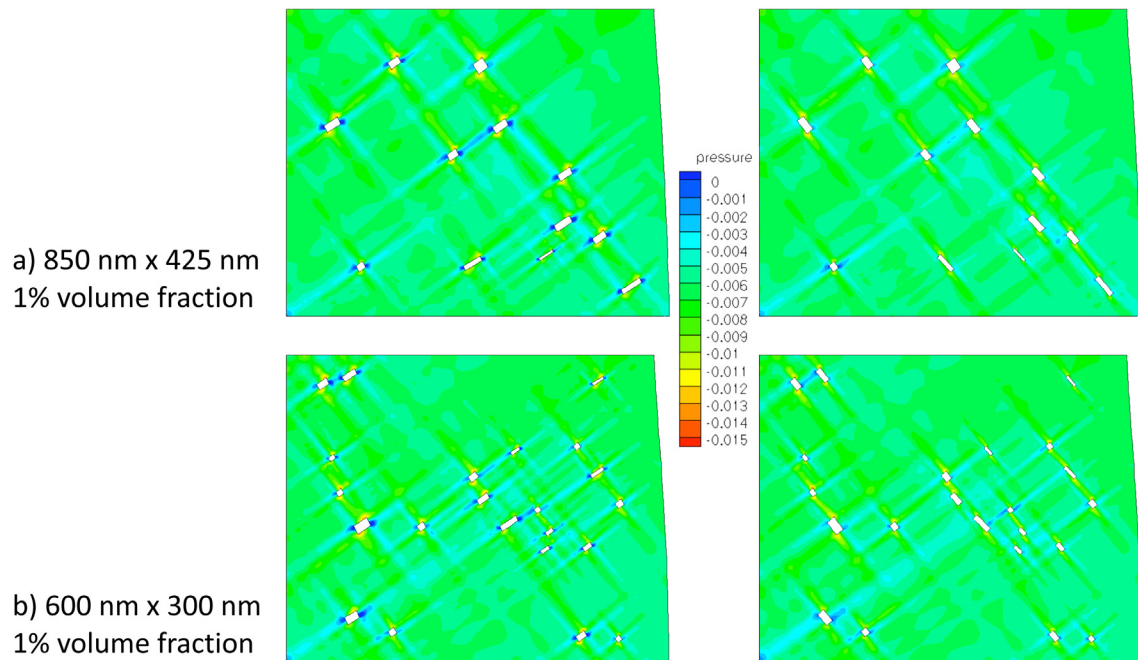
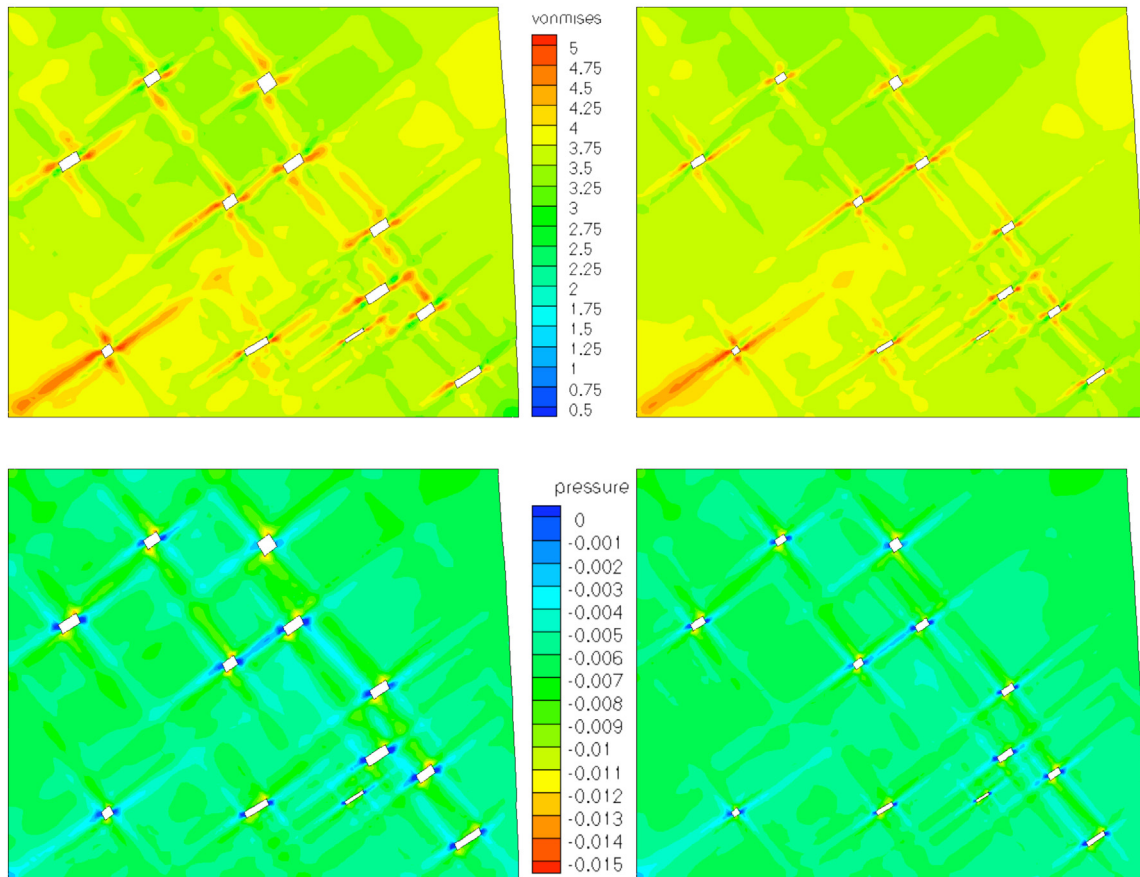


Figure 8.3: Pressure contours in the matrix (normalized by the matrix Young's modulus) at 10% nominal compressive strain for 1.0% volume fraction of particles in a single crystal: a) 800 nm by 425 nm average dispersed particle size and b) 600 nm by 300 nm average dispersed particle size. Contour levels set to emphasize decrease in compressive pressures and transition to tensile pressures at the particle-matrix interfaces



a) 850 nm x 425 nm,
1% volume fraction

b) 600 nm x 300 nm,
0.5% volume fraction

Figure 8.4: von Mises stress (normalized by the matrix static yield stress) and pressure (normalized by the matrix Young's modulus) contours in the matrix at a 10% nominal compressive strain for particles aligned parallel to the most active slip plane: a) 1.0% volume fraction, 800 nm by 425 nm average dispersed particle size and b) 0.5% volume fraction, 600 nm by 300 nm average dispersed particle size

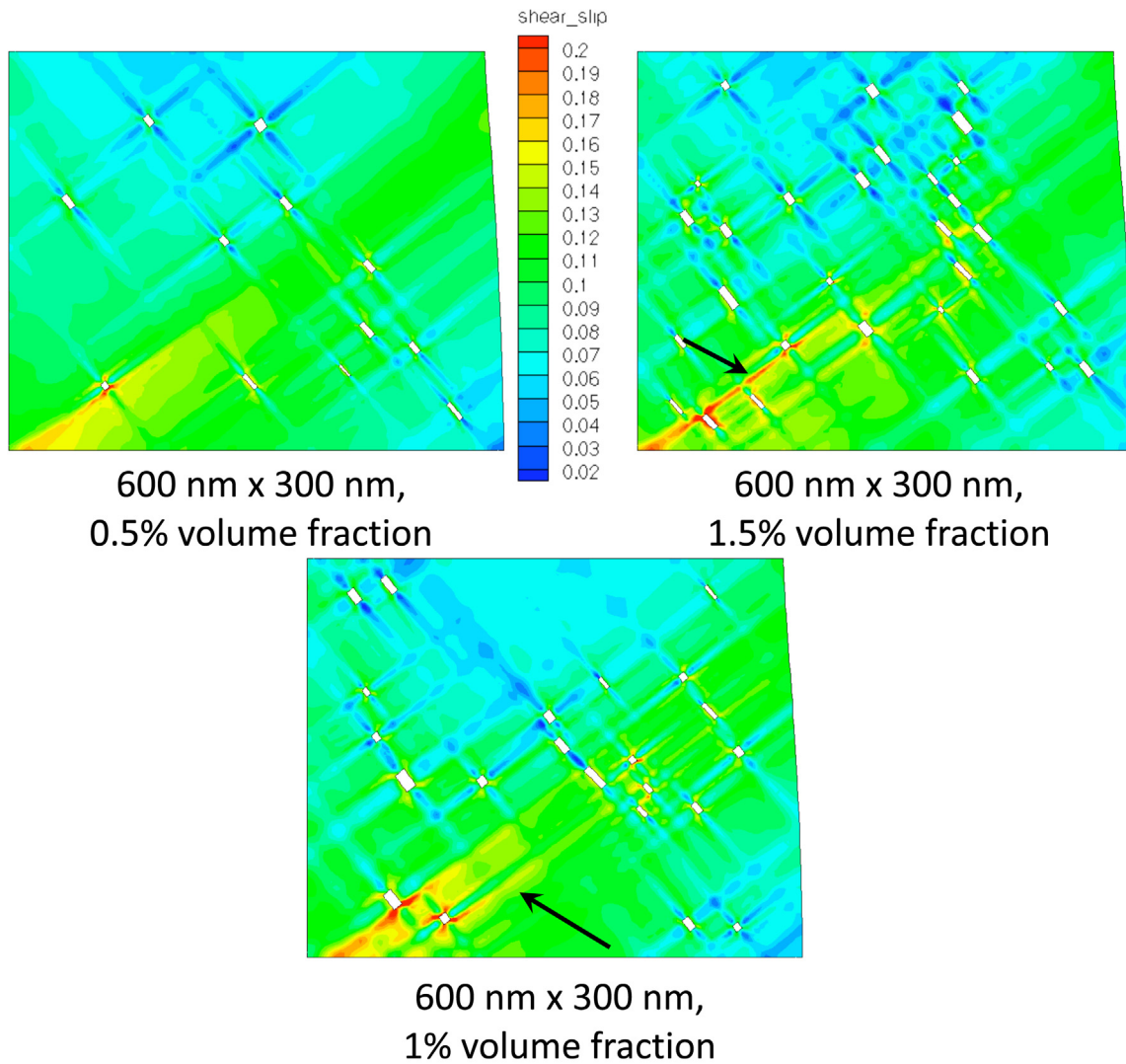


Figure 8.5: Matrix effective plastic shear slip comparison at 10% nominal compressive strain for 600 nm by 300 nm average size particles normal to most active slip plane for 0.5%, 1.0% (arrow indicates banded slip), and 1.5% volume fraction (arrow indicates slip localization between particles)

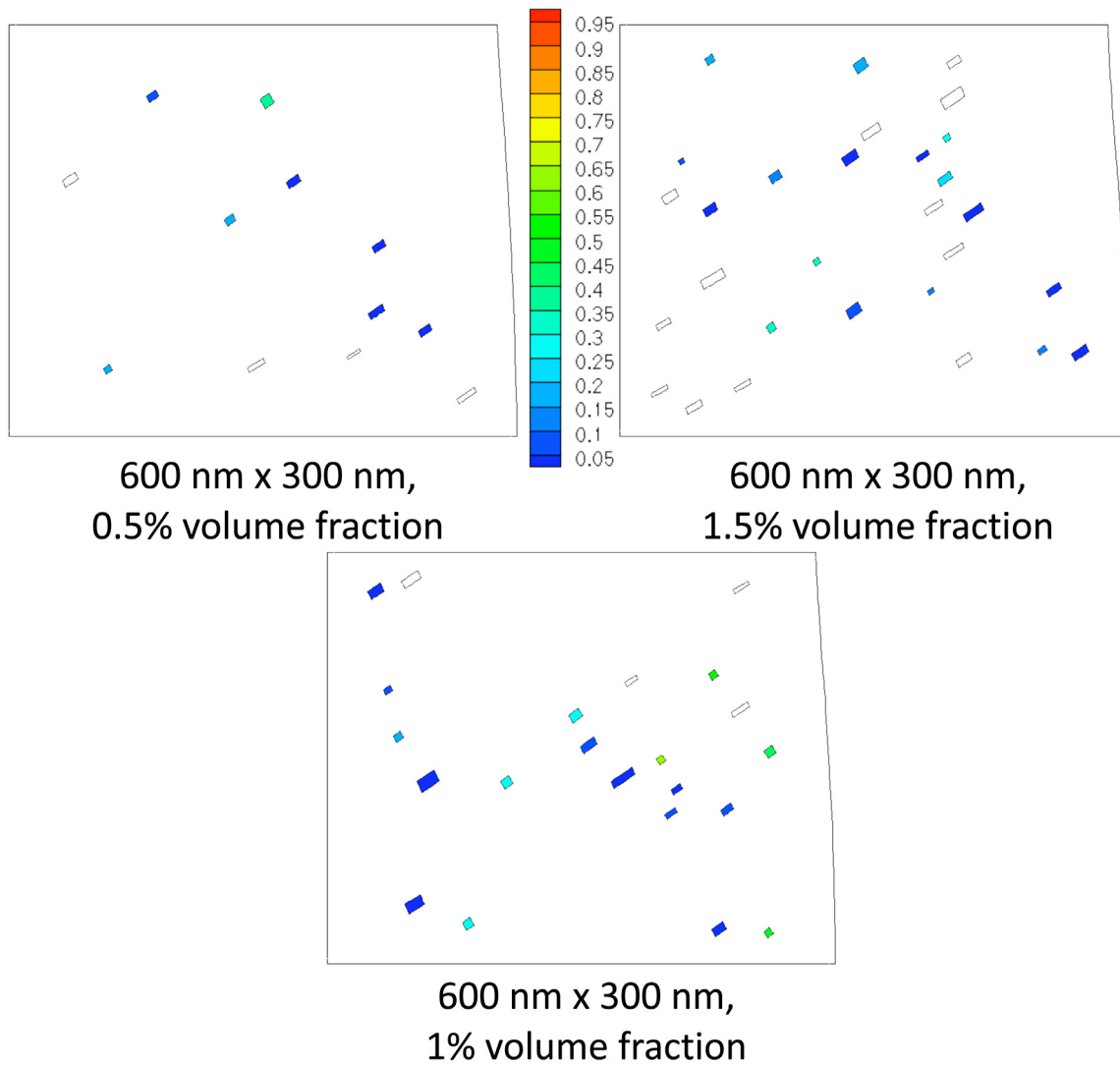


Figure 8.6: Percent of eigenstrain relaxed

$\left(\int D_{12, \max_shear}^* dt - \int D_{12, \max_shear_relaxed}^* dt \right) / \int D_{12, \max_shear}^* dt$ at 10% nominal compressive strain for 600 nm by 300 nm average size particles parallel to the most active slip plane for 0.5%, 1.0% and 1.5% volume fractions

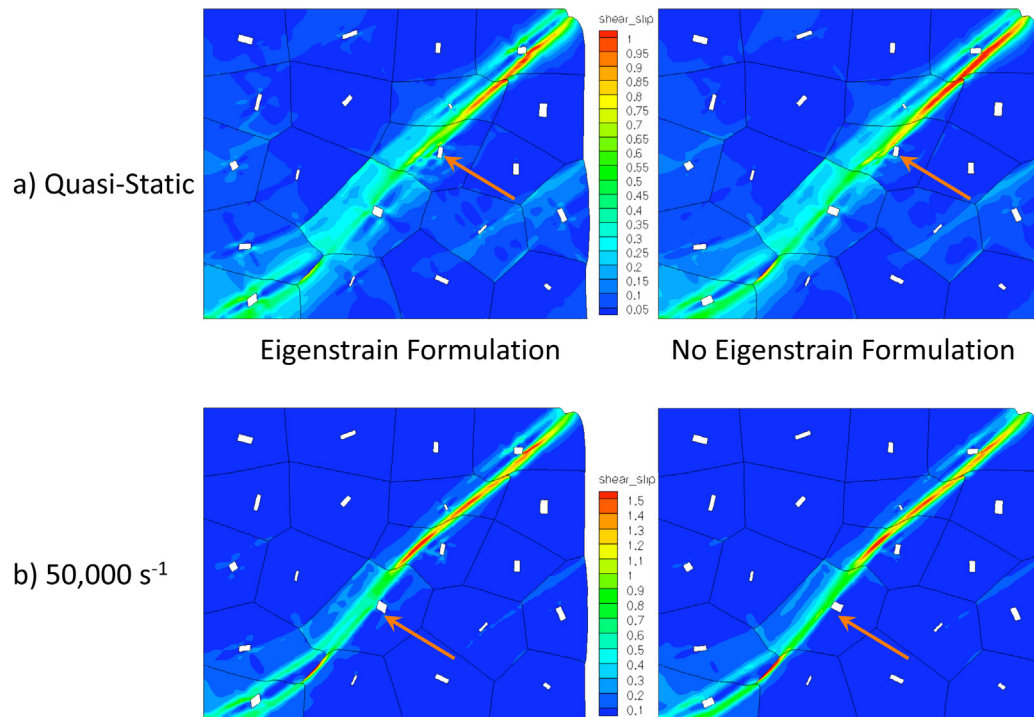


Figure 8.7: Comparison of effective plastic shear slip in the matrix at 10% nominal compressive strain for a 20-grain aggregate with high angle GB misorientations with and without the eigenstrain formulation included at a) quasi-static (0.004 s^{-1}) and b) $50,000 \text{ s}^{-1}$ strain-rates

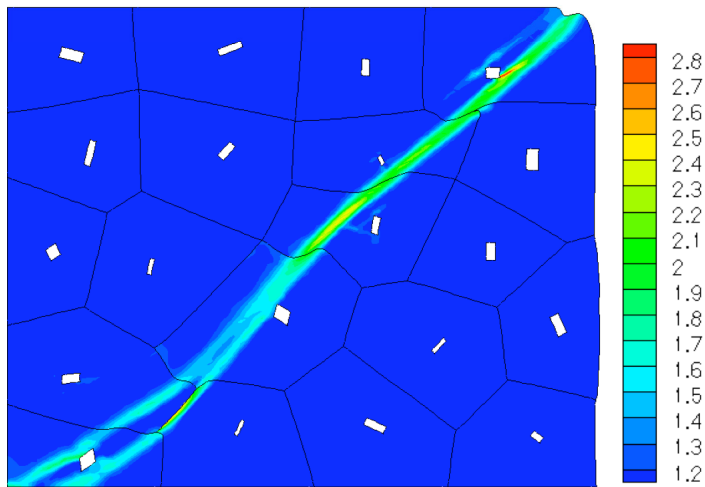


Figure 8.8: Matrix temperature (normalized by 293 K) at 10% nominal compressive strain for the 20-grain aggregate with the eigenstrain formulation at a strain-rate of $50,000 \text{ s}^{-1}$

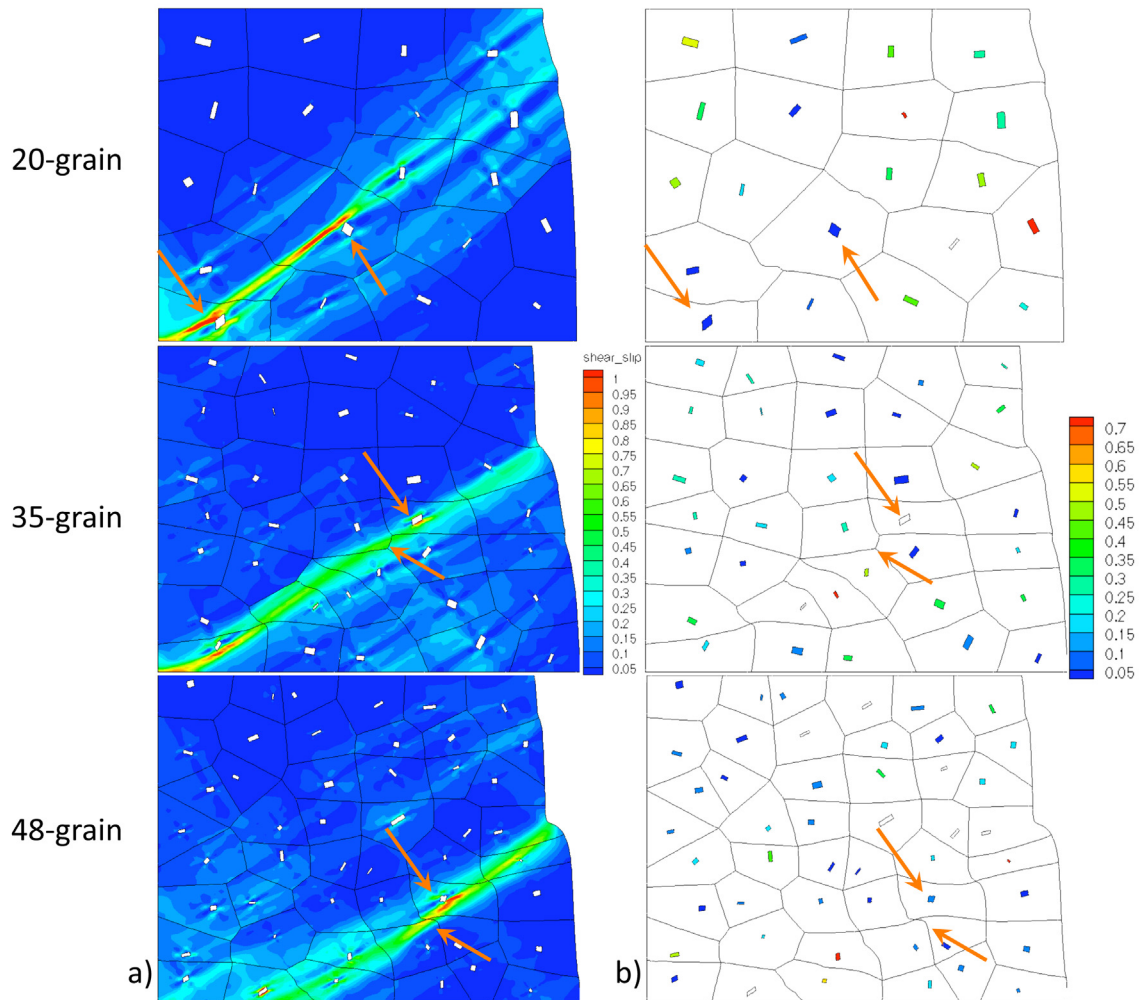


Figure 8.9: a) Effective plastic shear slip in the matrix and b) percent of eigenstrain relaxed at 10% nominal compressive strain for the 20-, 35-, and 48-grain aggregates with low angle GB misorientations

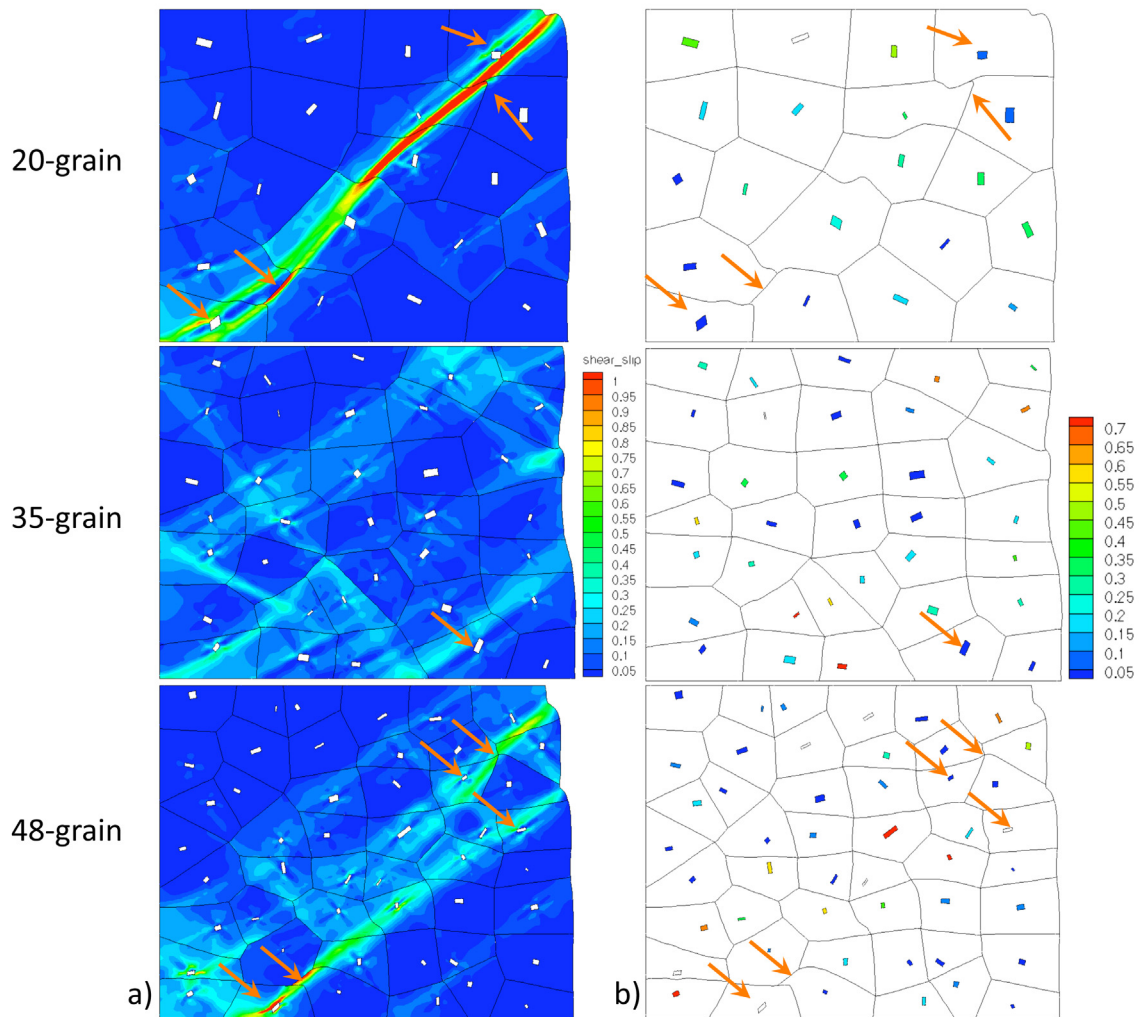


Figure 8.10: Effective plastic shear slip in the matrix and b) percent of eigenstrain relaxed at 10% nominal compressive strain for the 20-, 35-, and 48-grain aggregates with high angle GB misorientations

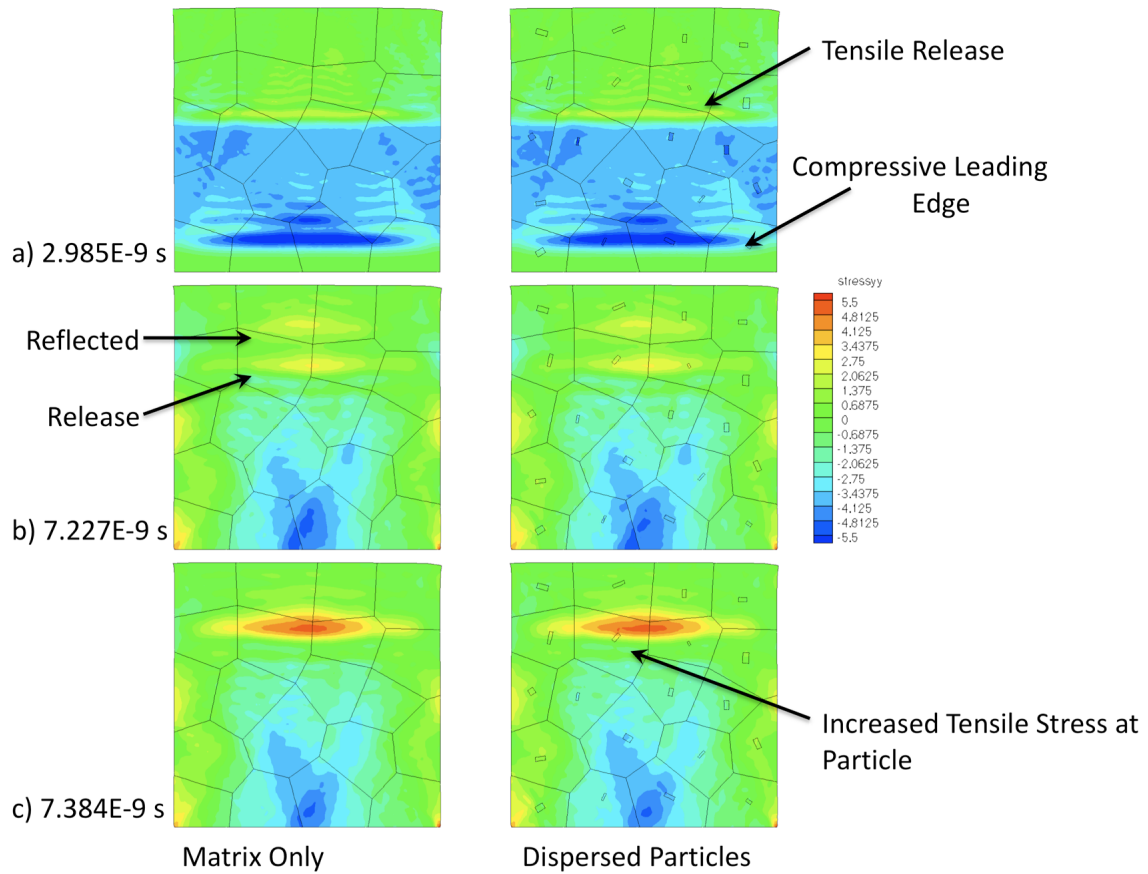


Figure 8.11: Vertical normal stress component contours (normalized by matrix static yield stress) detailing the effect of dispersed particles on stress accumulations associated with spall failure

Chapter 9: Dispersed Particle and Triple Junction Interactions in Aluminum Alloys

9.1. Introduction

The effects of grain boundary (GB) misorientations on the thermo-mechanical behavior of metals have been extensively studied (see, for example, Kobayashi, Tsurekawa et al. 2006; Kobayashi, Tsurekawa et al. 2005; Watanabe and Tsurekawa 1999; Kobayashi, Inomata et al. 2008; Davies and Randle 2001, Zikry and Kao 1996; Shi and Zikry 2009), with efforts mainly focusing on improving material toughness and ductility by inhibiting intergranular failure. High angle random GBs have generally been associated with GB hardening, due to a lack of slip transmission between the grains (Kobayashi, Tsurekawa et al. 2005). This lack of slip continuity can initiate intergranular cracking due to high stress concentrations when the geometrical orientation associated with the GB and loading is favorable for failure initiation under tensile loading (Watanabe and Tsurekawa 1999). Conversely, random low angle and low Σ coincident site lattice (CSL) GBs are favorable for preventing intergranular cracking due to lower stress concentrations and accumulations (Kobayashi, Tsurekawa et al. 2006).

The stress concentrations and GB hardening that can be associated with high angle random GBs are accentuated at triple junctions, where as many as three high angle random GBs may intersect. Triple junctions with two or more high angle random GBs can fracture more easily than those with more low angle or low Σ CSL GBs, due to higher compatibility

stresses and stress concentrations associated with high angle random GBs (Kobayashi, Tsurekawa et al. 2006; Kobayashi, Inomata et al. 2008).

The GB character of aluminum alloys is mainly associated high angle random GBs, with a lower percentage of low angle $\Sigma 1$ GBs. Therefore, the triple junctions are mainly R3, with three random GBs, or R2, with two random and one low angle or low Σ GBs (Kobayashi, Inomata et al. 2008, Fortier, Miller et al. 1997). Watanabe (1984) has shown that intergranular fracture occurs under tensile loads at random GBs, and transgranular fracture occurs when GBs intersecting the fractured random GBs are random low angle or low Σ CSL boundaries.

Numerous applications, such as ballistic loading and projectile penetration are associated with high strain-rate compressive loading conditions, and the effects of these loading conditions on local GB behavior is not well understood. It is of great interest, therefore, to investigate the interrelated effects of the GBs and *dispersed* particles on the high strain-rate deformation behavior and deformation modes of these high strength aluminum alloys subjected to these dynamic compressive loads.

The major objective of this investigation, therefore, is to use the dislocation density based crystal plasticity formulation and specialized microstructurally based FE models with an eigenstrain representation of Orowan looping and unrelaxed plastic strains, outlined in Chapters 3, 4, and 6, to investigate the interrelated effects of GB misorientation at triple junctions and particle dispersion on the high strain-rate compressive behavior of a high strength aluminum alloy. How these particles, GB misorientations, and triple junction arrangements affect possible failure modes, such as shear strain localization, stress

accumulations at GBs and particle-matrix interfaces, and dislocation density evolution, which can lead to failure of the alloy, will be a major focus of this chapter.

9.2. Results

9.2.1 Microstructural Representation

A 25 μm by 20 μm tri-crystal was modeled with different particle dispersions and random low and random high angle GB misorientations to investigate their interrelated effects on the high strain-rate compressive behavior of a high strength aluminum alloy. The model was deformed in plane strain, adiabatic compression at a strain-rate of $50 \times 10^{-3} \text{ s}^{-1}$. A convergent mesh was used, with at least three elements along each particle edge to generate a mesh of approximately 15000 elements with particles included in the simulation, and symmetry boundary conditions were used. Stiffness based hourglass control was used as outlined in Section 4.1. The junction angle at the tri-crystal was 120° (which would represent equal energy for each GB), and random high angle (R3) and random low angle misorientations (R0) were modeled. The Euler angles and GB misorientations are presented in Tables 9.1 and 9.2. The same Euler angles were used for the bottom grain (grain 3) for both high and low angle cases. Figure 9.1 shows a schematic of the models.

The effects of particle spacing were investigated by modeling three different volume fractions, 0.5%, 1%, and 1.5%, of randomly dispersed and oriented particles with sizes randomly generated about a mean value of 600 nm x 300 nm. The effects of particle size were investigated by modeling three particle sizes with the same particle dispersion and orientation. Particle sizes were randomly generated about an experimentally observed mean value of 600 nm x 300 nm (Lee and Zikry 2011) at 1% volume fraction, and scaled down to

425 nm x 212.5 nm (0.5% volume fraction), and scaled up to 850 nm x 425 nm (1.5% volume fraction). The material properties are presented in Table 9.3.

9.2.2 Grain Boundary (GB) Misorientation

Figure 9.2 shows the effective shear slip and lattice rotation contours of the matrix without dispersed particles for both high angle and low angle GB misorientations at 10% nominal compressive strain. In both cases, the effective shear slip forms a local band at the bottom left corner, extending into grain 3. For the low angle GB misorientation case, the shear slip is more diffuse, with most of grain 3 and nearly half of grain 2 associated with shear slip that is generally greater than 0.15. The localized band extends at an angle with respect to horizontal that is less than that of the band in the high angle GB misorientation case, and intersects the grain 2-grain 3 GB below the triple junction. It can be seen that the orientation of the band is associated with the initial alignment of the most active slip systems of the low angle misoriented grains instead of propagating directly towards the triple junction, and therefore not greatly affected by the triple junction.

The localized shear band that forms for the high angle GB misorientation case, on the other hand, extends into grain 3 at an orientation associated with the triple junction. The shear slip distribution is more localized and intense in comparison with the low angle GB misorientation case, and is affected by the triple junction and the loading conditions, with the highest shear stresses occurring at a 45° angle from horizontal, and shear slip localization is observed to a lesser extent in grain 2.

Positive lattice rotation bands are associated with the localization of the shear slip. These lattice rotations align the most active slip system of grain 3 closer to the plane of

highest shear stress (Figure 2b). The lattice rotations are less intense for the low angle GB misorientation case because the matrix deforms more homogeneously due to the lower angle misorientation values across the GBs. The high angle GB misorientations result in a band of lattice rotations in grain 3 that align the most active slip system of (1-11)[-101] in that localized band with the macroscopic plane of maximum shear stress. This lattice rotation is associated with mobile dislocation densities generated on a secondary slip system, as shown in Figure 9.3.

9.2.3 Dispersed Particle-GB Interaction

9.2.3.1 Particle Spacing

Figure 9.4 compares the effective shear slip in the matrix for particles with an average size of 600 nm x 300 nm at volume fractions of 0.5%, 1%, and 1.5% and low angle GB misorientations. It is evident that the localization behavior with 0.5% volume fraction of particles is similar to that of the tri-crystal with no dispersed particles (Figure 9.2a). The localized band of shear slip extends further as the dispersed particle volume fraction increased to 1%. An increase in volume fraction to 1.5% decreases the distance that the shear band propagates, which can be due to the secondary bands generated at the particle-matrix interfaces of the particles marked with arrows in Figure 9.4c. The angle of the shear band, with respect to horizontal, is the same as that of the tri-crystal without dispersed particles for all cases, indicating that the shear band is associated more with the preferential slip systems of the matrix than with the triple junction.

Figure 9.5 shows the matrix lattice rotations and percent of eigenstrain relaxed in the particles for the 1.5% volume fraction (small particle spacing) case. Local lattice rotational

structures, as was the case for tri-crystal without dispersed particles, are associated with the local shear slip behavior, with the difference being the particles that do not relax result in local lattice rotations. The reduced particle spacing can, therefore, allow for secondary shear band generation at the particle-matrix interface due to the interactions of the rotation fields associated with the particles (Figure 9.5), which can reduce the intensity of the primary shear band for low angle GB misorientations.

Figure 9.6 compares the effective shear slip contours for particles with average sizes of 600 nm x 300 nm at volume fractions of 0.5%, 1%, and 1.5% and high angle GB misorientations. It is clear that the increase in volume fraction (or decrease in particle spacing) reduces the overall intensity of the shear band in grain 3, and diffuses its propagation into grain 2.

Unlike the low angle GB misorientation case, the shear band does not follow the same path for all cases. For the 0.5% volume fraction case, a shear band intersects the grain 2-grain 3 GB further from the triple-junction in comparison with the tri-crystal case without any dispersed particles. This indicates that even a small particle volume fraction (large spacing) can have a significant effect on shear localization for high angle GB misorientations. The shear strain is localized in grain 2 (Figure 6a). The 1% volume fraction case has a similar shear band path as that of the tri-crystal without any dispersed particles, with some secondary localization occurring at the dispersed particle marked with an arrow (Figure 6b). The localization that occurs in grain 2 for the 1.0% volume fraction case is less intense than the 0.5% volume fraction case. The shear band in grain 3 for the 1.5% volume fraction case shows a path similar to the 0.5% volume fraction case, with some localization

occurring in the direction of the triple junction and also at some particle-matrix interfaces. The shear slip in grain 2 is most homogeneous for this case. This is due to the increased number of active slip systems associated with the dispersed particles (Figure 9.7).

9.2.3.2 Particle Size

Figure 9.8 shows the contours of effective plastic shear slip and lattice rotation in the matrix for three average particle sizes of 425 nm x 212.5 nm, 600 nm x 300 nm, and 850 nm x 425 nm, with the same initial dispersion and orientation and low angle GB misorientations for all three GBs. The particles accounted for volume fractions of 0.5% (425 nm by 212.5 nm particles), 1.0% (600 nm by 300 nm particles), and 1.5% (850 nm by 425 nm particles). A shear band from the lower left corner, extending into grain 3 in a similar fashion as was the case for the tri-crystal without any dispersed particles, indicates a minimal effect of the triple junction. The distance traversed by the band is similar in all cases, with only the 0.5% volume fraction case showing bifurcation around a particle. This is due to the different lattice rotation interactions associated with the different particle sizes. As the particle sizes increase, so does the effect of the particle, marked by an arrow in Figure 9.8, on the lattice rotations. The effects of this larger particle result in the interaction of the rotation fields associated with the particle and the band, diverting the rotation band from the top of the circled particle to the bottom, which further promotes the localization on that side of the particle.

Figure 9.9 compares the contours of effective plastic shear slip for the three average particle sizes with the same initial dispersion and orientation with high angle GB misorientations, and the percent of eigenstrain relaxed in each particle. It is clear that the

particles in the vicinity of the band, which are associated with minimal relaxation of the eigenstrain, lead to shear band bifurcation, and also inhibit the propagation of the shear band into grain 2. The tri-crystal with the larger 850 nm by 425 nm average size particles has the lowest of shear localization, but also has the highest effective stress concentration at the triple junction and tensile pressure buildups at the particle-matrix interfaces (Figure 9.10).

Figure 9.11 details the evolution of mobile dislocation densities associated with localized shear slip on a mostly inactive slip system for the tri-crystal with high angle GB misorientations without any dispersed particles and with 850 nm by 425 nm average size particles. It is evident that when there are no dispersed particles, the mobile dislocation densities on this mostly inactive slip system are generated at the bottom left corner and propagate in the direction of the triple junction. In contrast, the dislocation-densities on this slip system are generated at the particle-matrix interfaces when the dispersed particles are present. The dislocation densities propagate towards the bottom left corner, and in the other direction, interact with the next dispersed particle in the plane of maximum shear stress. The propagation of the shear band from the bottom left corner to the triple junction is therefore delayed by the local particle controlled dislocation density generation and localization at the particle-matrix interface, thus underscoring how the dispersed particles can inhibit shear localization that can be triggered by the presence of high angle random triple junctions. This beneficial effect must, however, be balanced with the increases of interfacial tensile pressures and triple junction stress accumulations associated with larger dispersed particles.

Figure 9.12 shows the effects of the dispersed particles on the overall behavior of the alloy for both high angle random and low angle random GB misorientation cases by plotting

the stress-strain curves for all of the investigated cases. It is clear that the effects of the dispersed particles were greater on the overall behavior for the high angle GB misorientation case, with nominal stress values differing by 2.4% at 10% nominal compressive strain compared to differences of 0.7% for the low angle GB misorientation case.

9.3. Conclusions

An eigenstrain formulation accounting for incompatibilities in plastic strain associated with Orowan looping and plastic relaxation coupled to a dislocation density based crystalline plasticity and a microstructurally-based finite-element framework was used to investigate the interrelated effects of particle dispersion and GB misorientations on the dynamic compressive behavior tri-crystals with different low and high angle GB misorientation arrangements. For low angle GB misorientations, slip was relatively homogeneous and associated with initially preferential slip systems. Lattice rotations associated with the particles led to increased localization at the particle matrix interface for low angle GB misorientations.

Particle dispersion had a greater effect on the deformation behavior for the high angle GB misorientation tri-crystal. Dislocation density generation at the particle-matrix interface resulted in particle-controlled shear banding, which can inhibit shear-banding effects associated with the triple junctions. However, larger dispersed particles led to increased stress concentrations at the triple junction and increased tensile pressures at the particle-matrix interfaces. This study underscores the distinct effects of dispersed particles on the behavior of alloys with random high angle and low angle GB misorientations, and how

material competition between particle distributions and sizes and triple junctions can be potentially controlled to mitigate shear strain localization within and between grains.

References—Chapter 9

- Davies, P and V. Randle, (2001). “Grain Boundary Engineering and the Role of the Interfacial Plane,” Materials Science and Technology **17**:615-626.
- Fortier, P., Miller, W.A., et al. (1997). “Triple Junction and Grain Boundary Character Distributions in Metallic Matrices,” Acta Metallurgica **45**(8):3459-3467.
- Kobayashi, S., Inomata, T., et al. (2008). “Effects of Grain Boundary- and Triple Junction-Character on Intergranular Fatigue Crack Nucleation in Polycrystalline Aluminum,” Journal of Materials Science **43**:3792-3799.
- Kobayashi, S., Tsurekawa, S., et al. (2006). “Structure-Dependent Triple Junction Hardening and Intergranular Fracture in Molybdenum,” Philosophical Magazine **86**(33-35):5419-5429.
- Kobayashi, S., Tsurekawa, S., et al. (2005). “Grain Boundary Hardening and Triple Junction Hardening in Polycrystalline Molybdenum,” Acta Materialia **53**:1051-1057.
- Lee, W. M. and M. A. Zikry (2011). “Microstructural Characterization of a High-Strength Aluminum Alloy Subjected to High Strain-Rate Impact.” Metallurgical and Materials Transactions. A, Physical Metallurgy and Materials Science **42**(5): 1215-1221.
- Shi, J. and M. A. Zikry (2009). “Grain–Boundary Interactions and Orientation Effects on Crack Behavior in Polycrystalline Aggregates.” International Journal of Solids and Structures **46**: 3914–3925.
- Starke, E.A., and T. H. Sanders (1980). “The Effect of Microstructure on the Properties of High Strength Aluminum Alloys.” AFOSR Annual Scientific Report. ADA083768.
- Watanabe, T. (1984). “An Approach to Grain Boundary Design for Strong and Ductile Polycrystals,” Res Mechanica **11**:47-84.
- Watanabe, T. and S. Tsurekawa, (1999). “The Control of Brittleness and Development of Desirable Mechanical Properties in Polycrystalline Systems by Grain Boundary Engineering,” Acta Materialia **47**(15):4171-4185.
- Zikry, M. A. and M. Kao (1996). “Inelastic Microstructural Failure Mechanisms in Crystalline Materials with High Angle Grain Boundaries.” Journal of the Mechanics and Physics of Solids **44**(11): 1765–1798.

Tables and Figures—Chapter 9

Table 9.1: Euler angles used in the tri-crystal simulations (deg)

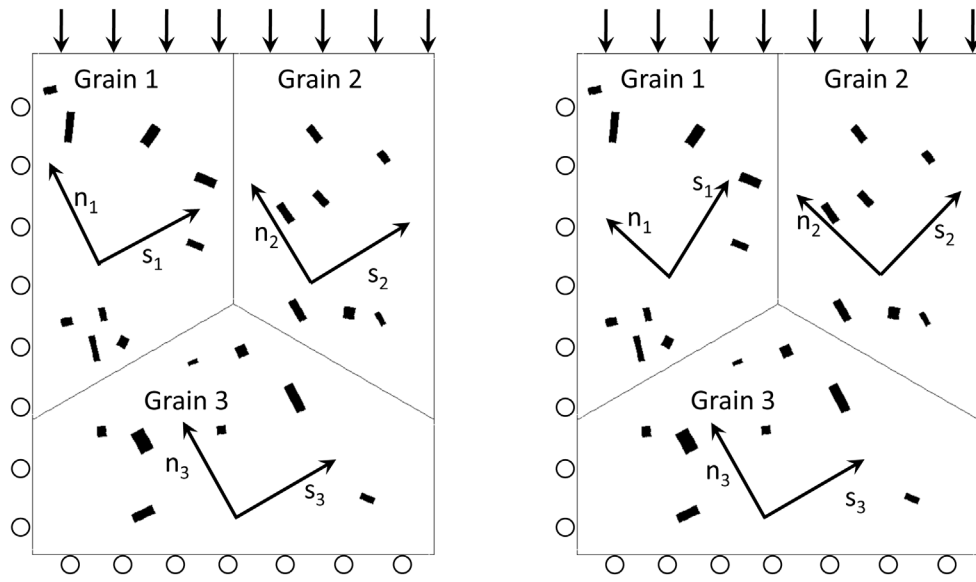
	Low angle			High angle		
	ϕ_1	Φ	ϕ_2	ϕ_1	Φ	ϕ_2
Grain 1	-60.8	-30.4	-24	-59	-36.7	-51.2
Grain 2	-56.8	-28.5	-17.3	-75.1	-74.1	-25.5
Grain 3	-43.9	-20.9	-38.8	-43.9	-20.9	-38.8

Table 9.2: GB misorientation angles (deg)

	Low angle	High angle
GB 1-2	10.7	39.1
GB 1-3	11.9	30.9
GB 2-3	13.5	65.1

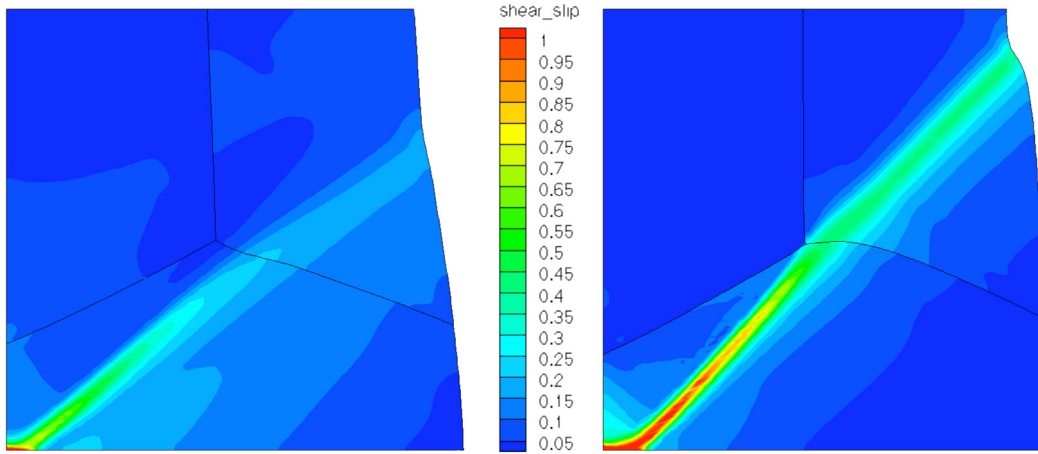
Table 9.3: Material properties of aluminum matrix and manganese-bearing dispersed particles

Property	Matrix Value	Particle Value
Elastic Modulus, E	70 GPa	110 GPa
Poisson's Ratio, ν	0.33	0.33
Static Yield Strength, τ_s^α	200 MPa	∞
Rate Sensitivity, m	0.01	N/A
Reference Strain-rate, $\dot{\gamma}_{ref}$	0.001 s^{-1}	N/A
Burgers Vector, \bar{b}	$0.289 \times \{111\}\langle 110 \rangle \text{ nm}$	N/A
Initial ρ_m	10^{11} m^{-2}	N/A
Initial ρ_{im}	10^{13} m^{-2}	N/A
Saturation ρ_{sat}	10^{14} m^{-2}	N/A



a) Low Angle GB Misorientations b) High Angle GB Misorientations

Figure 9.1: Schematic of the models; Initial alignment of the most active slip system in each grain is indicated



a) Low Angle GB Misorientation

b) High Angle GB Misorientation

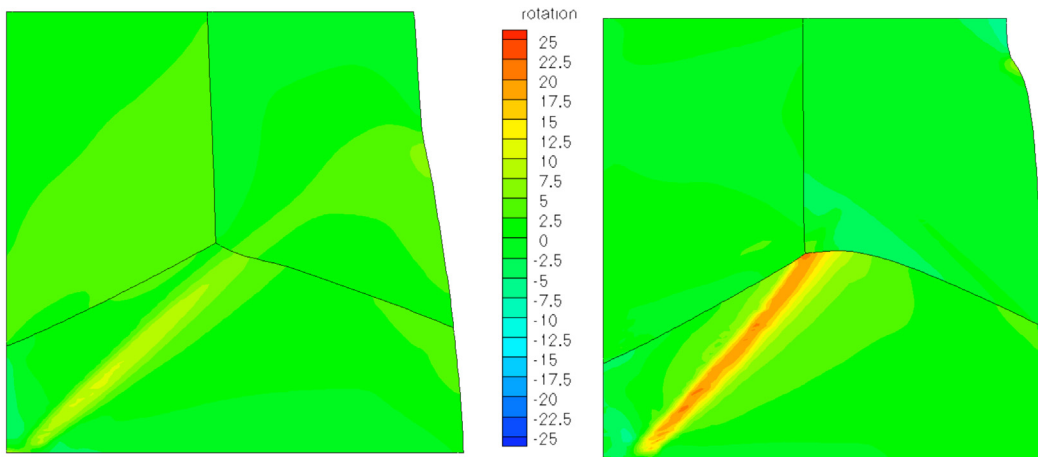


Figure 9.2: Effective shear slip and lattice rotation contours of the tri-crystal with no particles at 10% nominal compressive strain; a) Low angle GB misorientation and b) high angle GB misorientation

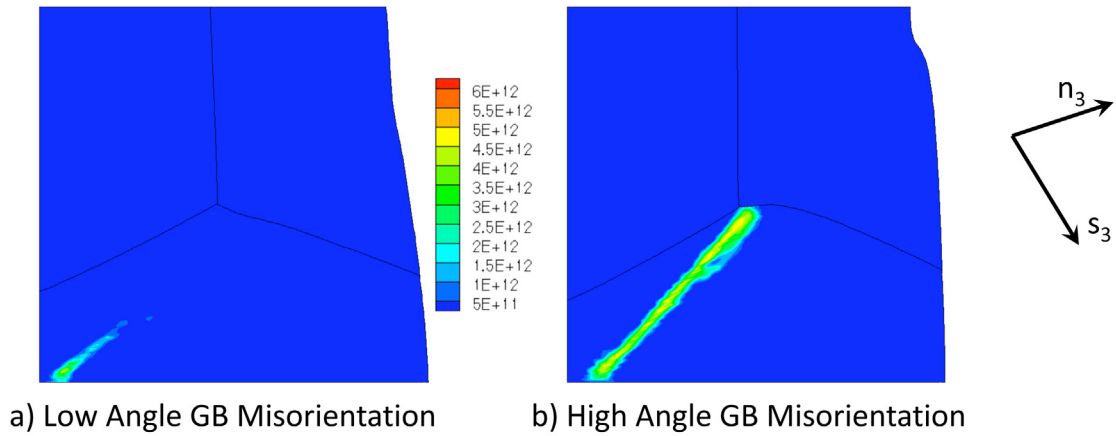


Figure 9.3: Mobile dislocation densities (m^{-2}) on a secondary $(-111)[101]$ slip system with no particles at 10% nominal compressive strain; a) Low angle GB misorientation and b) high angle GB misorientation. Initial orientation of the slip system in grain 3 is shown

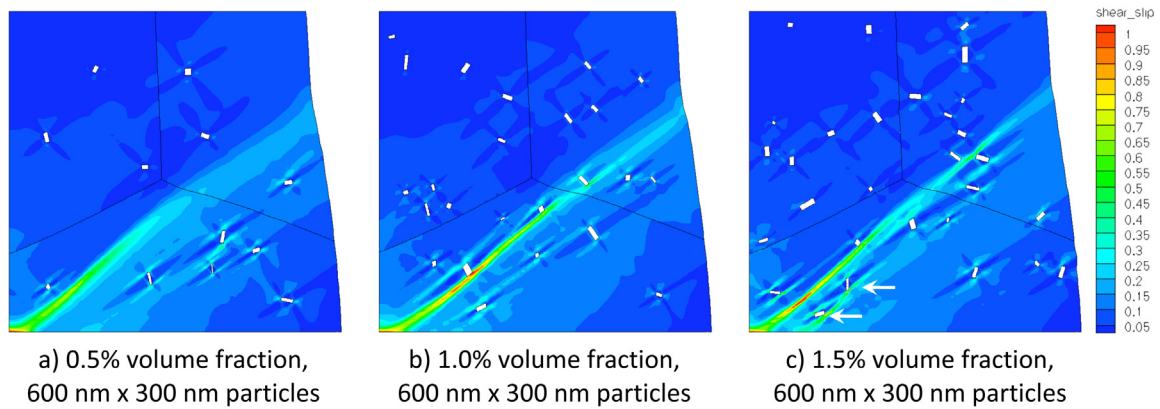


Figure 9.4: Effective plastic shear slip contours for 600 nm by 300 nm average particle size dispersions with low angle GB misorientations at 10% nominal compressive strain; a) 0.5% volume fraction, b) 1.0% volume fraction, and c) 1.5% volume fraction

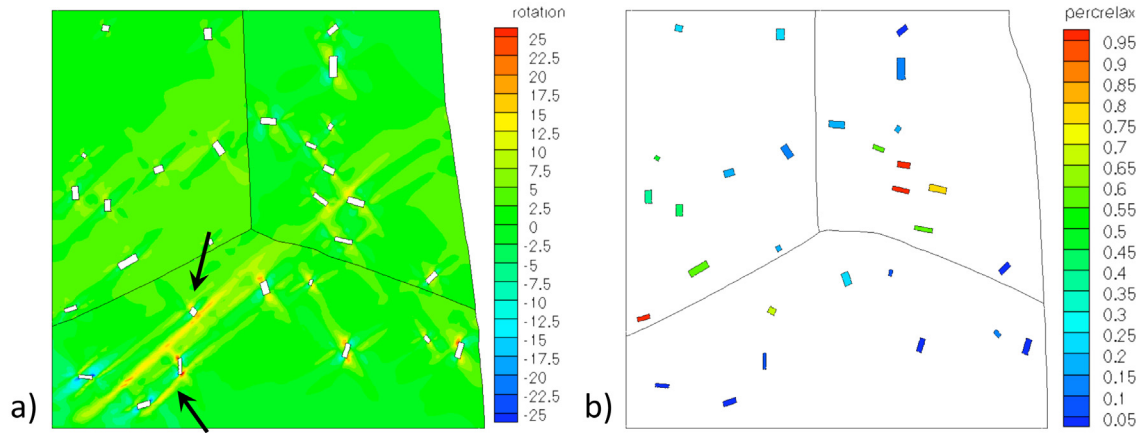


Figure 9.5: a) Lattice rotation and b) percent of eigenstrain relaxed

$\left(\left(\int D_{12,max_shear}^* dt - \int D_{12,max_shear_relaxed}^* dt \right) / \int D_{12,max_shear}^* dt \right)$ for 1.5% volume fraction of 600 nm by 300 nm average size particles and low angle GB misorientations at 10% nominal compressive strain

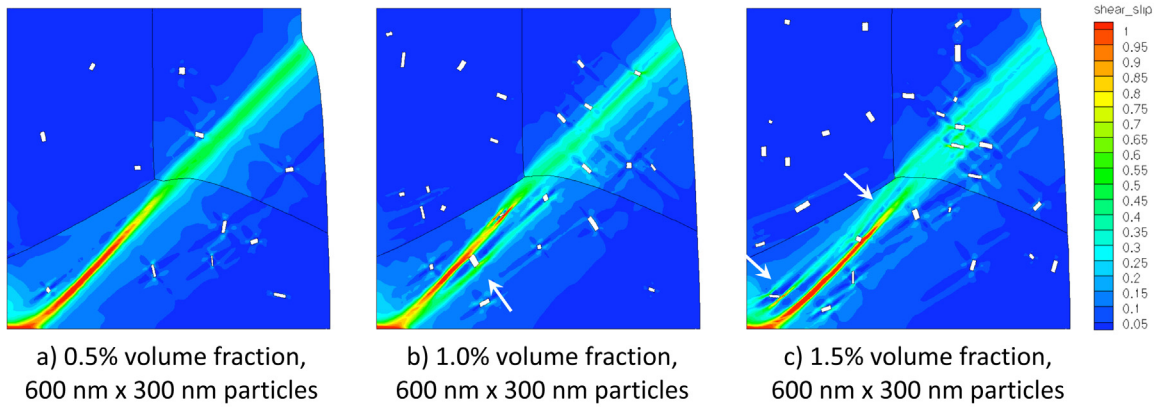


Figure 9.6: Effective plastic shear slip contours for 600 nm by 300 nm average particle size dispersions with high angle GB misorientations at 10% nominal compressive strain; a) 0.5% volume fraction, b) 1.0% volume fraction, and c) 1.5% volume fraction

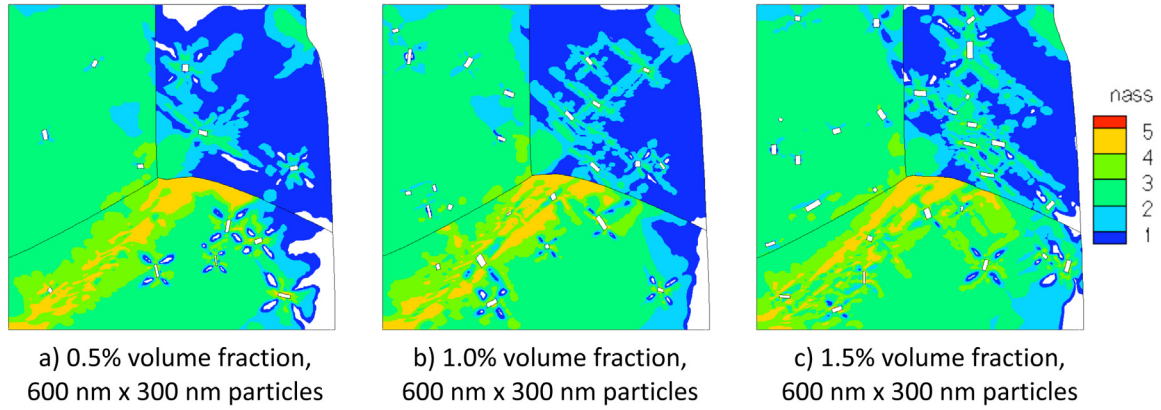


Figure 9.7: Number of active slip systems at 10% nominal compressive strain for 600 nm by 300 nm average particle size dispersions with high angle GB misorientations; a) 0.5% volume fraction, b) 1.0% volume fraction, and c) 1.5% volume fraction

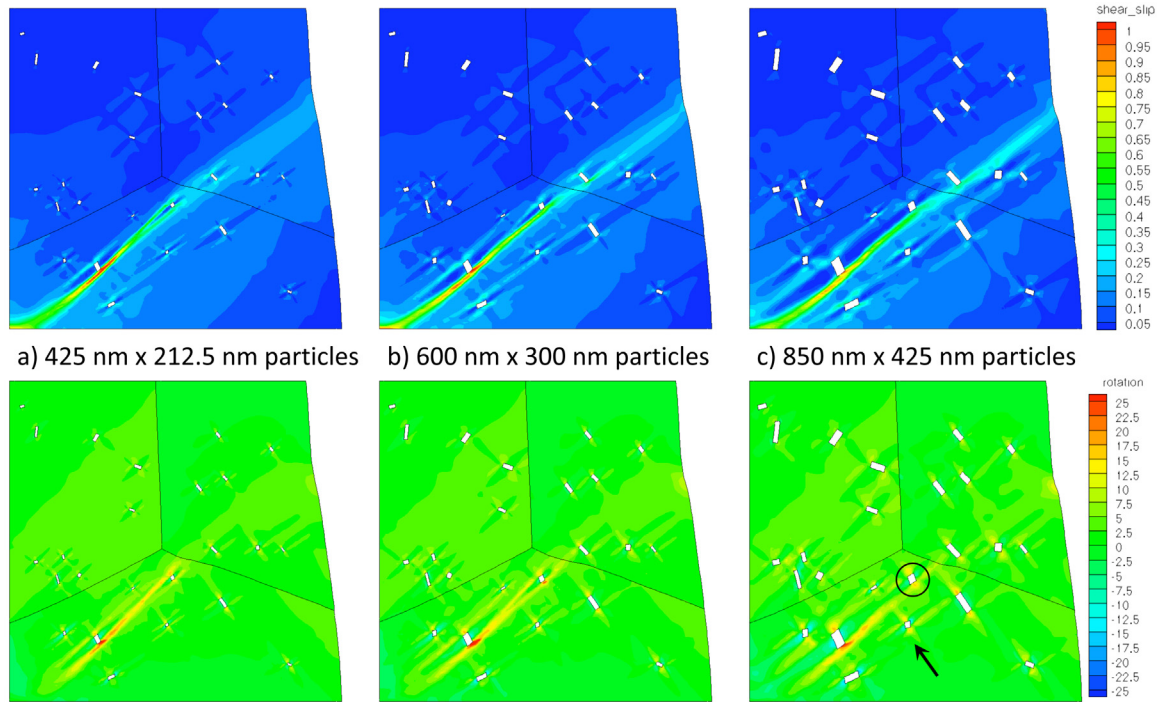


Figure 9.8: Effective plastic shear slip and lattice rotation contours for low angle GB misorientations at 10% compressive strain; a) 425 nm by 212.5 nm average particle size, b) 600 nm by 300 nm average particle size, and c) 850 nm by 425 nm average particle size

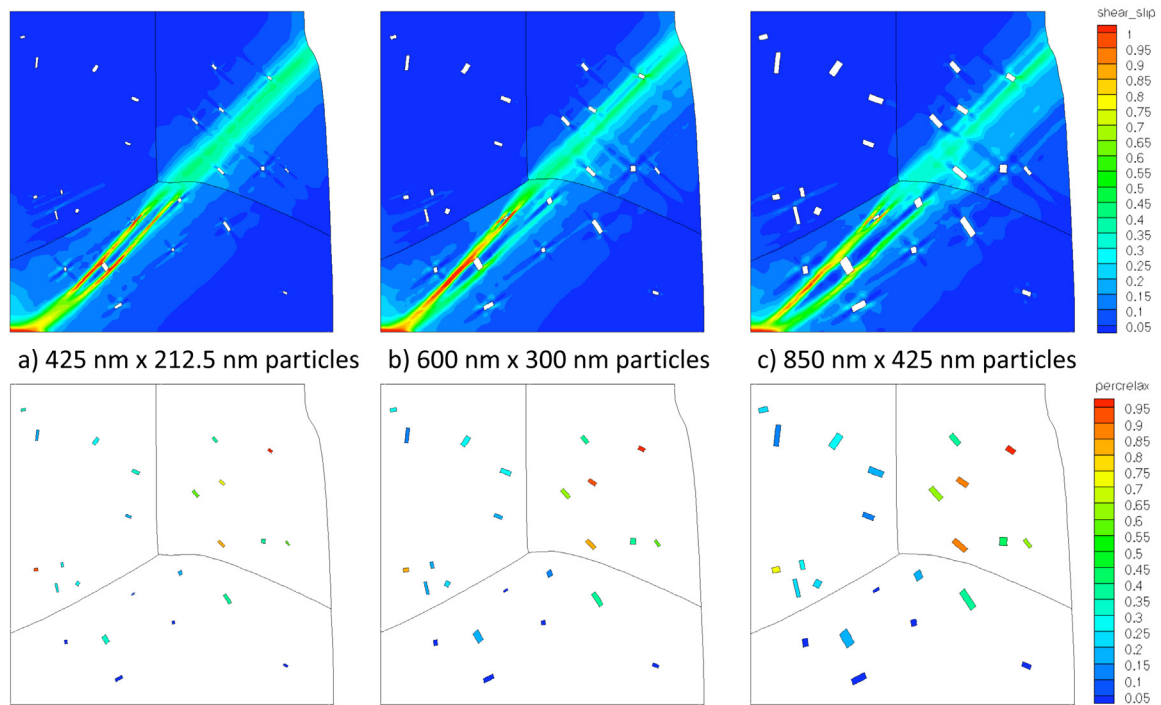


Figure 9.9: Contours of effective plastic shear slip and percent of particle eigenstrain relaxed for the same particle dispersion and orientation with high angle GB misorientations at 10% nominal compressive strain; a) 425 nm by 212.5 nm average particle size, b) 600 nm by 300 nm average particle size, and c) 850 nm by 425 nm average particle size

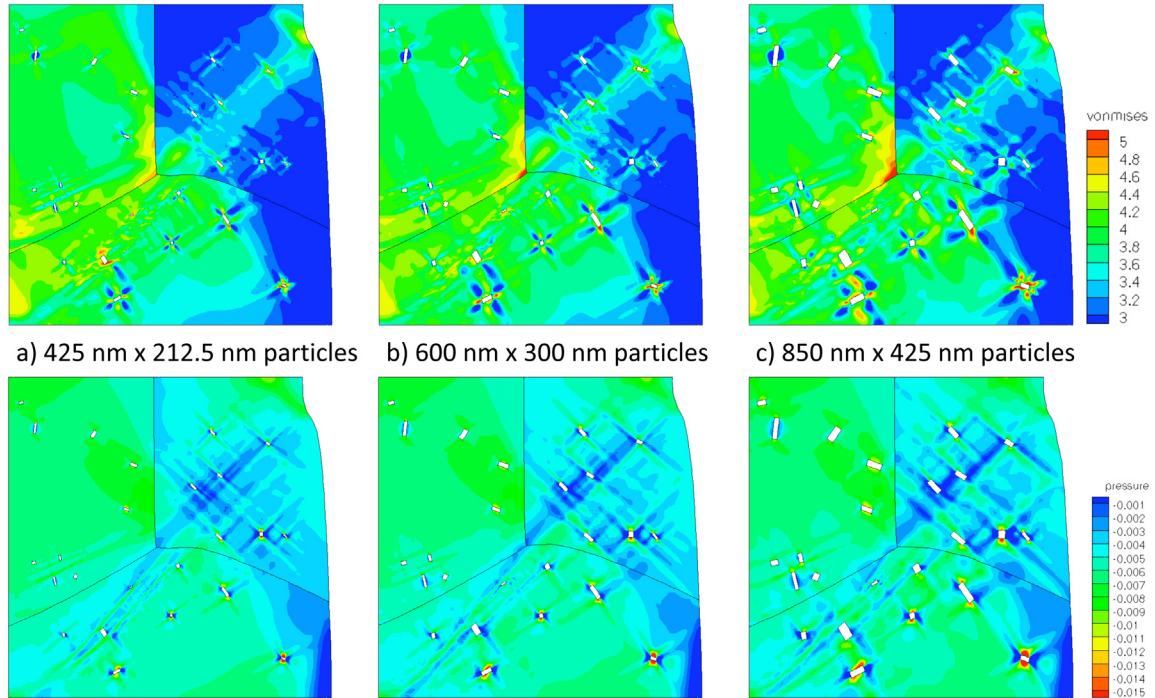


Figure 9.10: von Mises stress (normalized by matrix static yield stress) and pressure (normalized by matrix Young's modulus) contours for the same particle dispersion and orientation with high angle GB misorientations at 10% compressive strain; a) 425 nm by 212.5 nm average particle size, b) 600 nm by 300 nm average particle size, and c) 850 nm by 425 nm average particle size. Pressure contour levels set to emphasize decrease in compressive pressures and transition to tensile pressures at the particle-matrix interface

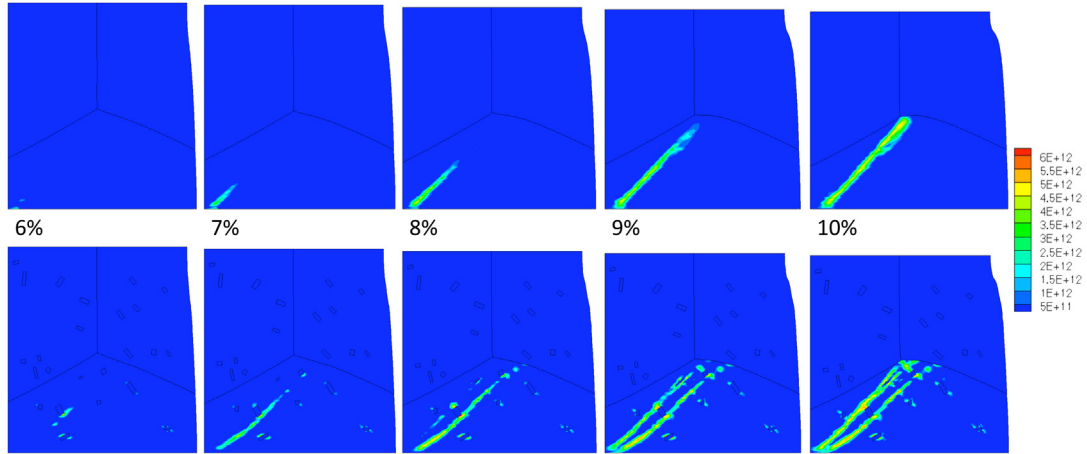
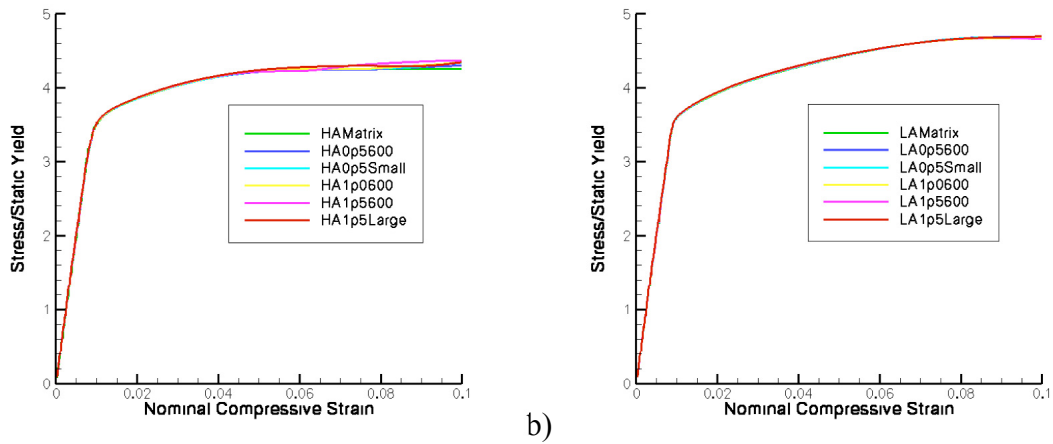


Figure 9.11: Evolution of mobile dislocation densities on a secondary $(-111)[101]$ slip system as a function of overall nominal compressive strain for matrix only and 850 nm by 425 nm average particle size simulations



a) b)
Figure 9.12: Nominal stress-nominal strain curves for the a) high angle random and b) low angle random GB misorientation tri-crystal investigations, showing a 2.4% spread in values at 10% nominal strain for high angle GB misorientations compared to 0.7% associated with low angle GB misorientations

Chapter 10: Future Research Recommendations

- Perform an investigation into the precipitation process and formation of $\text{Al}_{20}\text{Cu}_2\text{Mn}_3$ dispersed particles. Specifically, is there a rational orientation relationship between the dispersed particles and the aluminum matrix? It has been observed that $\text{Al}_{20}\text{Cu}_2\text{Mn}_3$ dispersed particles can nucleate at θ precipitates, which suggests there may be some preferred orientation (Zoeller and Sanders 2004).
- Determine the mechanical behavior, such as elastic modulus and yield strength, of the $\text{Al}_{20}\text{Cu}_2\text{Mn}_3$ dispersed particles by means of nano-indentation.
- Couple the tri-crystal investigation with a finite element formulation accounting for slip transmission between the grains, such as that of (Shi and Zikry 2009), to investigate the possible effects of dislocation pileups at the GBs of the alloy.
- Investigate how texture of the alloy grain affects the stress fields and shear slip distributions associated with Orowan looping.
- Include other possible plastic relaxation mechanisms, associated with smaller particles, such as prismatic loop punching (Hirsch and Humphreys 1970) and diffusion (Mura 1987), to investigate the effects of smaller dispersed particles on the failure modes of Al alloys.
- Use a coupled thermo-mechanical finite element framework accounting for thermal conduction to investigate how thermal conduction relates to the size effects of the particles for relevant strain-rates.

- Extend the eigenstrain formulation representing Orowan looping and plastic relaxation to a 3-D simulation.

References—Chapter 10

- Hirsch, P. B. and F. J. Humphreys (1970). “The Deformation of Single Crystals of Copper and Copper-Zinc Alloys Containing Alumina Particles. II. Microstructure and Dislocation-Particle Interactions,” Proceedings of the Royal Society of London A **318**: 73-92.
- Mura, T. (1987). Micromechanics of Defects in Solids (2nd ed.). The Netherlands, Martinus Nijhoff.
- Shi, J. and M. A. Zikry (2009). “Grain–boundary interactions and orientation effects on crack behavior in polycrystalline aggregates.” International Journal of Solids and Structures **46**: 3914–3925.
- Zoeller, T. L. and T. H. Sanders Jr. (2004). “The Rate of Solidification and the Effects of Local Composition on the Subsequent Nucleation of $\text{Al}_{20}\text{Cu}_2\text{Mn}_3$ Dispersoid Phase in Al-4Cu-0.3Fe-0.4Mn-0.2Si Alloys.” Journal de Physique IV **120**: 61-68.